Quantitative Modelling of the Effect of Speed Mismatch on Technological Parameters in Steel Rolling

Anant Sareen

Master of Science Thesis

Delft Center for Systems and Control

Quantitative Modelling of the Effect of Speed Mismatch on Technological Parameters in Steel Rolling

MASTER OF SCIENCE THESIS

For the degree of Master of Science in Systems and Control at Delft University of Technology

Anant Sareen

July 28, 2022

Faculty of Mechanical, Maritime and Materials Engineering (3mE) · Delft University of Technology

ArcelorMittal Hamburg GmbH supported the work in this thesis. Their cooperation is gratefully acknowledged.

Abstract

Steel production is a critical index to measure the infrastructural growth and development of a nation. The steel production capacity of a nation has a significant impact on its GDP. Even though steel rolling has been in the industry since the early 1700s, there have not been significant advancements in its technology space. The safety hazards to personnel and failure of process components have persistently posed daunting challenges for the steel industry. The advent of automation in the late 1900s helped the industry manage some of these challenges to a certain extent. Despite these technological improvements, the realm of steel rolling is still not explored thoroughly because steel rolling is a highly integrated and complex system with numerous process parameters impacting the quality of the finished product. As a result, the study of the dynamics of steel rolling is still under active research targeted toward improving the complex processes involved in the industry.

External factors play a significant role in the complexity of the steel rolling process. The scope of the work herein attempts to identify and model some of these significant external factors, also known as "disturbances" in control terminology. A Finite-Element Method (FEM) based simulator for the rolling process simulation incorporating the external disturbances is explored. The outcomes from this simulation will enable establishing regression models that facilitate quantifying external disturbances' effects on the technological/process parameters in steel rolling.

The thesis is focused on studying the external disturbance of speed mismatch and proposing a quantitative model for evaluating the effect of speed mismatch on the process parameters of rolling. Subsequent to the development of the proposed disturbance quantitative model, three controller systems - Proportional Integral Derivative (PID) controller, Linear Quadratic Regulator (LQR) controller, and Model Predictive Control (MPC) controller will be implemented to evaluate comparisons between the controllers for disturbance rejection and reference tracking.

The scope of the work presented in this thesis is significant as it focuses on developing a quantitative model for the process disturbances that prevail in the steel rolling industry.

Table of Contents

List of Figures

List of Tables

Preface

The thesis has been conducted under the supervision of Prof.Dr.Tamás Keviczky. I express umpteen gratitude to my Supervisor for his supportive mentorship during my academic pursuits and completion of this thesis work.

I would also like to thank my Supervisor at ArcelorMittal Hamburg, Mr. Jesus Robles, for his prompt support and access to organisational data and assets. I would like to extend my special gratitude to numerous plant operators and process engineers of the "Walzwerk" department who supported me in learning the steel rolling process and shared their valuable insights into plant operations. In addition, sincere gratitude to the Qform group for their support in assisting with the simulator software.

I thank my Delft Center for Systems and Control (DCSC) colleagues for their camaraderie during this challenging pandemic period.

Finally and most importantly, I would like to thank my parents and my brother for their wise counsel and continued support during my academic and career aspirations.

Chapter 1

Introduction

The rolling of steel is a highly nonlinear and complex process that directs the quality of the finished product. Modernization and digitalization of the steel plants are a growing trend to fulfill the demands of the colossal steel industry.

The basic fundamental processes in steel rolling space have not changed significantly since the early 20th century, which led to the development of control strategies and improvements for various components of the rolling mill to ensure higher productivity and adherence to stricter dimensional tolerances [12].

One of the most crucial issues affecting stable operation in rolling mills is the presence of longitudinal forces in the workpiece during rolling mill operation due to unequal mass flow of the rolled material between two adjacent mill stands. This force, known as tension, results in undesirable deformation in the rolled material that impacts the quality of the produced material. Tension during the rolling process results in the instability of the rolling process and thereby causing severe injuries to personnel operating the rolling mills. Excessive tension generated in the workpiece is a direct consequence of speed mismatch in adjacent work roll stands. Other factors affecting the stable operation of the rolling mill are temperature variations in the workpiece along the surface, the internal lattice, and the wear and tear of the work rolls.

The techniques for controlling the rolling mill operation highly depend on the section of the rolling mill. Generally, the two broad categories of control philosophies are looper and looper-less control.

The control philosophy with loopers is used in the intermediate and finishing sections of the rolling mill plant. The system consists of a mechanical device, a looper, installed between two adjacent rolling stands of the mill. The looper is hinged on one end and free on the other. Along with the looper, the drives of the work roll stands control the speed of the work rolls. The stability of the rolling process is maintained with the synchronisation of the looper angle control and the speed control of the rolling mill drives [13].

The use of loopers is not practical in the roughing section of the rolling mill due to the distance between consecutive stands being small and the bulky size of the material. In the absence of the loopers, the speed control of the work roll stands takes center stage to ensure the stability of the rolling process. Developing efficient speed control strategies is challenging due to the strong coupling between adjacent rolling mill stands. For the application of advanced speed control techniques for superior performance, it is essential to have an accurate system and disturbance models [14].

There has been significant research to develop an accurate system model for flat and longitudinal rolling. There has been limited research on the effect of disturbances on the stability of the rolling process. The scarce research that is available is focused on the area of sheet/flat rolling and not on longitudinal rolling. The available literature on disturbances in the longitudinal rolling process explains the various factors qualitatively. There has been little research to develop a quantitative disturbance model to explain these factors' effects. A possible explanation for a lesser interest in the disturbance modelling could be that the model obtained through the analysis is, to a certain extent, dependent on the configuration of the rolling mill and the rolling conditions on the mill. Another possible explanation could be the lack of instrumentation to measure certain factors like the temperature variation of the workpiece on the surface and the internal lattice. Finite-Element Method (FEM) based simulations could be a tool that can be used to try to replicate these conditions to a certain extent and solve the plastic deformation problem.

1-1 Motivation

The limited research in developing a quantitative model for the disturbances affecting the stability of the rolling mill process is the primary motivation for the work conducted in the thesis. The improvement of the speed control of the use-case facility is of the essence to achieve their goal of autonomous operation of the rolling mill by the end of 2030. This requirement of the use-case facility prompted the Author to use the current speed control philosophy at the use-case facility and propose alternate control philosophies based on a model approach to improve the speed control of the use-case facility.

1-2 Aim

The research questions tackled in the scope of this thesis work are discussed below as follows:-

1. Development of a quantitative model for the effect of the speed mismatch on technical parameters of rolling, which affect the stability of the rolling process.
   (a) Conduct experiments on the use-case facility to obtain specific data for the workpiece, work rolls, and environmental conditions.
   (b) Create 3-D models for the workpiece and work rolls based on technical drawings of the use-case facility.
   (c) Set up the FEM-based simulator according to the configuration of the rolling mill at the use-case facility.

   (d) Simulate the plastic deformation problem for different speed mismatches generally witnessed at the use-case facility and analyse the results obtained through the simulations.
   (e) Verify the results obtained from the FEM-based simulations with the help of theoretical equations already available in the literature on longitudinal rolling.
   (f) Using the data from the simulations conducted in the FEM simulator, obtain a regression model to quantify the effect of speed mismatch on rolling parameters.

2. Improve the speed control philosophy of the use-case facility for automatic speed regulation of the rolling mill with the help of simulations in MATLAB and Simulink.
   (a) Analyse the performance of the PID controller at the use-case facility under the influence of a speed mismatch disturbance.
   (b) Improve the performance of the PID controller at the use-case facility with the help of another PID controller.
   (c) Implement a Linear Quadratic Regulator (LQR) controller with disturbance rejection and reference tracking for the rolling mill.
   (d) Implement a Model Predictive Control (MPC) controller for the rolling mill.
   (e) Form a comparative study between the performance of the use-case facility controller and the proposed controllers.

3. Propose a road map for the development of quantitative models for other essential disturbances affecting the stability of the rolling process.

1-3 Outline

The master thesis consists of seven chapters. Chapter 2 will provide insight into the Use-Case, the wire rod rolling facility at ArcelorMittal Hamburg. Chapter 3 describes the various concepts and components in the steel rolling process and their inter-dependencies. Chapter 4 tackles the first research question and explains in-depth the setup of the FEM-based simulator, the speed mismatch simulation plan, the results of the simulations, and verification of the results of the simulations with the help of the theoretical equations presented in Chapter 3. Chapter 5 tackles the second research question of the master thesis and presents an overview of the current speed control philosophy at the use-case facility. The chapter also provides the necessary system transformations and theory required to design the model-based controllers. Chapter 6 tackles both the first and second research questions of the master thesis. The chapter first presents the regression model formed using the results of the simulations conducted in Chapter 4. Chapter 6 also discusses the performance of the different speed control philosophies presented in Chapter 5. Chapter 7 concludes the master thesis and answers the third research question by providing a possible extension of work conducted in the scope of this master thesis.

Chapter 2

Use-Case Facility

This chapter provides an overview of the ArcelorMittal Hamburg facility and the process flow of steel production. The facility is the Use-Case, where current work was conducted.

2-1 ArcelorMittal Hamburg

ArcelorMittal Hamburg is one of four facilities within the ArcelorMittal group in Germany. The plant, formerly known as Hamburger Stahlwerke GmbH, was set up in 1969 and started production in 1971 to produce simple steel qualities using sponge iron and scrap metal in an electric arc furnace. It was the world's second Direct Reduction plant at that time [15].

ArcelorMittal Hamburg is a trendsetter in the areas of productivity and energy efficiency. The plant employed 523 people and had a production output of 918,123 tonnes of steel billets in 2019. These semi-finished products are sold directly to customers or for the production of 5.5-16 mm wire rods using the in-house rolling mill facility. In 2019, the turnover of the plant was estimated at €453 million [15].

2-2 Production Facility

The production at the ArcelorMittal Hamburg plant consists of 5 significant steps, as shown below in Figure 2-1.

2-2-1 Reduction Plant-Based on MIDREX process

The infeed of the reduction plant consists of reducible hematite iron ore in the form of lumps and pellets. The infeed is fed in the reduction furnace through an inclined elevator. The reduction furnace is blown with a reduction gas, a mixture of hydrogen and carbon monoxide heated at around 960° C. The reduction gas heats the ore bed and reduces it to sponge

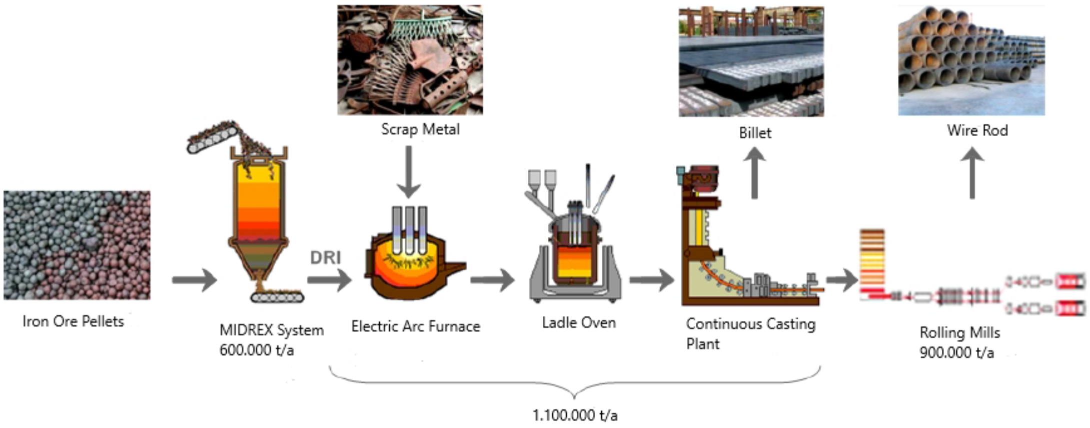

Figure 2-1: Production at ArcelorMittal Hamburg [1]

iron. The reducing gas is removed as furnace gas above the ore bed is cooled and cleaned in a washer. In the lower part of the reduction furnace, the cooling zone, the sponge iron is cooled to ambient temperature by cooling gas continuously drawn off via a vibrating chute discharge and transported to the storage bunker via a conveyor belt system. The reducing gas is generated in a reformer by catalytic cleavage at around 1100° C in 200 catalytic tubes from natural gas. Figure 2-2 depicts an illustration of the reduction process.

2-2-2 Electric Arc Furnace

ArcelorMittal Hamburg operates a 150-tonne three-phase electric arc furnace shown in Figure 2-3 with a transformer output of 205 MVA. Input materials to the furnace consisting of sponge iron and scrap steel depend on steel's quality under production. Slag is vital in the electric arc furnace as it minimizes heat loss and shields the arc. Lime and coal addition to the furnace helps regulate slag formation. The addition of carbon and other alloying materials based on the required quality of steel helps in the deoxidization of steel during the tapping process.

2-2-3 Ladle Furnace

After the steel melting is complete in the electric arc furnace, crude steel is poured into a ladle and transported to the ladle furnace. Secondary metallurgical enhancement of steel is done in the ladle furnace. Certain alloys are added precisely and systematically to achieve desired properties in the steel. The desulphurization process is carried out at the steel temperature and is controlled to achieve casting temperature.

2-2-4 Continuous Billet Caster

Figure 2-4 depicts the functional diagram of the Continuous Billet Caster. Liquid steel flows through a ladle slide with a shadow tube into the refractory-lined distributor during casting.

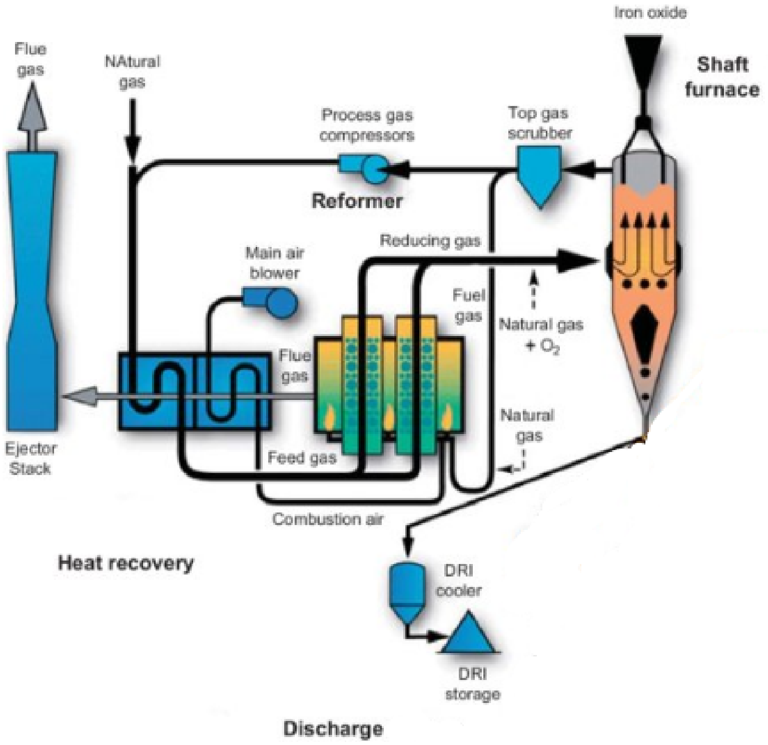

Figure 2-2: Illustration of MIDREX reduction process [2]

The shadow tube protects the steel from reoxidation and the formation of oxidizing inclusions. The distributor has a capacity of 25 tonnes, distributes the liquid steel over seven molds, and forms a buffer that enables the changing of ladles. The distributor feeds the steel into individual water-cooled copper molds using a nozzle. A nitrogen-filled bellow in the form of a flexible cylinder made from flame-retardant textile is attached around the nozzle to avoid the risk of reoxidation.

The mold is an 800 mm long, water-cooled copper pipe in a square format with dimensions of 130×130 mm. In the circular arc caster equipped with a casting radius of 5m, a straightening driver transports the glowing strands through the injection chamber, aligns the strand after the solidification process, and regulates the casting level in the mold. The strands are cut into the specified lengths by seven 300-tonne pendulum shears. The billets are cooled to around 400° C on the reversible cooling bed.

2-2-5 Wire Rod Mill

Figure 2-5 shows the layout of the Wire Rod Mill.

Lifting Hearth Furnace

For converting billets into wire rods, the temperature of the billets has to be in the range of 1000-1200° C, depending upon their quality. The Lifting Hearth Furnace preheats the

Figure 2-3: Electric arc furnace ArcelorMittal Hamburg (By Author)

billets before transport to the rolling mill stands. The output of the furnace is approximately 100 billets per hour. The total firing capacity of the furnace is 50MW. The furnace has 126 burners which burn a mixture of natural gas and air. The burners consist of the convection, heating, and compensation zones.

The billets come from a grid and are moved automatically over a roller conveyor into the furnace. Pushers push the billets from the roller table onto the fixed hearth of the furnace. With lifting flocks, the billets are transported towards the pulling hearth. The compensation zone consists of 9 sticks, out of which 5 are directly in front of the discharge opening. An ejecting machine pushes the billet from the pulling hearth in the direction of the pull-out driver, which drives the heated billet towards stand 0 of the rolling mill.

Roughing Mill and Intermediate Mill

The roughing and intermediate mill section consist of stands 0-15. The shapes of the grooves of the stands change in succession in the oval-round-oval format, as shown in Figure 2-6. The gaps between the upper and lower rollers of each stand are configured to obtain the final measurements of the wire rod. This section of the wire rod mill is responsible for the maximum deformation of the incoming billet (around 25% from stand to stand).

Two lines run parallel to each other through each stand. For uniform material deformation, the rolled material is rotated by 90° after each stand with the help of a twisting device.

A Direct Current (DC) machine drives each of the 16 stands via toothed gears. The transmission ratio of the gears is graded to ensure that the rolling speed increases in the direction of rolling.

After the roughing mill section, there is a cropping and chopping shear. The head and tail

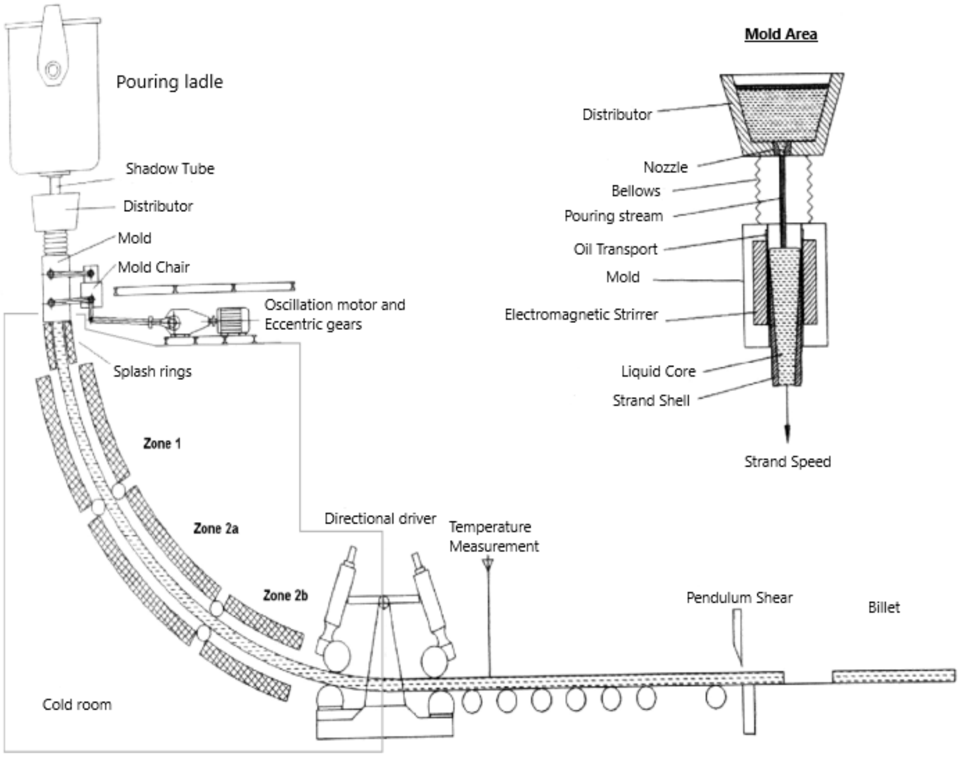

Figure 2-4: Functional Diagram of Continuous Billet Castor [1]

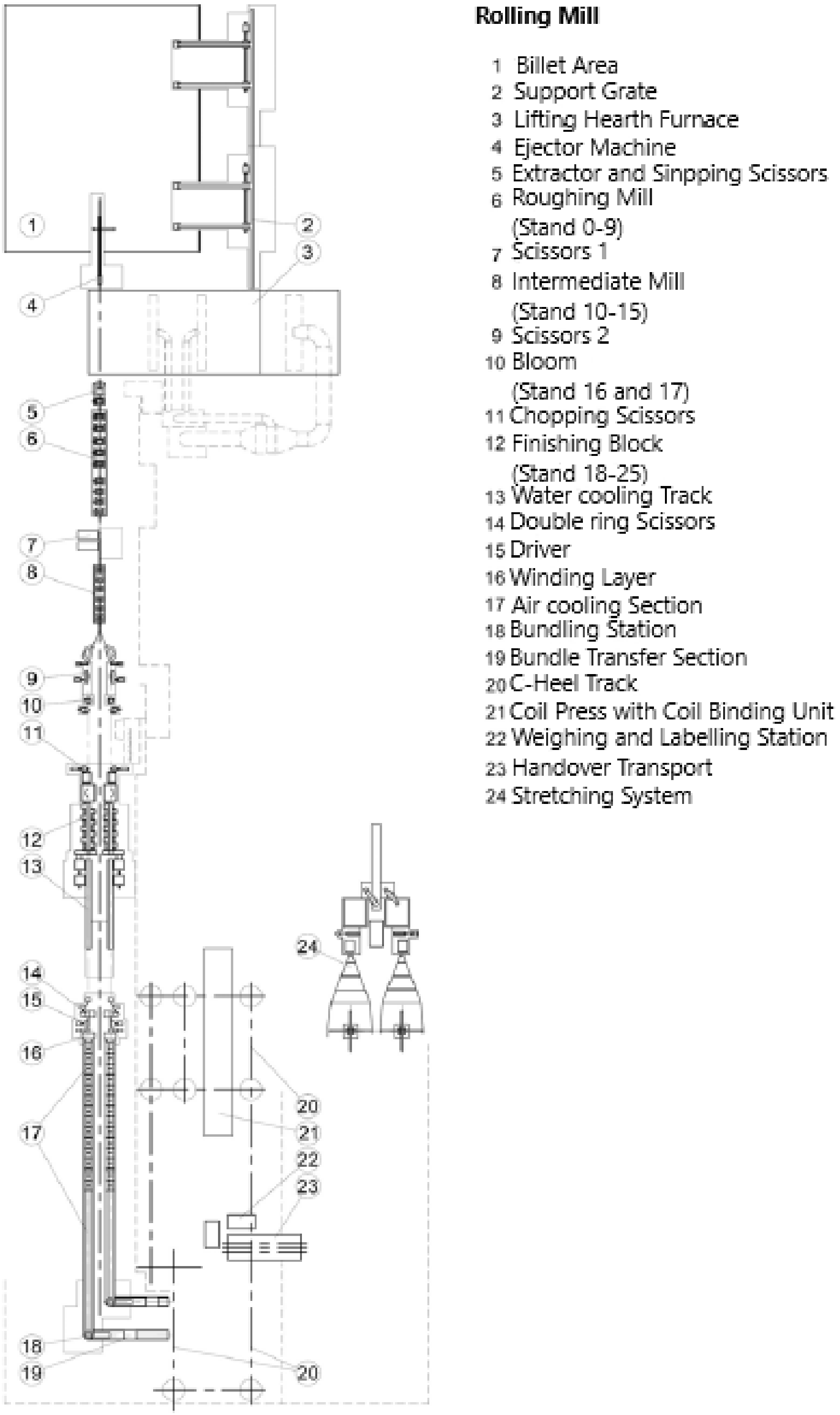

Figure 2-5: Diagram of Wire Rod Mill for ArcelorMittal Hamburg [1]

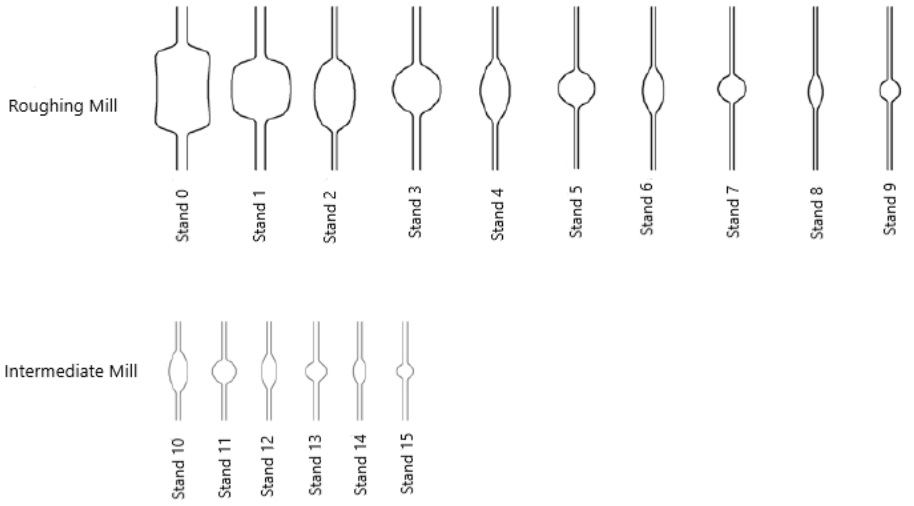

Figure 2-6: Groove shapes for Roughing and Intermediate Mills ArcelorMittal Hamburg (By Author)

of the rolled material are large in dimensions than the middle of the wire rod. The shear cuts the head and tail of the wire rod to ensure that the desired dimension of the wire rod is maintained. When a malfunction in the roughing mill occurs, the shear cuts the wire rods to ensure the safety of the personnel.

Finishing Mill

After the intermediate mill, the two lines are separated over a riding section and fed to the loop tables. The loop tables form a compensating section. The loop table ensures the rolling stock is free of drafts between the central train and the bloom. It also compensates for speed surges. The drives of stands 16 and 17 regulate the loop's height. These stands are called bloom and differ from the roughing and intermediate mill stands. In these stands, the rolls are smaller in size. The decrease in the wire rod size is around 15% from stand to stand. A large loop table after the blooms regulates the path of the wire rod in the finishing block.

The finishing block consists of 8 stands arranged in a V-shape to avoid twisting the rolling material due to the smaller wire rod size and significant speeds(around 100 m/s). The stands are therefore inclined at 45° to each other. Two DC machines, each with an output of 1.5 MW, drive the stands of the finishing block.

Water Cooling Section

When the wire rod leaves the finishing block after being deformed into the final desired dimensions, its temperature is around 900° C. The wire rod then enters the water cooling section, consisting of eight cooling pipes circulating water around the wire rod. The cooling of the wire rod influences the structure and technological properties of the wire rod. With a precisely regulated water cooling system, the passing wire rod having a speed of 100 m/s cools down to 700° C within approximately 0.3s. Therefore, the water pressure and the cooling time are critical parameters for obtaining the required properties of the wire rod.

Double Ring Shear

The task of the double ring shear is to trim the wire rod after it passes the wire rod section. Due to the high speed (60 to 100m/s) and small dimension (9-15mm) of the wire rod, this task requires extreme precision at very high speeds.

Driver and Winding Layers

The firm Danieli installed the winding layers with upstream drifts in the rolling mill in 2008. The driver has the main task of ensuring that the wire rod is under tension, and if the dimensions of the wire rod are significantly large, it should transport it to the winding layer.

The winding layer comprises a winding rotor operated by a frequency-controlled Alternating Current (AC) motor. A curved guide tube feeds the wire to the rotor. The high-speed rotation causes the wire to fall in turns on the winding conveyor belt.

Winding Conveyor Belt and Air Cooling Section

Due to the constant movement of the winding conveyor belt, the wire windings are fanned out and transported towards the coil forming station. Below the conveyor belt, there are 17 fan groups installed per roller core. A fan group consists of external, central, and internal fans. There are 133 fans with a total output of 1.5 MW and a volume flow of 3.1 million m/h. The fans help to reduce the wire's temperature from 700° C to a temperature in the range of 300-400 ° C. Alteration in the cooling is possible by changing the fan's activation according to different wire qualities. The air cooling section is also provided with covers that are required if there is a requirement for delayed cooling for some specific grades of wire. This section is shown below in Figure 2-7.

Coil formation and Coil Transfer Section

The coil formation station is at the end of the conveyor belt consisting of a rotatable, double collecting mandrel with a funnel and a cone.

The wire windings fall over the cone, into the funnel, and onto the collar plate. This section's speed is constantly controlled to ensure that the falling height is always constant, resulting in an enhanced packing density. The collecting mandrel rotates once the wire bundle formation is complete.

The next coil of wire falls onto a free mandrel, and a trolley transports the coil from the mandrel to the center of a C-hook track.

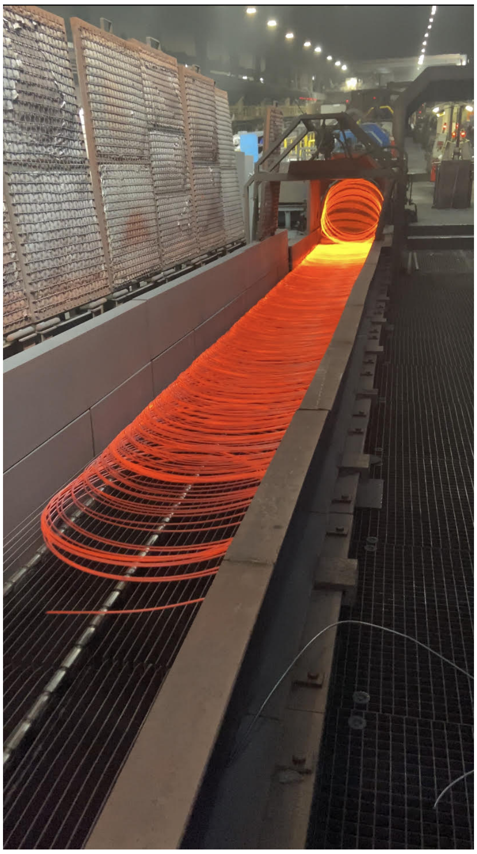

Figure 2-7: Conveyor Belt with Air Cooling Section ArcelorMittal Hamburg (By Author)

Trimming Station, Coil Press, Weighing and Labelling Station

The C-hook track transports warm coils to the trimming station, where manual trimming occurs. The warm coils created by a delayed activation of the water cooling section are not of the desired technological properties. After the trimming station, the wire is cut to a coil length of 1.20 m and tied with the help of 4 wires. Finally, the bundle is weighed and labelled with the help of a robot at the weighing and labelling station.

The chapter provided a fair understanding of the steel manufacturing process and the major subsystems involved in manufacturing and rolling steel at the ArcelorMittal Hamburg facility. It is important to understand these subsystems as they play an essential role in defining the quality of steel produced and its dimensional tolerances. The scope of this thesis focuses on the wire rod rolling facility. As described in the chapter, the looper and looper-less techniques are used to ensure stable operation in the rolling mill facility. The usage depends on which section of the rolling mill is under focus. The next chapter will dive deeper into the fundamental concepts of rolling. It will also provide a detailed description of the various components in the rolling process.

Chapter 3

Theoretical Background

This chapter provides a detailed explanation of the terminologies and components involved in the steel-making process. A comprehensive understanding of these is essential to understand the various disturbances that act on the system and how they would affect the stability of the steel rolling process. The chapter will also provide equations for theoretical analysis of the Finite-Element Method (FEM) based simulator results.

3-1 Steel Rolling Process

The process of hot steel rolling consists of hot metal being passed between two rolls to cause deformation in the metal. The hot metal is called workpiece, and the rolls are called work rolls. The work rolls move at a synchronous speed and in a direction opposite to the motion of the workpiece. The distance between the work rolls is called the roll gap. The roll gap is adjusted to less than the dimensions of the incoming workpiece.

The work rolls are mounted on a housing known as stands. The number of stands in a typical hot rolling mill varies between 17 and 21, depending upon the rolling mill's layout, design, and utility. Figure 3-1 shows a schematic diagram of the rolling process with three stands. It is also possible to have more than one line in a particular stand. This concept is called multi-line rolling and increases the production capacity but makes controlling the process quite complex. A schematic of the configuration of the roughing mill is shown in Figure 3-2.

When the workpiece passes through the roll gap, deformation in the workpiece takes place in a direction normal to the propagation of the workpiece. Deformation results in the downward movement of the grains in the workpiece, and hence a reduction of the cross-section area of the workpiece and elongation of the workpiece occurs. The deformation process follows the mass flow continuity equation (3-1). When the workpiece passes through the roll gap completely, a pass is said to the completed. There is an increase in the speed of the workpiece as it moves downstream in the rolling mill.

$$\dot{m}_{j-1} = \dot{m}_j = \dot{m}_{j+1} = \text{constant} \tag{3-1}$$

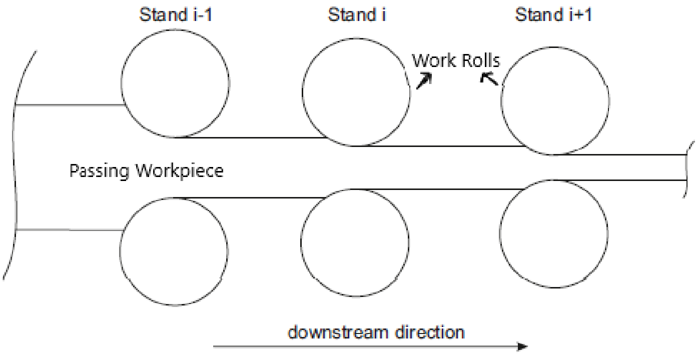

Figure 3-1: Schematic Diagram of rolling with 3 stands (By Author)

3-2 Concepts and Components of Steel Rolling Process

Figure 3-2 shows the configuration of the roughing mill. Each stand is powered by a Direct Current (DC) motor via a gearbox and shaft. Initial speed references (ω_{ref}) are set for each stand before the rolling process begins. The tuning of these setpoints is conducted during rolling. The speed reference is fed to a cascade control loop for the armature current and the motor speed. The values of the armature current i_a and field current i_f can be measured with the help of sensors.

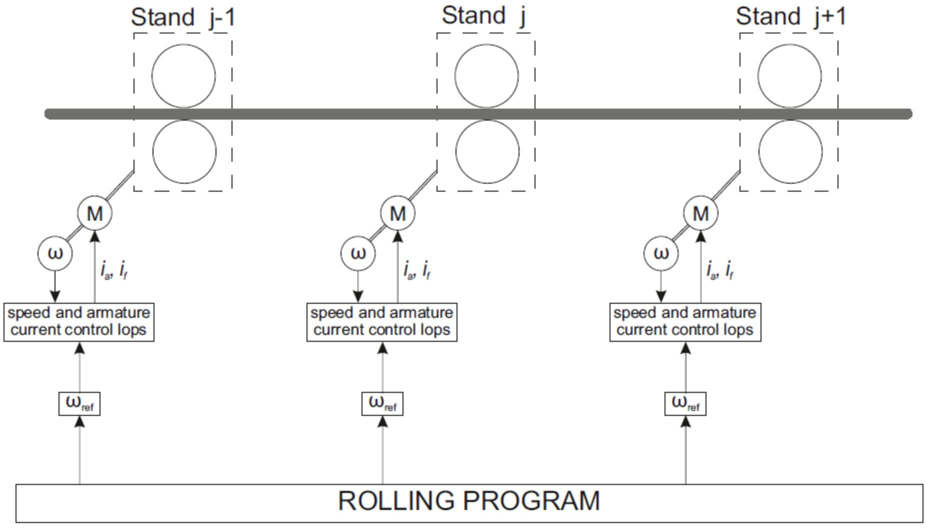

Figure 3-2: Schematic configuration of the roughing mill [3]

The quality of the end product depends on the tension between two consecutive rolling stands. In the case of the roughing mill, where no loopers are involved, the only option to regulate this inter-stand tension is to control the work roll's speed. The speed of the workpiece in the inter-stand gap is regulated by the regulation of the speed of the work rolls of the stands. Change in the speed of the motor of a particular stand results in the change of the work roll's speed of that stand. This consequently changes the tension in the passing workpiece.

Currently, the method used for controlling the speed around setpoints is based purely on the operator's experience.

When the rolling mill is started, and before any workpiece is introduced into it, a predetermined speed is calculated by the continuity equation (3-1) and provided to the motors of the stand as an initial setpoint. The speed setpoints, however, must be changed while rolling starts to ensure that the rolling process is stable.

An operator must manually check the workpiece's behavior to adapt the speed setpoints during rolling. This is done in the inter-stand section of stand j-1 and stand j by hitting the passing workpiece with a hammer-like instrument and observing the workpiece's behavior.

Once the hammer strikes the workpiece, it reacts in two possible ways. If the tension is low, the workpiece starts to oscillate and comes to rest. Consequently, the tension must be increased to ensure stable rolling mill operation. This can be done by decreasing the speed of the previous stand (stand j-1). If the tension is high, the workpiece will not react. The speed of the previous stand (stand j-1) will be increased to decrease the tension in the workpiece. This process is repeated for all the roughing and intermediate mill stands. Suppose the speed is updated for any of the stands. In that case, the speeds of the remaining stands have to be updated proportionally to ensure that the rolling process can continue safely and according to specifications and set tolerances. Generally, this entire process of setting speed setpoints takes up to 5 workpieces. However, the process must be repeated every time a new steel quality is rolled. This makes the process time-consuming and dependent on the operator's accuracy and assessment.

3-2-1 Motor

The motor drives belong to the group of separately excited DC motors. The motor consists of two main parts, a stator and a rotor. A magnetic field is produced in the windings of the stator and induces a magnetic flux in the rotor's windings. Due to the rotating magnetic field produced by the stator, the rotor starts to rotate, producing magnetic torque.

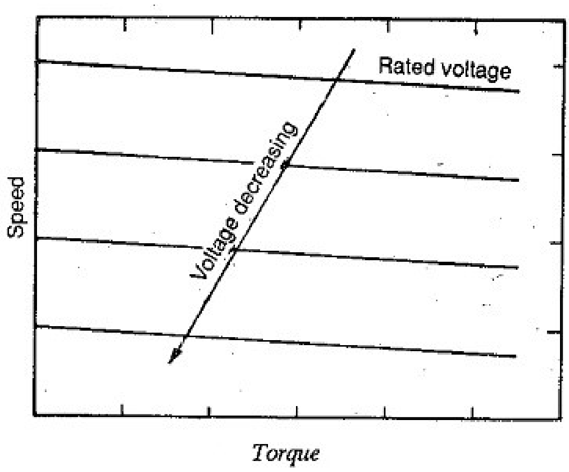

Figure 3-3: Speed Torque Characteristics for separately excited DC motor [4]

Separately excited DC motors for rolling are preferred due to their torque-speed characteristics, high performance, and flexibility. The torque-speed characteristics of the separately excited DC motor is a straight line in steady-state, Figure 3-3 [4]. This means that the motor will maintain a constant speed for any load exerted on the motor. This is highly desirable for rolling as constant speed will be maintained even when load torque changes rapidly at the entry and exit of the workpiece.

The stator and the rotor can be expressed in equivalent electrical circuits termed as the field (right side) and armature circuits (left side), respectively. Figure 3-4 shows the equivalent circuit of the motor. The smaller case depicts values in dynamic values, and the bigger case depicts steady-state values. When a voltage v_f is applied to the field circuit, field current i_f flows through the circuit. Due to the field current, a current i_a is induced in the armature circuit. According to Lenz's law, a back Electromotive Force (EMF) is induced in the armature circuit resulting in torque on the motor's shaft [5].

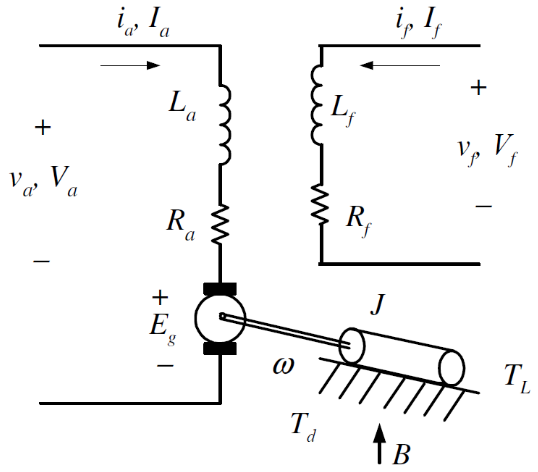

Figure 3-4: Electrical Circuit for separately excited DC motor [5]

Equation (3-2) depicts the relation for the field circuit, where R_f and L_f are the field circuit's resistance and inductance, respectively.

$$\mathrm{v}_f = \mathrm{R}_f i_f + \mathrm{L}_f \frac{di_f}{dt} \tag{3-2}$$

We have (3-3) for the armature circuit where, R_a, L_a, and E_g are the armature resistance, armature inductance, and dynamic back EMF.

$$\mathrm{v}_a = \mathrm{R}_a i_a + \mathrm{L}_a \frac{di_a}{dt} + \mathrm{E}_g \tag{3-3}$$

The back EMF generated depends on the speed of the motor ω, field current i_f, and motor voltage constant $\mathrm{K_v}$ and is expressed in (3-4).

$$\mathrm{E}_g = \mathrm{K_v} i_f \omega \tag{3-4}$$

The magnetic torque T_m produced by the motor is proportional to the field current i_f is expressed in (3-5), where $\mathrm{K_t}$ is called the motor torque constant.

$$\mathrm{T}_m = \mathrm{K_t} i_f i_a \tag{3-5}$$

Equation (3-5) can be written as shown in (3-6), where ϕ_m is the magnetic flux in the motor.

$$\mathrm{T}_m = \mathrm{K_t} \phi_m i_a \tag{3-6}$$

Using Newton's second law, we can get the mechanical equation of the motor as shown in (3-7). Here, $\mathrm{T_L}$ is the load torque, J_m is the Moment of Inertia (MOI) of the motor, T_d is the resultant torque developed by the motor, and B_m is the mechanical damping coefficient of the rotor. It is assumed in this relation that the friction is linear.

$$\mathrm{T}_d = \mathrm{J}_m \frac{d\omega_m}{dt} = \mathrm{T}_m - \mathrm{T}_L - \mathrm{B}_m \omega_m \tag{3-7}$$

Speed Control

Two types of controls are used for separately excited DC motor. They depend on the values of load torque and motor speed.

Armature control is applied when the armature voltage is less than the motor's rated voltage. The flux is held at a constant value for this method. The above scenario is possible when the load torques have low values. The normal operating range for the armature control method is in the range shown in (3-8), where $\mathrm{T_R}$ and $i_{a\mathrm{R}}$ are the rated torque and rated armature current, respectively [16].

$$-0.2 \leq \frac{\mathrm{T_L}}{\mathrm{T_R}} = \frac{i_a}{i_{a\mathrm{R}}} \leq 0.2 \tag{3-8}$$

Field control is applied to control the motor's speed for load torques that exceed the motor's rated torque. In field control, the field current is changed, resulting in the change of the motor's magnetic flux. The decrease in the motor's flux results in the motor's speed, as shown in (3-9). Equation (3-10) shows the desired ratio of flux for safe operation, where ϕ_R is the rated flux of the motor. The flux ratio should never increase 1 as this might result in over fluxing of the motor, causing saturation in the stator and rotor windings which ultimately causes the overheating in the motor and failure [16].

$$\frac{\omega_m}{\omega_{m\mathrm{R}}} = \frac{1}{\mathrm{b}} \frac{v_a}{v_{a\mathrm{R}}} - \frac{1}{\mathrm{b}^2} \frac{\mathrm{T_L}}{\mathrm{T_R}} \tag{3-9}$$

$$\mathrm{b} = \frac{\phi}{\phi_\mathrm{R}} \leq 1 \tag{3-10}$$

DC Motor Model

System identification techniques do not have good results for capturing the behaviour of the motor. Therefore, a method is proposed by Karabegovic [3]. It has separate designs for mechanical and armature circuits and two controllers in a cascade configuration. The inner loop controls the armature circuit, and the outer loop controls the speed. The cascade configuration is considered with the assumption that the dynamics of the inner loop are faster than the outer loop. This holds for the DC motors because the time required for the armature current to achieve its setpoint is much faster than the time required for the motor to reach the speed setpoint. A simplified block diagram for the cascade control configuration is shown in Figure 3-5. Figure 3-6 shows the block diagram of the electro-mechanical part of the DC motor.

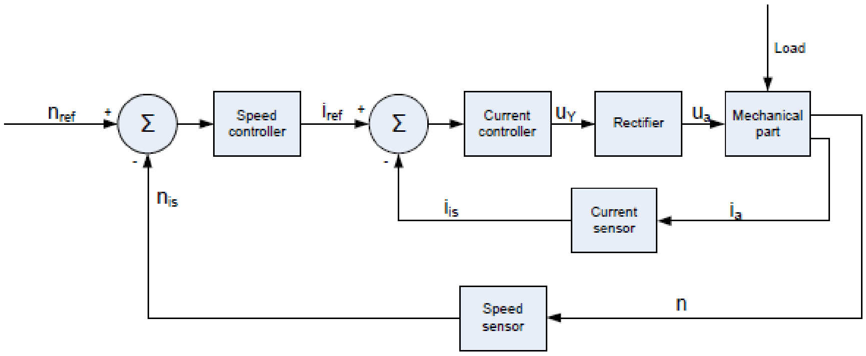

Figure 3-5: Block Diagram for cascade control DC Motor [3]

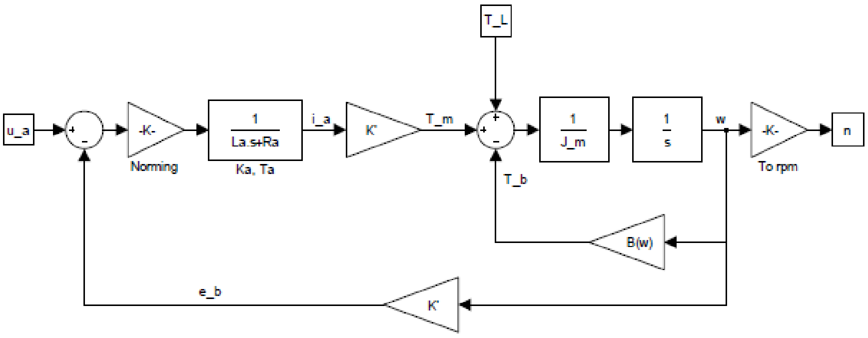

Figure 3-6: Block Diagram for Electro-Mechanical part of DC Motor [3]

Equation (3-11) depicts the relationship between the armature current and torque with constant magnetic flux ϕ_m.

$$\mathrm{T}_m = \mathrm{K}' i_a \tag{3-11}$$

Equation (3-12) shows the armature voltage generated by the rectifier circuit, where $\mathrm{U}_{\max}$ is the maximum output voltage of the rectifier and u_{Y_n} is the normed value of voltage set by the current controller.

$$u_a = \mathrm{U}_{\mathrm{max}}\mathrm{Sin}\left(\frac{\pi}{2}u_{Y_{\mathrm{n}}}\right) \tag{3-12}$$

3-2-2 Work Rolls

Work rolls are the tools used to reduce the cross-section of the workpiece and are generally made of steel alloys and can weigh up to 250 tonnes [17].

While rolling, there is significant wear and tear in the work rolls due to the high temperatures of the passing workpiece and high forces acting during the deformation process. The wear and tear in the work rolls considerably impacts the exiting workpiece's quality. Therefore, after several hundred tonnes of rolled workpieces, the mill has to be stopped, and the work rolls are replaced.

The most significant factor in the degradation of the performance of the work rolls over time and tonnage rolled is the change in diameter of the work rolls. The working diameter of the work roll is the diameter of the part that is in direct contact with the passing workpiece. In this zone, called the deformation zone, the work roll diameter is assumed to be reduced by 10%. Unfortunately, there is no technique or device to measure this momentary change in diameter while the work roll is in contact with the passing workpiece in the deformation zone.

The diameter of the work rolls is significant for calculating the speed of the work rolls and, consequently, the DC motor's speed setpoints. The DC motor is connected to the work rolls through mechanical gears. To ensure that the speed of the work rolls is constant as time progresses, the change in the diameter of the work rolls has to be compensated accordingly by changing the gear ratio. The gear ratio is a ratio that determines the transfer of speed from the DC motor to the work rolls.

Equation (3-13) shows the relationship between the motor speed ω_{m} in rpm and the tangential velocity of the work roll v, where g is the gear ratio of the mechanical gears, j is the stand number, and D is the diameter of the work rolls.

$$\mathrm{v}_j = \frac{2\pi}{60}\frac{\mathrm{D}_j}{2}\frac{1}{\mathrm{g}_j}\omega_{\mathrm{m}_j} \tag{3-13}$$

3-2-3 Workpiece

The steel workpiece passes through each stand's pair of work rolls in sections of the roughing and intermediate mills undergoing a deformation process at each stand [17].

The modelling of the rolling process is a very challenging task for rolling experts. Most of the programs used to optimize the process are either based entirely on empirical data or practical experience of the mill operators [18]. A new method using FEM for modelling hot and cold rolling was presented in the doctoral thesis of Shunxin Zhou. The method was used to model re-crystallization, grain growth, temperature influence, and residual strains. Prior to this, efforts had been made to simulate the process of sheet rolling (flat rolling) using Finite Element Analysis (FEA) techniques [19–22]. Authors Abhijit Chandra and Subrata

Mukherjee present a series of papers that use the Boundary Element Method (BEM) to model the rolling process [23–25]. Although detailed research has been carried out, many effects have still not been studied for the flat rolling process. The literature on wire rod rolling is even more scarce.

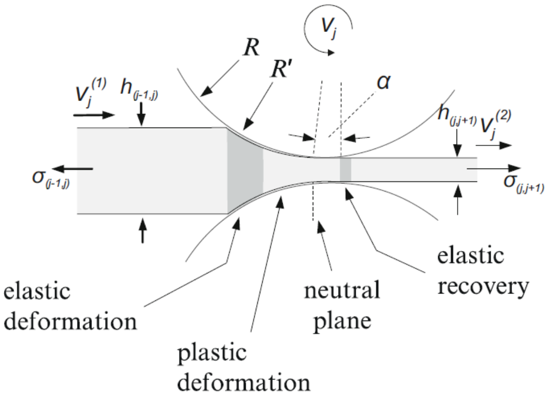

Figure 3-7: Variables in the deformation process [6]

A view of the deformation process and the crucial variables are shown in Figure 3-7. The figure depicts the case of sheet metal rolling (flat rolling), but the basics do not change for wire rod rolling. The stand number is represented by the letter j. $j-1$ and $j+1$ represent the previous and next stands. $(j-1, j)$ represents the inter-stand section between the previous stand and the current stand. Similarly, $(j, j+1)$ represents the inter-stand section between the current and next stand. The height and speed of the incoming workpiece into the rolling area (roll bite) are given by $\mathrm{h}_{(j-1,j)}$ and $\mathrm{v}_j^{(1)}$, respectively. Similarly, the same variables of the exiting workpiece are given by $\mathrm{h}_{(j,j+1)}$ and $\mathrm{v}_j^{(2)}$. The tension in the incoming workpiece is given by $\sigma_{j-1,j}$ existing in the inter-stand section $(j-1, j)$. Similarly, the tension in the exiting workpiece is given by $\sigma_{j,j+1}$ existing in the inter-stand section $(j, j+1)$.

During the deformation in the deformation zone, the work roll undergoes elastic flattening, as mentioned in the previous section. The radius of the work roll changes from R to R′. There is a speed difference between the flattened work roll and the workpiece except for a small region in the roll bite. This region is termed the neutral plane, and in this region, the speed of the workpiece of the speed of the work roll is synchronised. Before the neutral plane, the speed of the work roll is greater than the workpiece, and the opposite holds after the workpiece crosses the neutral plane.

In the deformation zone, the workpiece's shape changes due to vertical strains on the workpiece, causing elastic deformation. In most of the literature available, this elastic deformation is assumed to be plastic. In reality, there is a slight elastic recovery in the workpiece [26].

Neutral Plane

The angle α indicates the position of the neutral plane in Figure 3-7. It is measured with respect to the vertical diameter of the work roll. It can be theoretically calculated as shown in (3-14), where $\mathrm{K_{Wm}}$ is the average forming resistance [3].

$$\begin{aligned}\alpha =&\sqrt{\frac{\mathrm{h}_{(j,j+1)}}{\mathrm{R}'}}\cdot\tan\left\{\frac{1}{2}\left[\arctan\sqrt{\frac{\mathrm{h}_{(j-1,j)}}{\mathrm{h}_{(j,j+1)}}-1}+\right.\right.\\&\left.\left.+\sqrt{\frac{\mathrm{h}_{(j,j+1)}}{\mathrm{R}'}}\left(\frac{\sigma_{(j,j+1)}-\sigma_{(j-1,j)}}{\mathrm{K}_{\mathrm{Wm}}}\right)-\ln\frac{\mathrm{h}_{(j-1,j)}}{\mathrm{h}_{(j,j+1)}}\right]\right\}\end{aligned} \tag{3-14}$$

The entry and exit speed of the workpiece can be calculated using the mass flow continuity equation, shown in (3-1). According to that, the mass flow is always the same, i.e., before the entry of the workpiece into the work rolls, when the workpiece is inside the work rolls, and after the workpiece exits the workpiece. Equation (3-1) can be written as shown in (3-15), where ρ is the density of the workpiece, h_j and s_j is the height and length of the workpiece at a given point inside the roll bite, respectively, a is the width of the workpiece and remains the same only in the case of flat rolling.

$$\dot{m}_j = \rho\frac{d\left(\mathrm{a}\mathrm{h}_j\mathrm{s}_j\right)}{dt} = \text{ const.} \tag{3-15}$$

Considering that the height and density of the workpiece (workpiece is considered to be a sheet instead of a wire rod) remain the same, (3-15) can be simplified, as shown in (3-16). Consequently, (3-17) follows where h_α is the height of the workpiece at the neutral plane.

$$\frac{d\left(\mathrm{h}_j\mathrm{s}_j\right)}{dt} = \mathrm{h}_j^{(x)}\mathrm{v}_j^{(x)} = \text{const.} \tag{3-16}$$

$$\mathrm{h}_j^{(x)}\mathrm{v}_j^{(x)} = \mathrm{h}_\alpha\mathrm{v}_j = \mathrm{h}_{(j-1,j)}\mathrm{v}_j^{(1)} = \mathrm{h}_{(j,j+1)}\mathrm{v}_j^{(2)} \tag{3-17}$$

When the values of the height of the workpiece are known at the neutral plane, before and after the roll bite, the entry and exit speeds of the workpiece can be calculated as shown in (3-18) [3].

$$\begin{aligned}\mathrm{h}_\alpha &= \mathrm{h}_{(j,j+1)} + 2\mathrm{R}'(1-\cos\alpha) = \mathrm{h}_{(j,j+1)}\left[1+2\frac{\mathrm{R}'}{\mathrm{h}_{(j,j+1)}}(1-\cos\alpha)\right]\\ \mathrm{v}_j^{(1)} &= \frac{h_\alpha\mathrm{v}_j}{\mathrm{h}_{(j-1,j)}} = \mathrm{v}_j\frac{\mathrm{h}_{(j,j+1)}}{\mathrm{h}_{(j-1,j)}}\left[1+2\frac{\mathrm{R}'}{\mathrm{h}_{(j,j+1)}}(1-\cos\alpha)\right]\\ \mathrm{v}_j^{(2)} &= \frac{\mathrm{h}_\alpha\mathrm{v}_j}{\mathrm{h}_{(j,j+1)}} = \mathrm{v}_j\left[1+2\frac{\mathrm{R}'}{\mathrm{h}_{(j,j+1)}}(1-\cos\alpha)\right]\end{aligned} \tag{3-18}$$

Forward and Back Slip

The forward and backward slip coefficients connect the workpiece's entry and exit speed to the roll's speed. These can be easily determined using (3-19).

$$\lambda_{\mathrm{f}} = \frac{\mathrm{v}_j^{(2)} - \mathrm{v}_j}{\mathrm{v}_j}$$
$$\lambda_{\mathrm{b}} = \frac{\mathrm{v}_j - \mathrm{v}_j^{(1)}}{\mathrm{v}_j} \tag{3-19}$$

3-3 Equations for Theoretical Analysis

G.S. Nikitin covers the equations of the rolling process under the influence of inter-stand tension in the rolling mill for a wide variety of different rolling mill configurations [27]. It also provides details for drawing processes under the influence of inter-stand tension. The inter-stand tension developed in the rolling mill is a direct consequence of speed mismatch in the stands of the rolling mill. As a result, the equations presented in the book apply to the study of speed mismatch conducted in the thesis work and provide a basis for conducting a theoretical analysis to compare the results obtained during the FEM-based simulations in Chapter 4.

The deformation of the workpiece during rolling in the deformation zone at a particular stand is given by (3-20). The deformation in the workpiece depends on the friction between the work roll and the workpiece and the bite angle. These fields can be calculated using the relations shown in (3-21) and (3-22), respectively.

$$\delta = \frac{2 \cdot \mathrm{f}}{\alpha} \tag{3-20}$$

Here:-

f is the coefficient of external friction

α is the bite angle

The external coefficient of friction for a specific stand is calculated as shown in (3-21). The friction for the specific stand depends on the material composition for the work rolls and the temperature of the workpiece. For coal-based work rolls, the factor k_1 has a value of 0.8, and for steel-based work rolls, a value of 1. Equation (3-21) is used when the rolling speed of the workpiece is less than 1 m/s. At higher speeds, the expression needs to be modified to inculcate the influence of the rolling speed.

$$\mathrm{f} = \mathrm{k}_1(1.05 - 0.0005\mathrm{T}) \tag{3-21}$$

Here:-

T is the temperature of the workpiece

$\mathrm{k}_1 = 1$ for steel

The bite angle for a particular stand is given by (3-22). The bite angle, also known as the capture angle, is the angle between the point where the workpiece comes in contact with the work roll and the projection of the center of the work roll on the surface. The bite angle demarcates the beginning of the deformation zone.

$$\alpha = 2 \arcsin \sqrt{\frac{\mathrm{H_0} - \mathrm{H_1}}{2\mathrm{D_k}}} \tag{3-22}$$

Here:-

$\mathrm{H_0}$ is the height of the workpiece before entry into the stand.

$\mathrm{H_1}$ is the height of the workpiece after exiting from the stand.

$\mathrm{D_k}$ is the work roll diameter of the stand.

In the deformation zone, the workpiece undergoes plastic deformation. Due to deformation, the dimensions of the workpiece change. The change in the area of the workpiece before it enters the deformation zone and after it exits is a good measure of the deformation that occurred in the workpiece at a particular stand. The ratio of these areas, called the deformation ratio is calculated by (3-23).

$$\lambda = \frac{\mathrm{A}_{0j}}{\mathrm{A}_{1j}} \tag{3-23}$$

Here:-

A_{0j} is the area of the workpiece before entry into the j-th stand.

A_{1j} is the area of the workpiece after exiting from the j-th stand.

The lead of metal in a particular stand is defined as the excess speed of the workpiece after exiting a particular stand compared to the circumferential speed of the work roll of the particular stand. The lead of metal is calculated as shown in (3-24).

$$\mathrm{S} = \frac{\mathrm{v} - \mathrm{v_r}}{\mathrm{v_r}} \tag{3-24}$$

Here:-

v is the exit speed of the workpiece from the stand.

$\mathrm{v_r}$ is the work roll speed of the stand.

A speed mismatch needs to be created to study the effect of speed mismatch in rolling stands on the technological parameters during steel rolling. The speed mismatch is given by (3-25). The speed of a particular stand in case there is no speed mismatch is calculated using the theoretical speed of the rolling and the diameter of the work roll of that particular stand. This speed is called the coordinated speed. In case there is no speed mismatch (an ideal case), the coordinated speed should be equal to the current speed of the stand.

$$\frac{\mathrm{n}_\phi - \mathrm{n_{coordinated}}}{\mathrm{n_{coordinated}}} 100\% \tag{3-25}$$

Here:-

n_ϕ is current speed of the work rolls.

$\mathrm{n_{coordinated}}$ is the speed of the work rolls in the coordinated mode.

A direct consequence of speed mismatch in rolling stands is the development of tension in the workpiece. These tensions, namely the front tension σ_1, and the rear tension σ_0, are calculated by the formula shown in (3-26). These tensions are calculated for a particular rolling stand. The front tension is created in the workpiece's area towards the stand's exit. The rear tension is created in the workpiece's area before the stand's entry.

$$\sigma_{1j} = \sigma_{0j+1} = \frac{1}{0.045}\left\{\left[\left(\frac{\mathrm{n}_{j+1}}{\mathrm{n}_j}\right)_{\phi} - \left(\frac{\mathrm{n}_{j+1}}{\mathrm{n}_j}\right)_{\text{coordinated}}\right]\frac{\mathrm{D}_{\mathrm{k}j+1}}{\mathrm{D}_{\mathrm{k}j}} \cdot \frac{1}{\lambda_{j+1}} \cdot \frac{1+\mathrm{S}_{j+1}}{1+\mathrm{S}_j}\right\} \tag{3-26}$$

The resultant tension in a particular stand is given by (3-27).

$$\sigma_{\Sigma j} = \sigma_{0j} - \sigma_{1j} \tag{3-27}$$

The tension in the entire workpiece area due to a particular stand is calculated as shown in (3-28).

$$\begin{aligned}\mathrm{T}_{0j} &= \sigma_{0j} \cdot \mathrm{A}_{0j}\\ \mathrm{T}_{1j} &= \sigma_{1j} \cdot \mathrm{A}_{1j}\end{aligned} \tag{3-28}$$

Due to speed mismatch, tension is created in the workpiece, as explained before. This creation of tension causes the rolling moment of a particular stand to change. This change of the rolling moment of a stand is calculated as shown in (3-29).

$$\Delta\mathrm{M} = \frac{\mathrm{F_k l_c}}{\frac{1}{\eta} - 1} \cdot \sigma_{\Sigma j} \tag{3-29}$$

Here:-

$\mathrm{F_k}$ is the projection area of the contact surface between the rolls and the rolled material. It is calculated as shown in (3-30).

$$\mathrm{F_k} = \frac{\mathrm{B}_0 + \mathrm{B}_1}{2} \cdot \mathrm{l_c} \tag{3-30}$$

Here:-

B_0 is the width of the workpiece before entering the stand

B_1 is the width of the workpiece after exiting the stand

$\mathrm{l_c}$ is the length of the deformation zone given by (3-31).

$$\mathrm{l_c} = \sqrt{\frac{(\mathrm{H}_0 - \mathrm{H}_1)\,\mathrm{D_k}}{2}} \tag{3-31}$$

The change in the rolling moment of a particular stand has a consequent effect on the work roll pressure acting on the workpiece. The change in the work roll pressure on the workpiece is calculated using (3-32).

$$\Delta \mathrm{p} = -\left\{\left[\left(\frac{1}{\eta} - \frac{1}{\eta}^{\frac{\delta-1}{2\delta}}\right)\frac{\sigma_{0j}}{\frac{1}{\eta}-1}\right] - \left[\left(\frac{1}{\eta}^{\frac{\delta-1}{2\delta}} - 1\right)\frac{\sigma_{1j}}{\frac{1}{\eta}-1}\right]\right\} \tag{3-32}$$

In (3-32), η is expressed in (3-33), as shown below.

$$\frac{1}{\eta} = \frac{\mathrm{H_1}}{\mathrm{H_0}} \tag{3-33}$$

Here:-

$\mathrm{H_0}$ is the initial workpiece height.

$\mathrm{H_1}$ is the final workpiece height.

The torque on a particular stand is calculated as shown in (3-34). The torque calculated using (3-34) will be used to compare the results obtained from the FEM simulations in Chapter 4.

$$\mathrm{M_H} = \frac{\mathrm{D_k}}{2}\left(\frac{\mathrm{T_0}}{\lambda} - \mathrm{T_1}\right)(1+\mathrm{S}) \tag{3-34}$$

After a detailed explanation of the critical concepts and components of the rolling mill, the upcoming chapter focuses on the FEM-based simulations, the setup of the simulator, and verification of the results obtained from the simulations using the theoretical equations presented in the last section of this chapter. The results from the FEM simulations conducted in the upcoming chapter, along with the results presented in Chapter 6, answer the first research question of the master thesis.

Chapter 4

Finite Element Method (FEM)-based simulator

The most widespread way of studying the phenomenons of metal forming is based on Finite-Element Method (FEM) simulations. Currently, various software packages allow for the creation of simulations for metal forming processes using 2-D and 3-D-based FEM models. Some renowned software packages are DEFORM-2D / 3D, QForm 2D/ 3D, PAMSTAMP 2D, SuperForm, and SuperForge.

For the FEM-based simulations conducted in this thesis, the QForm 3D software package was used. Appendix A explains in detail the mathematical formulation of the Finite- Element (FE) problem in the software package and how the plastic deformation problem is solved. The first section of the chapter will delve into the setup of the simulator for the thesis. The second section of the chapter provides the reader with an in-depth view of the simulation results obtained from the FEM simulations. The results in this section are then further used to obtain a regression model explained in Chapter 6. The last section of the chapter verifies the results obtained through the FEM simulations using theoretical equations described in Section 3-3.

4-1 Simulator Setup

Setting up a simulation model in QForm starts with creating a solid model of the components of the rolling process, namely the workpiece and the work rolls. The first part of obtaining a solid model is the creation of volumetric solids.

4-1-1 Creating 3D Models

A Computer-Aided Design (CAD) software is used for creating volumetric solids, in our case, Fusion 360. Fusion 360 is a cloud-based 3D modeling, CAD, Computer-Aided Manufacturing (CAM), and Printed Circuit Board (PCB) software platform for product design and manufacturing.

The 3-D models of the work rolls and workpiece were created using the data from the Drawings Archives of ArcelorMittal Hamburg. The drawings in the database at our use-case facility contained technical drawings of the work rolls and workpiece. The process of converting these 2-D sketches into 3-D models will be explained in detail in this section.

Work Rolls

For the FEM simulations, the models for stand 0 to stand 4 must be created to provide a more realistic representation of the rolling simulations. The part significant to the thesis would be the characteristics of workpiece deformation and its effect on the power parameters of stands 2, 3, and 4. Another reason for creating a simulation including stands up to 4 is the inability to measure or estimate the profile of the workpiece post deformation from the initial stands. Table 4-1 shows the data for stands from the Drawing Archives of ArcelorMittal Hamburg [7]. Table 4-2 shows the roll gaps between the work rolls, the working diameters, and the linear speed of the rollers.

Table 4-1: Work Roll Dimensions [7]

Stand Number	**Groove Shape**	**Height(Depth) Hg (in mm)**	**Groove Angle ag (in °)**	**Relief Radius R0 (in mm)**	**Bottom Radius R1 (in mm)**	**Bottom Radius R2 (in mm)**	**Width at collar Wg (in mm)**	**Top Width Wt (in mm)**	**Roll Diameter D (in mm)**
0	Box	35	16.5	10	20	-	154.09	133.35	560
1	Box Oval	40	19.5	10	20	180	108.51	85.45	530
2	Oval	28.5	-	10	130	-	-	-	505
3	Round	33	60	8	41	-	85.45	-	460
4	Oval	21.426	-	10	71.554	-	-	-	460

Figures 4-1, 4-2, and 4-3 show the technical drawing, 2-D sketch, and 3-D profiles created in Fusion 360 for Stand 0 [7]. A 2-D sketch of half the work roll was created based on the technical drawing of the work roll in Fusion 360. After this, an axis was created at an arbitrary position. The 2-D sketch is revolved around this axis to create the 3-D profile of the work roll. The 3-D profile obtained will be a solid model for the Qform simulation environment. Similar figures showing the technical drawings, sketches, and profiles can be found in Appendix C.

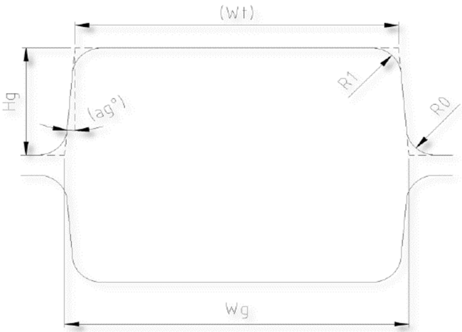

Figure 4-1: Technical Drawing for Stand 0 [7]

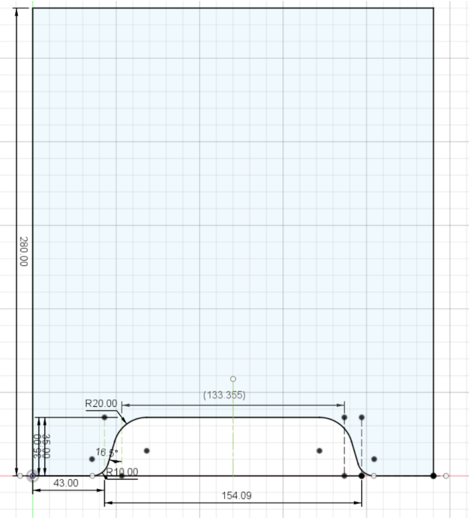

Figure 4-2: 2-D Sketch for Stand 0 (By Author)

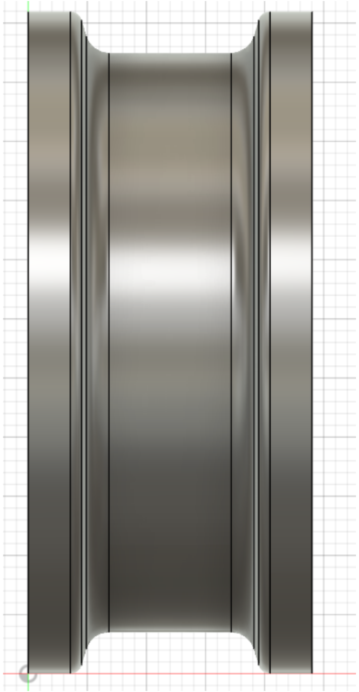

Figure 4-3: 3-D Profile for Stand 0 (By Author)

Workpiece

The standard workpiece used as an input to the rolling mill at the use-case facility is 130 × 130 × 16000 mm. The profile of the workpiece is a cuboid, and its dimension is a standard workpiece size at the billet-caster at the use-case facility. The workpiece is created by forming a two-point rectangle of the dimension 130 × 130 mm. The extrude command extrudes the dimension up to the workpiece's length and generates a volumetric solid, as shown in Figure 4-4. This solid will be used as a model for the workpiece in the Qform environment.

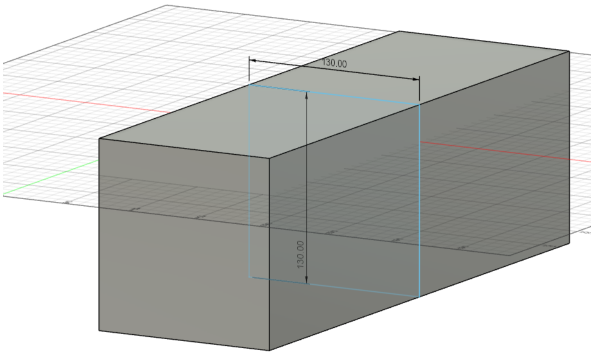

Figure 4-4: Profile for Workpiece (By Author)

4-1-2 QForm Environment Setup

The 3-D models created in Fusion 360 are divided into finite elements in the QShape program. The 3-D models must be saved in the ".step" format to enable this division.

After this, the models can be loaded into QShape. Selecting the "Shell0" object and generating a mesh of the 3-D object is essential. After this, the object can transform into a tool(work roll) or a workpiece. Select the "TOOL" option and the "WPIECE" option for the workpiece to create the work rolls.

The tool rotation axis needs to be selected to define the rotation of the work roll in the QForm simulation. The options for rotation axis are OX, OY, or OZ. After selecting the axis, the coordinates of the point through which the selected axis passes need to be specified. This work roll has to be saved in the ".shl" format. This is the standard file format that is required by the QForm software.

Model formulation starts with setting the process type and the type of problem. A deformation process is established for the simulations, considering thermal processes in a 3-D problem.

The workpiece temperature is selected as 1050 ° C based on the data of the use-case facility's monitoring system called ibaAnalyzer. The temperature data in the ibaAnalyzer software is based on the instrumentation available at the use-case facility before the workpiece enters the rolling mill. The metallurgical material of the workpiece is selected as "ST37K" since it is the most widely produced steel in the year 2020 (based on tonnage produced) at the use-case facility. In QForm, the European standard for this steel grade is "S235J0". The availability of the steel grade in the default database of Qform allows us to use data from its database for critical values such as stress-strain characteristics for the simulation of the plastic deformation process.

In the tool parameters tab, the material of the work rolls must be specified as "H13 HRC50". The selection is based on the datasheet provided to the use-case facility by the work roll manufacturers. The drive type for the work roll is universal, with counter-clockwise rotation around the axis for the top work roll and clockwise rotation for the bottom work roll of a particular stand. This is in lieu with the configuration of the work rolls at the use-case facility. Since there is no use of lubricant during rolling at the use-case facility, the lubrication parameters in QForm are selected as "Unlubricated" with a friction factor of 0.8 according to the Siebel's friction law and a heat transfer coefficient of 10000 $\frac{W}{m^2.K}$. The selection of the friction factor and heat transfer coefficient values is based on the suggestions of experts from the QForm Group and varies with the type of lubricant. In the setup of the simulator, different lubricants can also be selected based on the type of rolling condition one has simulated. The work roll temperature is set to 45°C. This temperature selection is based on the experiments conducted by the author to measure the temperature of the work rolls at the use-case facility with the help of a thermal camera. The temperature of the work rolls was measured during an intermediary stop in the rolling process of the selected quality of steel grade at the use-case facility, enabling to obtain a close estimate of the work roll temperature during rolling. The experiment cannot be conducted during the rolling process due to the extremely high temperature of the workpiece, which poses a threat of fatal injuries to the experimenter and damages the thermal camera. The distance between the work rolls, also known as roll gap, is set according to Table 4-2 according to the setup of the use-case facility.

Table 4-2: Work Roll Parameters [7]

Stand No.	**Groove Shape**	**Roll Gap (mm)**	**Work Roll Diameters**		**Theoretical Speed (m/sec)**	**Work Roll Speed for Software (rpm)**
			Design Diameter (mm)	**Working Diameter (mm)**		
0	Box	16	560	490.66	0.264803	10.307
1	Box Oval	16	530	446.226	0.366186	15.672
2	Oval	8	505	449.672	0.505945	21.488
3	Round	11	460	392.842	0.66337	32.2507
4	Oval	7	460	415.504	0.90098	41.413

The speeds of the work rolls in the software need to be adjusted according to the theoretical speed of the workpiece at each stand in the rolling mill. The theoretical speed of the workpiece at each stand is calculated with the help of the internal proprietary software of the use-case facility. This speed is dependent on the steel grade of the workpiece and the desired cross-sectional area of the finished product. The work roll speed for the software is calculated by the relation shown in (4-1). The calculated speeds are shown in Table 4-2. These are the speeds when no speed mismatch is created between the work rolls.

$$V = \frac{2 \times \pi \times R \times N}{60 \times 1000} \tag{4-1}$$

Here:-

V is the theoretical speed of the workpiece (Observed from ibaAnalyzer, shown in Table 4-2)

R is the working roll radius of the work rolls (Can be calculated from Table 4-2)

N is the speed of the work rolls for the simulation (needs to be calculated from (4-1))

Boundary conditions in QForm have different purposes and can be set in a given area. The areas (mesh) can be of different shapes. In these simulations, the area is in the shape of a parallelepiped. In the existing problem, the boundary condition for the environment is Air with a temperature of 20°C. The boundary condition for the workpiece is the environment with which it is in contact. The ambient temperature for air was selected on the thermometer reading for the rolling mill at the use-case facility. The temperature is an average based on three readings taken at different phases of the day over a week.

The main requirements for the mesh generation algorithm present in the QForm software package are as follows:-

1. The mesh should ensure the movement of the elements along the border of the tool (work roll), including the areas where there is a change in the direction of metal flow. There should be several mesh nodes present near the border elements.
2. The mesh should be present in areas where metal flow is complex.
3. The mesh should be able to thicken in areas where high rate gradients exist.
4. The shape of the elements should tend to be an equilateral triangle to increase the stability of the calculations.
5. The density of mesh should be controlled. The user should be able to increase the number of elements without reducing the mesh quality. The increase in the number of mesh elements significantly increases the computation time of the problem.

Figure 4-5 shows the mesh in the deformation zone of the top work roll of stand 2. The mesh has a high density in the deformation zone, signifying the high gradients of strain rate in the deformation zone. The mesh elements are in the form of regular tetrahedrons, which ensures the stability of the calculations in the software. The total number of volumetric elements in the system is 1,713,330.

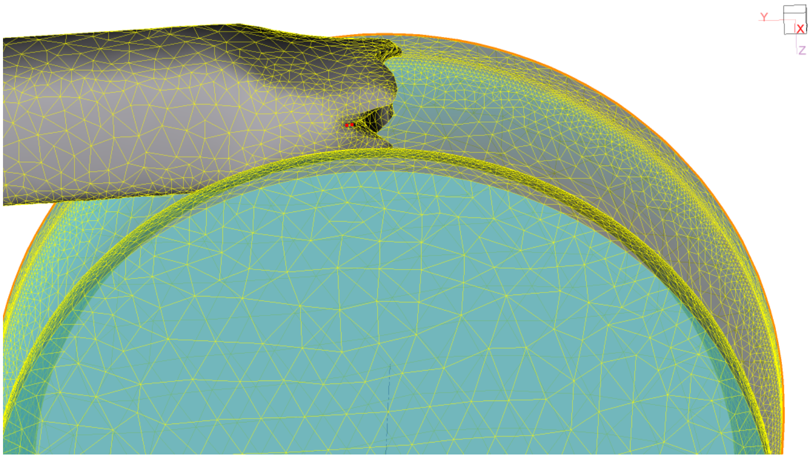

Figure 4-5: Mesh Elements in deformation zone (By Author)

Figure 4-6 shows the simulation setup in the QForm environment. The axis of rotation of alternate stands is aligned 90° to each other to replicate the conditions on the use-case facility. The workpiece is rotated by 90° post-deformation from a stand to ensure deformation occurs uniformly in the roughing mill section. The finishing mill and the second part of the intermediate mill at the use-case facility follow a similar technique of axis rotation for the work rolls. The workpiece is not rotated in the intermediate and the finishing mill since the speed of the workpiece is very high (more than 10 m/sec) and therefore poses a threat of severe injuries to personnel. To avoid the bending of the workpiece post-deformation from work rolls of stand 4, two additional stands that are a copy of stand 4 are used in the simulation. These are relief stands created to ensure stability during the rolling process. No deformation of the workpiece takes place in the relief stands.

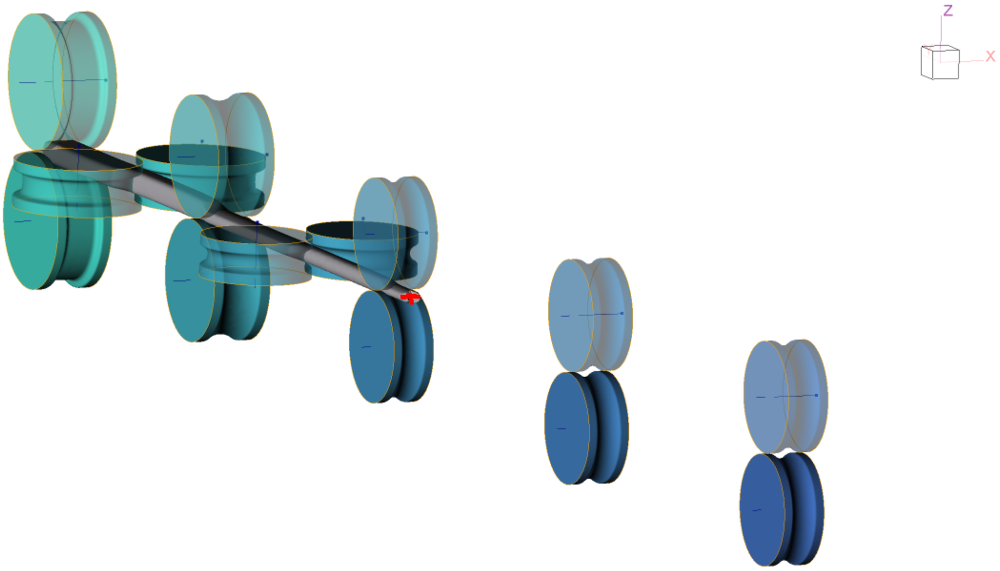

Figure 4-6: Rolling Simulation in QForm software package (By Author)

4-2 Simulation Results

The FEM simulations occur after the simulator has been set up, as explained in the previous section. This section shows the results obtained from the simulator according to a simulation plan generated by the author. The simulation plan was generated in consultation with experts from the use-case facility to include the most common and extreme cases of speed mismatches. The simulation plan is shown in Figure 4-7, where X1 and X2 correspond to the percentage of speed mismatch in stands 2 and 4, respectively, and be calculated as depicted in (3-25). The cases for which simulations have been conducted are highlighted by shading. Stand 3 is considered a reference stand, and its speed will not change throughout the simulations. According to the simulation plan, simulations in various scenarios are conducted. An analysis of the effect of speed mismatches in stands 2 and 4 on the technological parameters(load, power, and torque) of stand 3 is carried out.

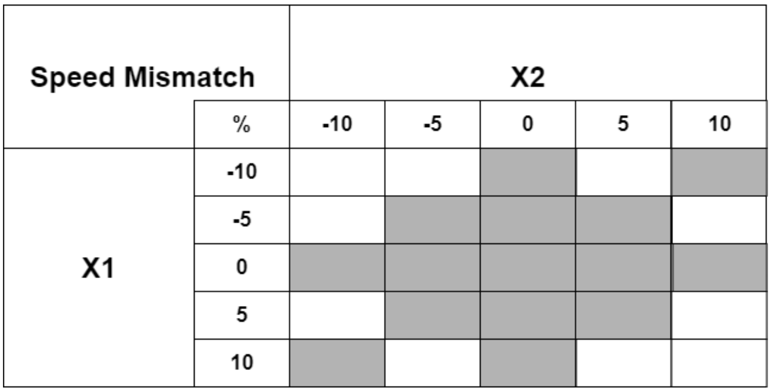

Speed Mismatch		X2				
	%	-10	-5	0	5	10
X1	-10			▨		▨
	-5		▨	▨	▨	
	0	▨	▨	▨	▨	▨
	5		▨	▨	▨	
	10	▨		▨		

Figure 4-7: Rolling Plan for Speed Mismatch Simulations (By Author)

Tables 4-3, 4-4, 4-5, 4-6, and 4-7 show the measurements taken from the software for the rolling modes:- (0,0), (-5,5), (-10,10), (5,-5) and (10,10) respectively. The rolling mode pair is in the form of (X1, X2). A cross-cut plane is created in the software using the "Set Cross-Cut Plane" option for these measurements. Then the dimensions of the workpiece after deformation from each stand are measured using the "Measure" option. The option allows the user to measure the workpiece's dimensions and area at any particular point in the workpiece.

Table 4-3: Dimension measurements of the workpiece in rolling mode (0,0)

Stand No.	**Workpiece Dimensions**			**Deformation Ratio**	**Work roll speed in software (rpm)**	**Work roll linear speed (m/sec)**
	Height (mm)	**Width (mm)**	**Cross Section Area** (mm^2)			
0	84.8136	145.18	11856.9	1.425	10.307	0.264803
1	94.172	95.3611	8387.85	1.413	15.672	0.366186
2	64.1302	108.97	6066.4	1.382	21.488	0.505945
3	71.5615	75.809	4471.54	1.356	32.2507	0.66337
4	49.8787	83.1647	3354.72	1.333	41.413	0.90098

The speeds of the stands in the rolling mode (0,0), as shown in Table 4-3, are the speeds denoted by $n_{\mathrm{coordinated}}$ in (3-25).

Table 4-4: Dimension measurements of the workpiece in rolling mode (-5,5)

Stand No.	**Workpiece Dimensions**			**Deformation Ratio**	**Work roll speed in software (rpm)**	**Work roll linear speed (m/sec)**
	Height (mm)	**Width (mm)**	**Cross Section Area** (mm^2)			
0	84.8136	145.18	11856.9	1.425	10.307	0.264803
1	94.172	95.3611	8387.85	1.413	15.672	0.366186
2	63.7891	113.193	6184.03	1.356	20.4136	0.48063
3	71.3386	75.4074	4396.01	1.406	32.2507	0.66337
4	49.456	79.4849	3297.11	1.333	43.483	0.946004

Table 4-5: Dimension measurements of the workpiece in rolling mode (-10,10)

Stand No.	**Workpiece Dimensions**			**Deformation Ratio**	**Work roll speed in software (rpm)**	**Work roll linear speed (m/sec)**
	Height (mm)	**Width (mm)**	**Cross Section Area** (mm^2)			
0	84.8136	145.18	11856.9	1.425	10.307	0.264803
1	94.172	95.3611	8387.85	1.413	15.672	0.366186
2	63.6513	120.29	6456.34	1.3	19.339	0.512295
3	67.3049	75.2961	4287.05	1.506	32.2507	0.750678
4	49.7083	78.334	3234.13	1.325	45.554	1.02605

Table 4-6: Dimension measurements of the workpiece in rolling mode (5,-5)

Stand No.	**Workpiece Dimensions**			**Deformation Ratio**	**Work roll speed in software (rpm)**	**Work roll linear speed (m/sec)**
	Height (mm)	**Width (mm)**	**Cross Section Area** (mm^2)			
0	84.8136	145.18	11856.9	1.425	10.307	0.264803
1	94.172	95.3611	8387.85	1.413	15.672	0.366186
2	63.6498	106.84	5934.71	1.413	22.562	0.530947
3	73.6316	75.2538	4575.83	1.3	32.2507	0.66337
4	49.5604	87.5102	3460.18	1.322	39.342	0.8554803

Table 4-7: Dimension measurements of the workpiece in rolling mode (10,-10)

Stand No.	**Workpiece Dimensions**			**Deformation Ratio**	**Work roll speed in software (rpm)**	**Work roll linear speed (m/sec)**
	Height (mm)	**Width (mm)**	**Cross Section Area (mm^2)**			
0	84.8136	145.18	11856.9	1.425	10.307	0.264803
1	94.172	95.3611	8387.85	1.413	15.672	0.366186
2	64.1636	104.089	5794.58	1.44	23.636	0.55622
3	76.5497	75.525	4637.72	1.3	32.2507	0.66337
4	49.388	91.2745	3568.6	1.3	37.271	0.810447

The values obtained for the technological parameters of stand 3 according to the simulation plan shown in Figure 4-7 are depicted below in Table 4-8, where "1*" depicts the case when the workpiece is present in stands 2 and 3 (measured at 8.16 seconds in the software), "2**" depicts when the workpiece is present in stands 2,3 and 4 (measured at 9.02 seconds in the software), and "3***" depicts when the workpiece is present in stands 3 and 4 (measured at 14.25 seconds in the software).

To further analyse the results obtained during the simulations, plots have been generated in MS-Excel.

Figure 4-8 depicts the loading of stand 3. When the speed of stand 2 decreases from the normal operating point (X1 negative) and the speed of stand 4 increases from the normal operating point (X2 positive), the load on stand 3 decreases. This is due to the pull on the workpiece under deformation from both sides because of the front and back tension forces and increases the tensile stresses within the workpiece and the normal force required to cause deformation decreases, thereby decreasing the loading of stand 3. When stand 2 is made to speed up (X1 positive) and stand 4 is slowed down (X2 negative), the tensile stress in the workpiece reduces and the force required to cause deformation increases. Hence, the loading of stand 3 increases.

Table 4-8: Technological Parameters for Stand 3

Speed Mismatch (%)		**Torque (KNm)**			**Power (KW)**			**Load (KN)**		
X1	**X2**	**1***	**2****	**3*****	**1***	**2****	**3*****	**1***	**2****	**3*****
0	0	20.14	15.64	17.38	68	52.8	58.7	424.3	403.9	402.2
-5	0	23.08	21.15	16.28	78	71.4	55	424.9	417	383.4
-5	5	23.06	14.34	7.76	77.9	48.4	26.2	427.9	378.8	342.8
0	5	21.42	13.29	9.26	72.4	44.9	31.3	418.3	378.3	344
-10	0	28.62	22.83	14.62	96.6	77.1	46.9	443.2	412.3	365.5
-10	10	28.38	41.17	2.2	95.8	47.9	7.4	433.3	350.2	314.5
0	10	21.39	9.18	1.81	72.2	31	6.1	429	342.9	311.2
5	0	17.06	14.63	15.98	57.6	49.4	54	431.2	429.2	381.8
5	-5	16.91	21.5	24.82	57.1	72.6	83.8	437.5	455.9	408.2
0	-5	20.6	24.21	24.13	69.6	81.8	81.5	427.7	447.4	402.8
10	0	12.15	13.04	25.01	41	44	84.5	422.1	455.2	394
10	-10	13.4	25.47	35.4	45.2	86	119.5	446.3	498.3	440.5
-5	-5	24.35	26.68	26.4	82.2	90.1	89.2	435	440	408
5	5	17.45	12.4	15.3	53.33	35.4	51.69	432	396	357
0	-10	20.98	28.66	30.71	70.9	95.6	103.7	429	469	414

Figure 4-9 depicts the torque of stand 3. When the speed of stand 2 is decreased (X1 negative) and the speed of stand 4 is increased (X2 positive), the load on stand 3 drops and causes the speed of the stand to increase. This reduces the torque produced on stand 3. On the other hand, when the speed of stand 2 (X1 positive) is increased and stand 4 (X2 negative) is slowed down, the load on stand 3 increases. This results in a speed drop in stand 3, increasing the torque generated on stand 3. This is in agreement with the speed-torque characteristics of a DC motor.

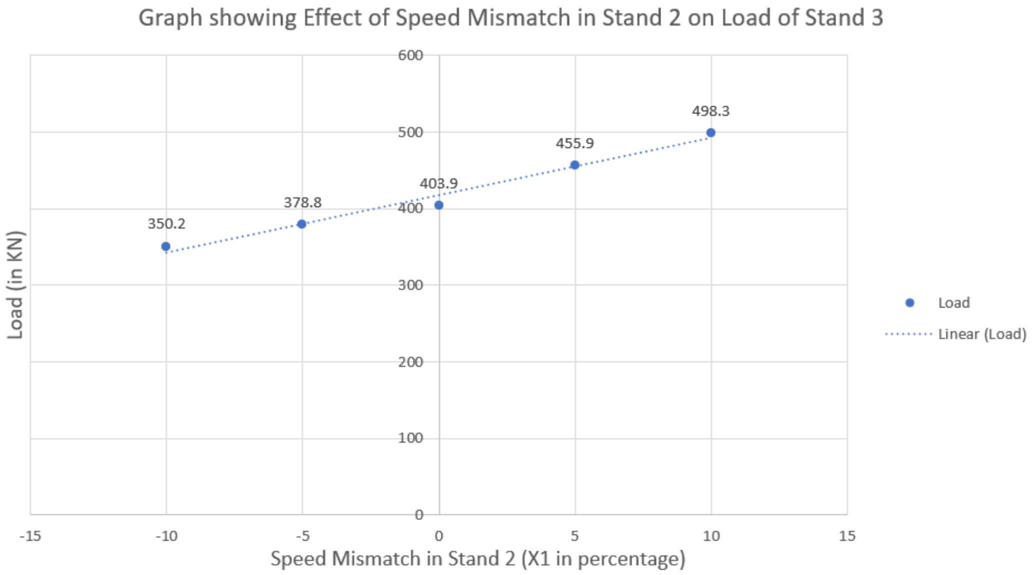

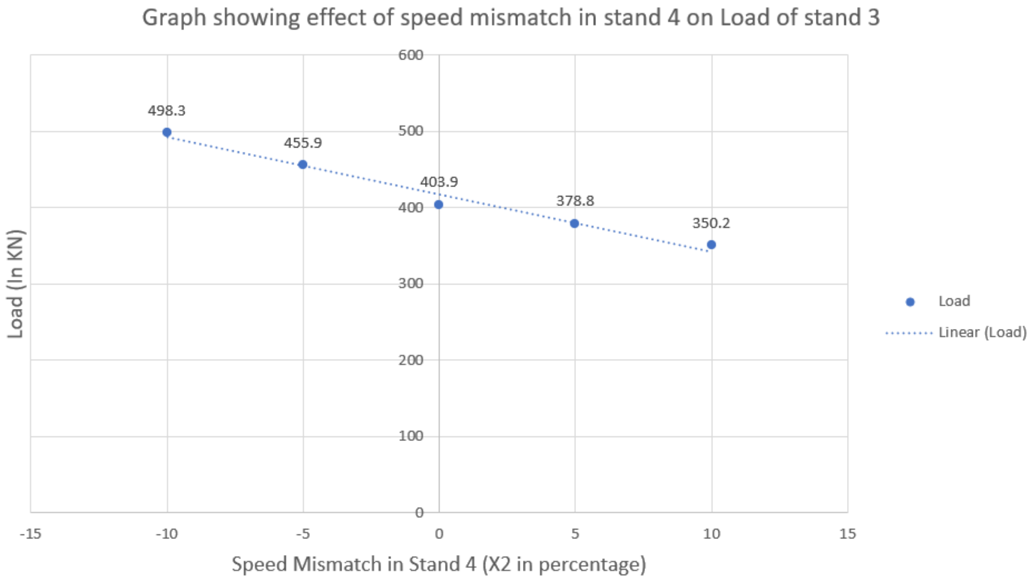

Figure 4-8: Load Graphs (By Author)

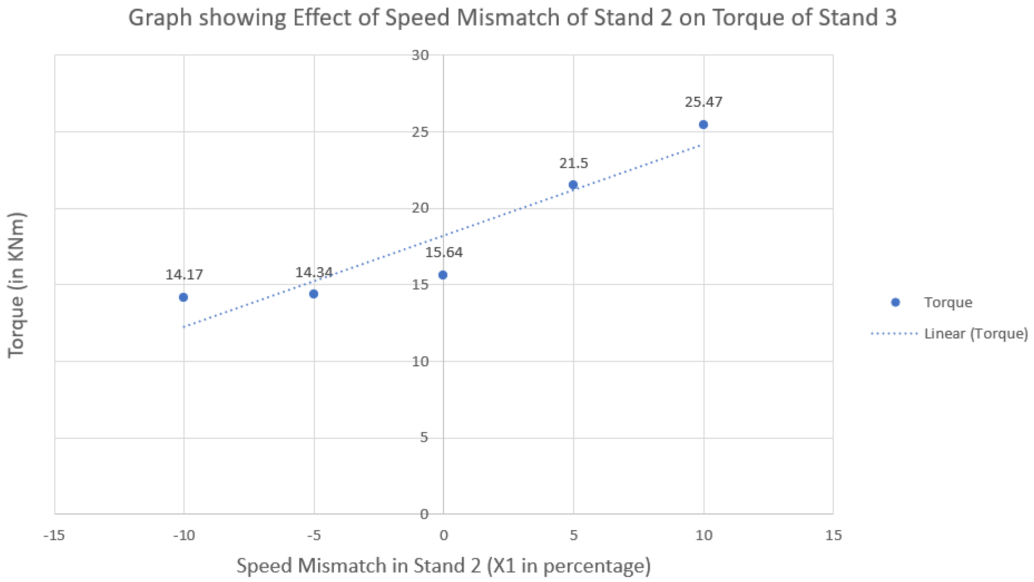

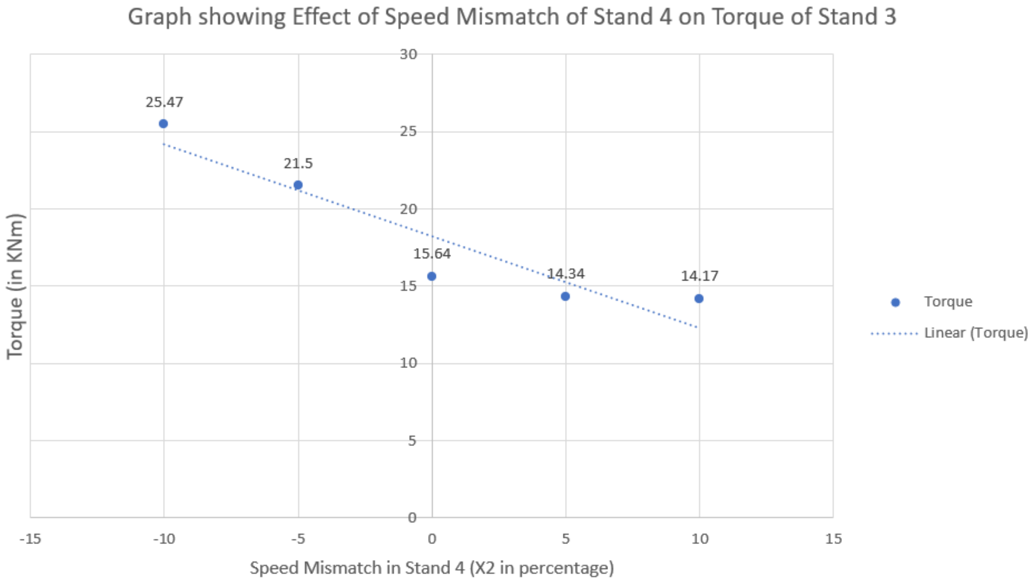

Figure 4-9: Torque Graphs (By Author)

4-3 Simulation Verification

A theoretical analysis to verify the results from the FEM-based simulator can be conducted using the equations presented in Section 3-3. The analysis takes into consideration different rolling modes. The analysis for rolling mode (-5,5) is shown below.

The speed mismatch is calculated using (3-25) as:-

$$\mathrm{X1} = \frac{20.4136 - 21.488}{21.488} \times 100 = -5\%$$
$$\mathrm{X2} = \frac{43.483 - 41.413}{41.413} \times 100 = 5\%$$

The external coefficient of friction is calculated using (3-21) as:-

$$\mathrm{f} = (1.05 - 0.0005 \times 1050) = 0.525$$

The bite angle for the rolling mill stand is calculated using (3-22) as:-

$$\alpha = 2 \arcsin \sqrt{\frac{0.1131 - 0.0713}{2 \times 2 \times 0.196421}} = 0.4655 \,\text{radians}$$

The deformation ratio for the three stands are calculated using (3-23) as:-

$$\lambda_2 = 1.382;$$
$$\lambda_3 = 1.356;$$
$$\lambda_4 = 1.333$$

For calculating the lead of metal for the three stands, (3-24) is used and we as follows:-

$$\mathrm{S}_2 = \frac{0.528398 - 0.48063}{0.48063} = 0.099$$
$$\mathrm{S}_3 = \frac{0.740585 - 0.66337}{0.66337} = 0.1163$$
$$\mathrm{S}_4 = \frac{0.989802 - 0.946004}{0.946004} = 0.046$$

The front and the rear tension for the middle stand can be calculated using (3-26) as:-

$$\sigma_0 = \frac{1}{0.045}\left[\left(\frac{32.2507}{20.4136}\right) - \left(\frac{32.2507}{21.488}\right)\right]\left[\frac{0.196421}{0.224836} \cdot \frac{1}{1.356} \cdot \frac{1+0.116}{1+0.099}\right] = 1.15791 \,\mathrm{MPa}$$
$$\sigma_1 = \frac{1}{0.045}\left[\left(\frac{43.483}{32.25707}\right) - \left(\frac{41.413}{32.2507}\right)\right]\left[\frac{0.207552}{0.196421} \cdot \frac{1}{1.333} \cdot \frac{1+0.04}{1+0.116}\right] = 1.05365 \,\mathrm{MPa}$$

Equation (3-27) is used for finding out the resultant tension on the stand under consideration:-

$$\sigma_\Sigma = \sigma_0 - \sigma_1 = 0.10425 \,\mathrm{MPa}$$

The length of the deformation zone of the stand follows from (3-31) as:-

$$\mathrm{l_c} = \sqrt{(0.1131 - 0.0713) \times 0.196421} = 0.091 \,\mathrm{m}$$

The projection of the area of contact between the work roll and the workpiece follows from (3-30) as:-

$$\mathrm{F_k} = \frac{0.0637891 + 0.07540}{2} \times 0.091 = 0.0062\mathrm{m}^2$$

The term η is calculated using (3-33) as:-

$$\frac{1}{\eta} = \frac{0.1131}{0.0713} = 1.586$$

The change in the rolling moment of the stand under the influence of inter-stand tension follows from (3-29) as:-

$$\Delta \mathrm{M} = \frac{0.00626 \times 0.091}{1.586 - 1} \times 0.10425 = 0.101343\,\mathrm{KNm}$$

The entire back and front tension in the workpiece is calculated by using (3-28) as:-

$$\mathrm{T}_0 = 1.15791 \times 0.618403 = 0.716055\,\mathrm{MN}$$
$$\mathrm{T}_1 = 1.05365 \times 0.4396 = 0.46318\,\mathrm{MN}$$

The deformation in the workpiece follows from (3-20) as:-

$$\delta = \frac{2 \times 0525}{0.4655} = 2.255$$

With the use of (3-32), the change in roll pressure on the workpiece in the presence of inter-stand tension is given as:-

$$\Delta \mathrm{p} = -\left\{\left[\left(1.586 - 1.586^{0.27827}\right) \cdot \frac{1.15791}{0.586}\right] - \left[\left(1.586^{0.27827} - 1\right) \cdot \frac{1.05365}{0.586}\right]\right\} = -0.823658\mathrm{MPa}$$

With the use of (3-34), the torque on the stand can be calculated as follows:-

$$\mathrm{M_H} = 0.196421 \cdot \left(\frac{0.716055}{1.356} - 0.46318\right) \cdot (1 + 0.116) = 14.226\,\mathrm{KNm}$$

Similarly, the analysis for different modes is conducted in Appendix B. The results are shown below in Table 4-9.

Table 4-9: Comparison of theoretical results and simulation results

Rolling Mode (X1, X2)	$\mathrm{M_{HSimulations}}$ **(KNm)**	$\mathrm{M_{HAnalysis}}$ **(KNm)**
(-5,5)	14.34	14.226
(-10,10)	28.38	31.25
(5,-5)	21.5	13.05
(10,-10)	35.4	41.2

On average, 11% error in the results obtained through the FEM-based simulations. Given the limited factors considered in the FEM simulations, the disturbance model based on the regression analysis described in Chapter 6 can be termed a good approximation for the behaviour of the rolling mill under the influence of speed mismatches.

Chapter 5 provides a theoretical background of the controllers implemented to demonstrate the use of the disturbance model generated through the regression analysis. The designing of the controllers in the upcoming chapter along with the results presented in Chapter 6 answer the second research question of the master thesis.

Chapter 5

Controller Implementation

The chapter implements control philosophies using the disturbance model obtained in the simulations conducted in the thesis for the roughing mill section of the rolling mill at the use-case facility. The chapter will first present the current PID controller and its performance at the use-case facility. The author manually tunes the PID to ensure that the performance improves by eliminating the steady-state error. Post this, the chapter presents the design and tuning of the Linear Quadratic Regulator (LQR) and Model Predictive Control (MPC) controllers used for the implementation of speed control. These controllers are model-based and should have a performance enhancement compared to the PID controllers. The simulation results of these speed controllers are discussed in depth in Chapter 6.

Figure 5-1 shows the PID controller used at the use-case facility. The current control strategy does not have the disturbance model generated in the thesis. Therefore, the strategy only takes into account the speed of stand 3. The disturbance introduced to the system below is similar to the one corresponding to the rolling mode (-5,5). The simulation depicts a case where multiple workpieces pass through the rolling mill every 10 seconds. The results are shown in Figure 5-2. It can be noted from the results that even though the settling time of the controller is fast (around 1.4 seconds), there is a steady-state error that exists and keeps increasing as consecutive workpieces pass through the rolling mill. In a scenario like this, the mill operators must keep adjusting the speed of the stand 3 to ensure that the quality of the end wire rod is maintained. Also, there is a significant increase in the speed of the stand when the workpiece enters the stand. This is highly undesirable as it adversely impacts the quality of the final wire rod obtained at the end of the line.

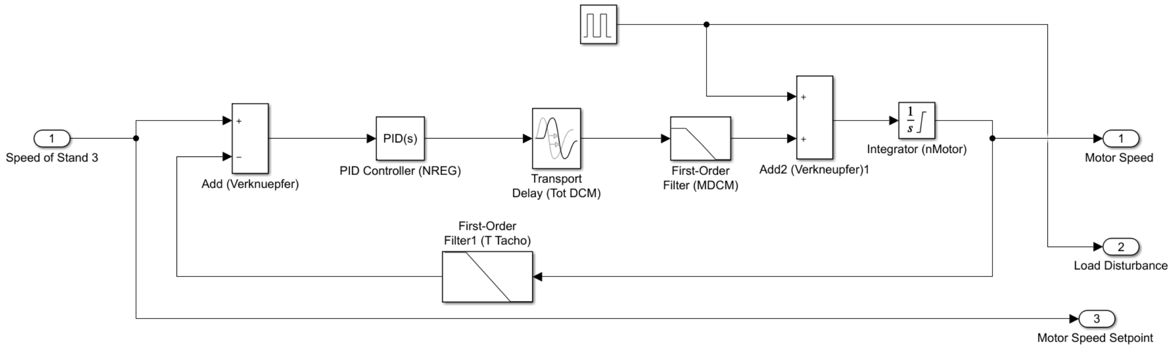

Figure 5-1: Control Philosophy at ArcelorMittal Hamburg (By Author)

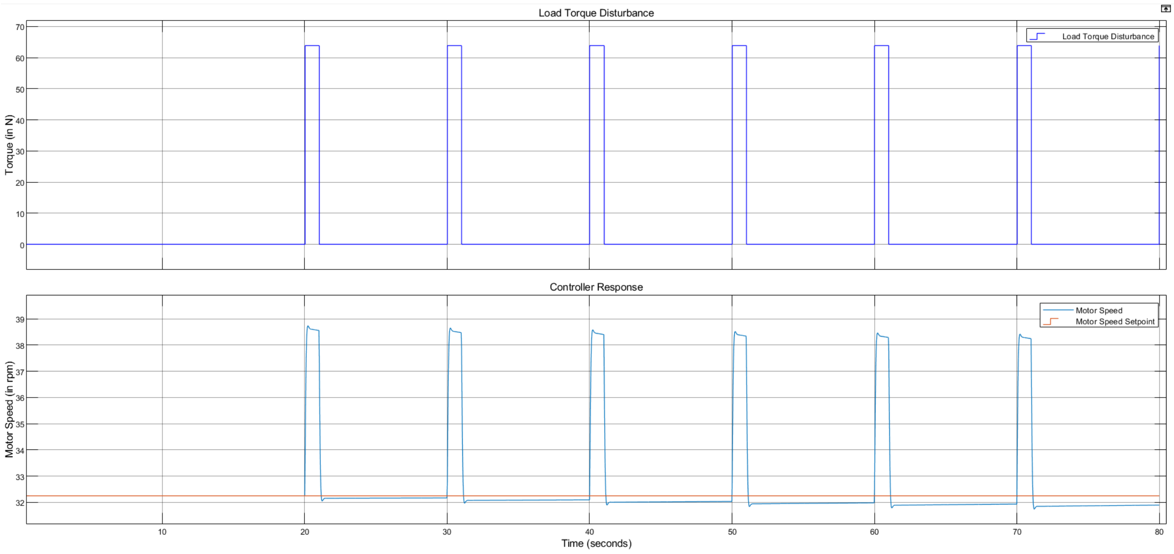

Figure 5-2: Results of PID controller at ArcelorMittal Hamburg (By Author)

5-1 PID Controller

The PID-based control is the first option in the choice of the controllers. The choice is based the PID controller's use in more than 90 % of the industrial processes. The control strategy's popularity is because there is a vast range of techniques for tuning, both in the time and frequency domain. It is intuitive to use when manual tuning needs to be performed, for which guidelines exist, as in [28].

As provided by the use-case facility, the transfer function we have for the rolling mill is shown below in (5-1). It resembles a system category of a third-order system with zeros and time delay. The use-case facility uses a generalised transfer function to represent the rolling mill. The transfer function is an approximated function that captures the rolling mill's behavior irrespective of the metallurgical material or temperature of the workpiece. The transfer function is defined around the operating point of the rolling mill stand under consideration. The transfer function stated below has been used at the facility for the past 10 years and was developed with the help of the technological partners of the use-case facility.

$$\mathrm{H}(s) = \frac{32.2507\mathrm{e}^{-0.02s}\,(1 + 0.014s)}{0.00014s^3 + 0.024s^2 + s + 32.2507\mathrm{e}^{-0.02s}} \tag{5-1}$$

Since the transfer function finds use in the current rolling mill, it will be used for the analysis presented in this thesis work.

5-1-1 PID Tuning

The PID controller in the context of this thesis work was used in the parallel form with manual tuning, which is in line with the current use status at the use-case facility. A step-by-step approach for the PID controller's manual tuning. The PID controller must be turned on and placed correctly in the system for the approach. The first step is to initialise all the gains of the zero. The proportional gain must be increased until oscillations are observed in the output, as shown in Figure 5-3. Once oscillations are observed, the P gain can be set to approximately half this value. Now, the system exhibits a significantly high overshoot.

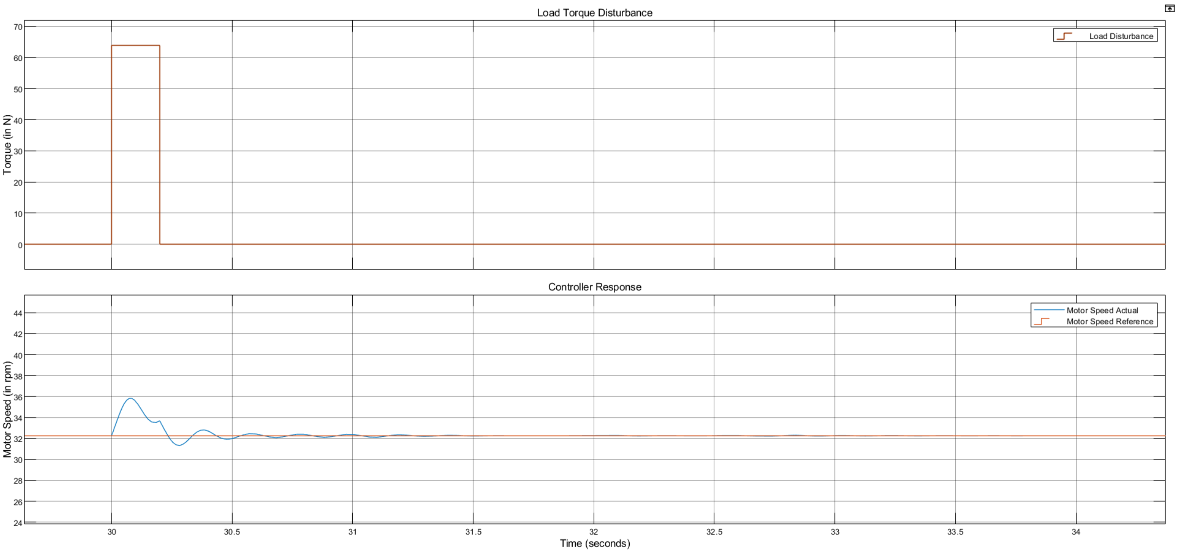

Figure 5-3: Tuning P gain of PID controller. P = 33 (By Author)

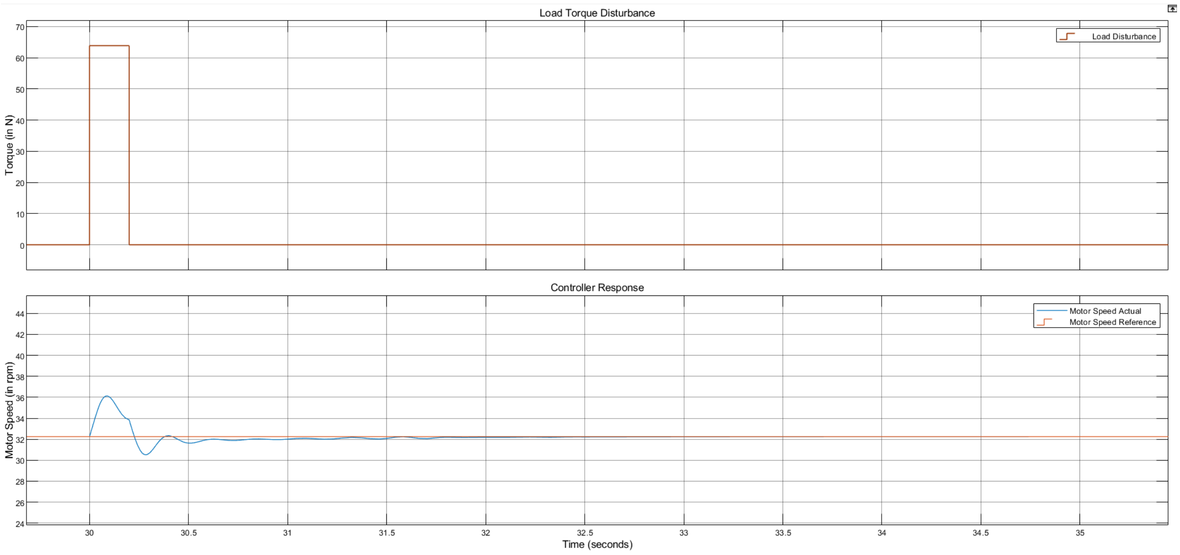

Figure 5-4: Tuning I gain of PID controller. I = 26 (By Author)

The integral gain should now be increased to ensure that the steady-state error can be minimised. The increase in I-gain increases the system's settling time, as shown in Figure 5-4. It should also be kept in mind not to increase the I-gain so that the overshoots become very high and cause instability of the system and damage to the system components. Once the I gain is set, the derivative gain can be tuned.

The D-gain should be set so that the settling time and the rise time of the response can be reduced, as shown in Figure 5-5. The response has some noise. The D-gain has to be used along with a high filter coefficient to reduce the noise.

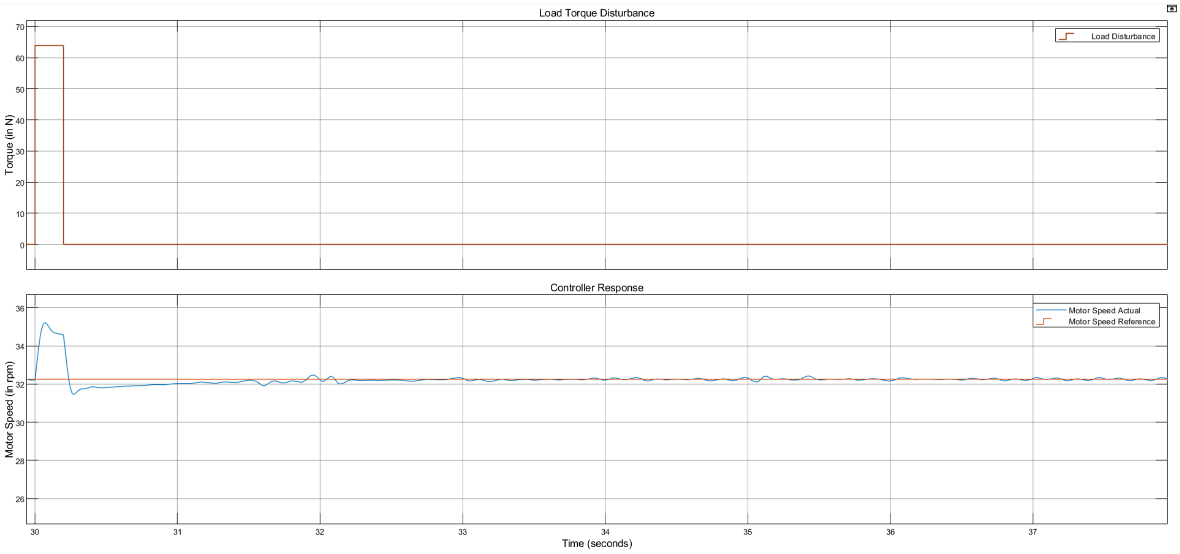

Figure 5-5: Tuning D gain of PID controller. D = 0.5 (By Author)

The final tuned values of the PID controller are shown below in Table 5-1.

Table 5-1: Controller Parameters for PID Controller

Parameter	**Value**
P - Gain	24
I - Gain	26
D - Gain	0.496
Filter Coefficient(N)	3537

5-2 Linear Quadratic Regulator (LQR) Controller

LQR is a type of modern state variable feedback system and part of the optimal controllers family. It follows the idea of the pole placement controller. The pole placement controller is a relatively straightforward controller philosophy. However, it becomes extremely cumbersome to implement in a case where the number of states of the system is significant. The pole placement controller also does not consider the controller's effort during closed-loop operation.

An index-based optimisation technique was developed to minimize a cost function to overcome such problems. The controllers designed on this philosophy are called optimal state feedback controllers.

Consider the performance index of a single-input, single-output system to be defined as follows:-

$$\mathrm{J} = \frac{1}{2}\int_0^\infty \left[\mathrm{x}^T\mathrm{Q}\mathrm{x} + \mathrm{R}u^2\right] dt \tag{5-2}$$

with the state equation of the system as:-

$$\dot{x} = \mathrm{A}\mathrm{x} + \mathrm{B}u \tag{5-3}$$

The output of the controller is defined as:-

$$u = \mathrm{F}\mathrm{x} = \begin{bmatrix} f_1 & f_2 & \dots & f_n \end{bmatrix} \mathrm{x} \tag{5-4}$$

The performance index shown in (5-2) gets minimised when

$$\mathrm{F} = -\mathrm{R}^{-1}\mathrm{B}^T\mathrm{P} \tag{5-5}$$

where P is a positive definite matrix and is the solution of the nonlinear, steady-state continuous-time Riccati equation defined as:-

$$\mathrm{A}^T\mathrm{P} + \mathrm{P}\mathrm{A} - \mathrm{P}\mathrm{B}\mathrm{R}^{-1}\mathrm{B}^T\mathrm{P} + \mathrm{Q} = 0 \tag{5-6}$$

The LQR derived as presented above has a control law given by:- [9]

$$u = -\mathrm{R}^{-1}\mathrm{B}\mathrm{P}\mathrm{x} \tag{5-7}$$

This type of controller is used in the thesis to compare a modern control technique and the traditional PID controller.

To implement the LQR, a state-space representation for the system needs to be created. We will be designing the LQR controller in the discrete-time domain.

5-2-1 State Space Representations

The continuous-time and discrete-time state-space representations are generated using MATLAB, as shown in Appendix (D-1). We get a state-space representation of the system in continuous time, as shown in (5-8).

$$\begin{aligned} \begin{bmatrix} \dot{\mathrm{x}_1} \\ \dot{\mathrm{x}_2} \\ \dot{\mathrm{x}_3} \end{bmatrix} &= \begin{bmatrix} -100 & 0 & -571.4286 \\ 1 & 0 & 0 \\ 0 & 403.1338 & -71.4286 \end{bmatrix} \begin{bmatrix} \mathrm{x}_1 \\ \mathrm{x}_2 \\ \mathrm{x}_3 \end{bmatrix} + \begin{bmatrix} 64 \\ 0 \\ 0 \end{bmatrix} \begin{bmatrix} u \end{bmatrix} \\ \mathrm{y} &= \begin{bmatrix} 0 & 50.3917 & 0 \end{bmatrix} \begin{bmatrix} \mathrm{x}_1 \\ \mathrm{x}_2 \\ \mathrm{x}_3 \end{bmatrix} \end{aligned} \tag{5-8}$$

From (5-8), we have the following:-

$$\begin{aligned} \mathrm{A} &= \begin{bmatrix} -100 & 0 & -571.4286 \\ 1 & 0 & 0 \\ 0 & 403.1338 & -71.4286 \end{bmatrix} \\ \mathrm{B} &= \begin{bmatrix} 64 \\ 0 \\ 0 \end{bmatrix} \\ \mathrm{C} &= \begin{bmatrix} 0 & 50.3917 & 0 \end{bmatrix} \\ \mathrm{D} &= [0] \end{aligned}$$

An appropriate sampling time is selected to convert the continuous-time state-space to the discrete-time state-space. The step response of the discrete-time system was compared with that of the continuous-time system to arrive a the suitable value of the sampling time of 0.001. Figure 5-6 shows the step response of the continuous-time and discrete-time systems with a sampling time of 0.001.

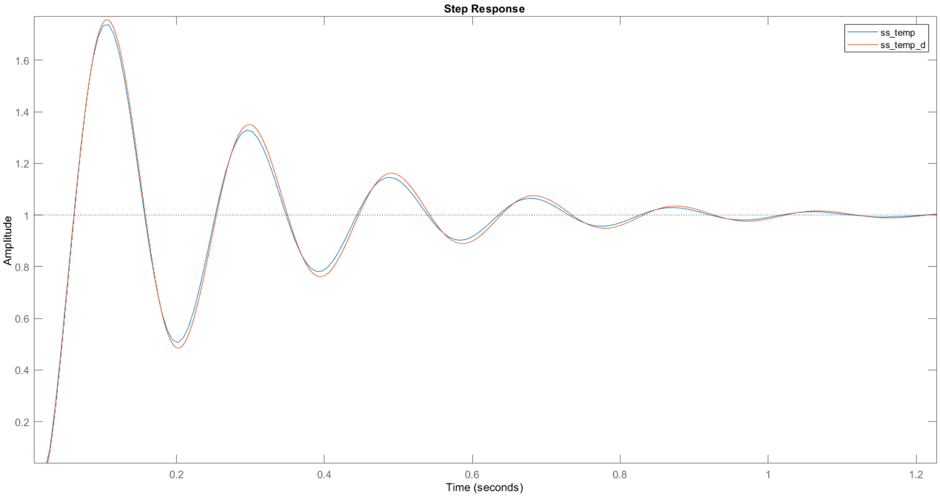

Figure 5-6: Step Response of Continuous time and Discrete time system with Sampling time of 0.001 (By Author)

After selecting the sampling time as 0.001, the discrete-time state-space representation is shown in (5-9) [29].

$$
\begin{aligned}
\begin{bmatrix} \mathrm{x}_1(k+1) \\ \mathrm{x}_2(k+1) \\ \mathrm{x}_3(k+1) \end{bmatrix} &= \begin{bmatrix} 0.904837 & 0 & -0.543786 \\ 0.000951 & 1 & -0.000276 \\ 0.000190 & 0.389072 & 0.9310259 \end{bmatrix} \begin{bmatrix} \mathrm{x}_1(k) \\ \mathrm{x}_2(k) \\ \mathrm{x}_3(k) \end{bmatrix} + \begin{bmatrix} 0.0609 \\ 0.0000309 \\ 0.00000412 \end{bmatrix} \begin{bmatrix} u(k) \end{bmatrix} \\
\mathrm{y}(k) &= \begin{bmatrix} 0 & 50.3917 & 0 \end{bmatrix} \begin{bmatrix} \mathrm{x}_1(k) \\ \mathrm{x}_2(k) \\ \mathrm{x}_3(k) \end{bmatrix}
\end{aligned}
\tag{5-9}
$$

From (5-9), we get the following:-

$$
\begin{aligned}
\Phi &= \begin{bmatrix} 0.904837 & 0 & -0.543786 \\ 0.000951 & 1 & -0.000276 \\ 0.000190 & 0.389072 & 0.9310259 \end{bmatrix} \\
\Gamma &= \begin{bmatrix} 0.0609 \\ 0.0000309 \\ 0.00000412 \end{bmatrix} \\
\mathrm{C} &= \begin{bmatrix} 0 & 50.3917 & 0 \end{bmatrix} \\
\mathrm{D} &= [0]
\end{aligned}
$$

5-2-2 Linear Quadratic Regulator (LQR) Controller Design

An external load disturbance that acts on the system. To accommodate this disturbance, reject it, and ensure that the system can track our input, the design of the LQR needs to be modified as shown in Figure 5-7, where v is the load disturbance acting on the system of form $v(\mathrm{k}+1) = v(\mathrm{k})$, $\hat{v}$ is the estimated disturbance from the Disturbance Observer which is an Integrator, $\hat{x}$ is the estimated states of the system of the State Observer, ϵ is the error dynamics of the observer and is given by $y(\mathrm{k}) = \mathrm{C}\hat{x}(\mathrm{k})$ [8].

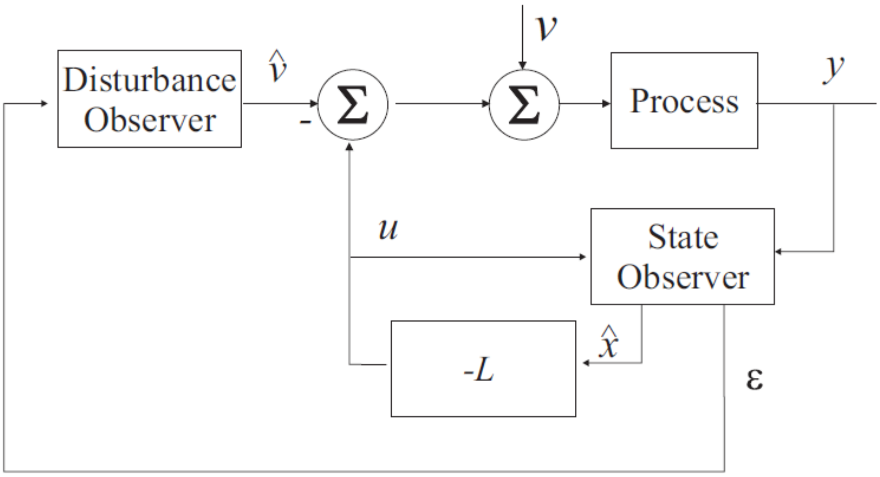

Figure 5-7: Modified LQR design for disturbance rejection [8]

State Observer Design

A state observer is designed in a scenario where the states of the system are not directly available for measurement and have to be estimated instead. The observer is a copy of the original system and is mathematically described as shown in (5-10) and Figure 5-8. The observer poles are selected so that the observer under design shows an asymptotic behaviour, as shown in Figure 5-9. The MATLAB code for the observer design is shown in Appendix D-2.

$$\begin{aligned}\hat{x}(k+1) &= \Phi\hat{x}(k) + L[y(k) - \hat{y}(k)] + \Gamma u(k)\\ \hat{y}(k) &= C\hat{x}(k) + Du(k)\end{aligned} \tag{5-10}$$

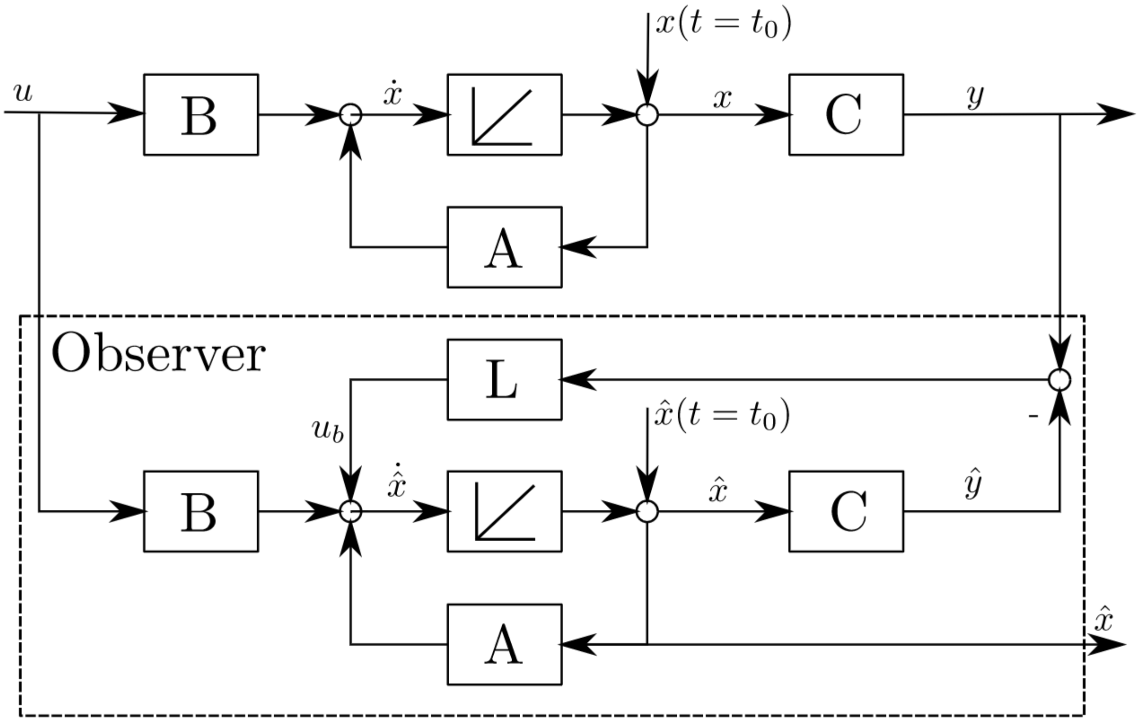

Figure 5-8: State Observer for continuous time system [9]

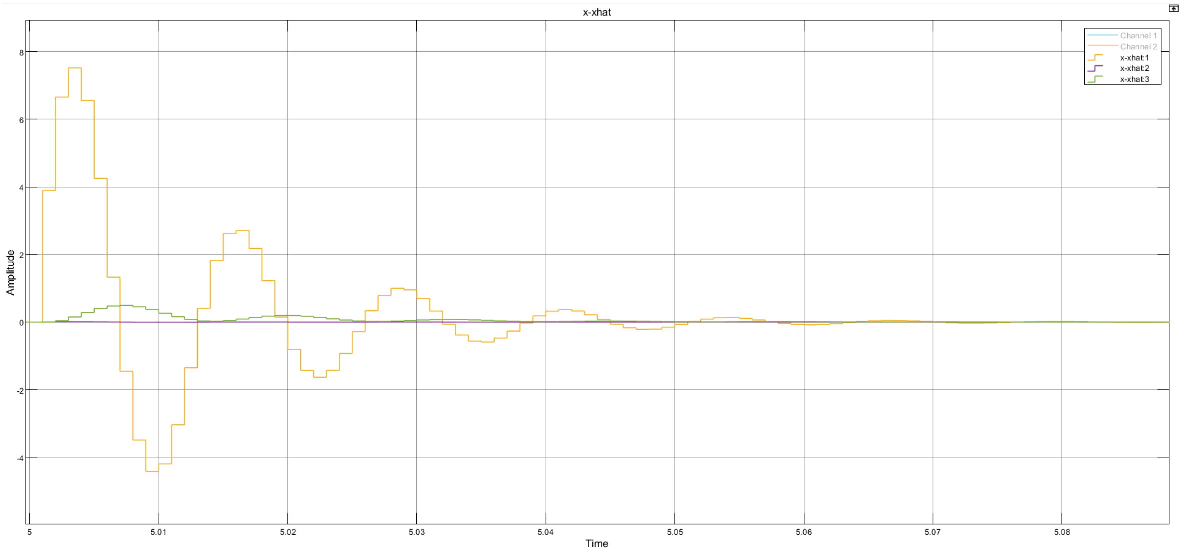

Figure 5-9: Asymptotic behaviour of state observer (By Author)

Disturbance Observer Design

The disturbance observer is a discrete-time integrator. The gain of the integrator needs to be adjusted to ensure that the observer has an asymptotic behaviour as well. While ensuring that the time required for the observer to estimate the disturbance is small, one has to be careful not to have very high transients. A very high transient would lead to significant errors in the tracking performance of the controller. The dynamics of the disturbance observer are shown in Figure 5-10, and the MATLAB code for it is shown in Appendix D-2.

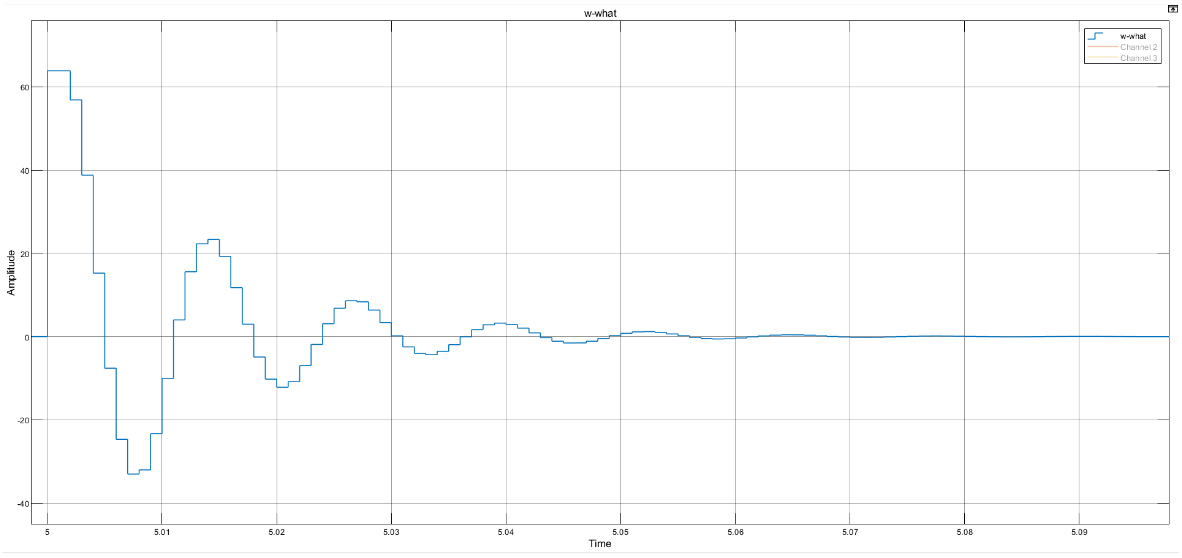

Figure 5-10: Asymptotic behaviour of disturbance observer (By Author)

State Feedback Gain Design

The state feedback gain is selected using the LQR controller philosophy. For tuning the response of the state feedback gain, we have to tune two parameters, namely Q and R. Irrespective of the values of Q and R, the cost function, shown in (5-2) has a unique minimum which is obtained by solving the Riccati equation shown in (5-6). The parameters Q and R penalise the state variables and control signals, respectively. The larger one selects the values for these parameters, the more one penalises the signals. A high value of parameter R as compared to the Q-value depicts a case where one tries to stabilise the system with less energy. The focus is to stabilise the system with the least possible control input. This type of controller is considered to be a conservative controller. Compared to the R-value, a large Q parameter value depicts a case where we do not care about the input required to bring the states to the desired value. In other words, it means the focus is more on converging the states of the system to a stable point rather than the control input to the system leading to creating an aggressive controller. These two parameters must be appropriately tuned to ensure a decent performance of the controller.

Table 5-2: Tuning Q and R parameters for LQR

Q	R	Overshoot (rpm)	Steady State Error (rpm)	Settling Time (sec)	Figure
I	1	36.48	0.15	0.209	5-11
	10	36.85	0.02	0.346	5-12
	100	36.9	0	0.325	5-13
	1000	36.9	0	0.328	5-14
10 * I	1	35.27	0.2	0.318	5-15
	10	36.48	0.2	0.273	5-16
	100	36.83	0.02	0.329	5-17
	1000	36.9	0	0.408	5-18

For tuning the LQR, an iterative procedure is followed to determine the best possible configuration for the controller. First, the Q matrix is set to the Identity matrix to start with this iterative procedure. Then the R values are varied to see the performance of the resulting controller. To compare the combinations, the parameters of interest are the steady-state error, the maximum overshoot, and the settling time of the system's response to a step disturbance. Table 5-2 shows this comparison.

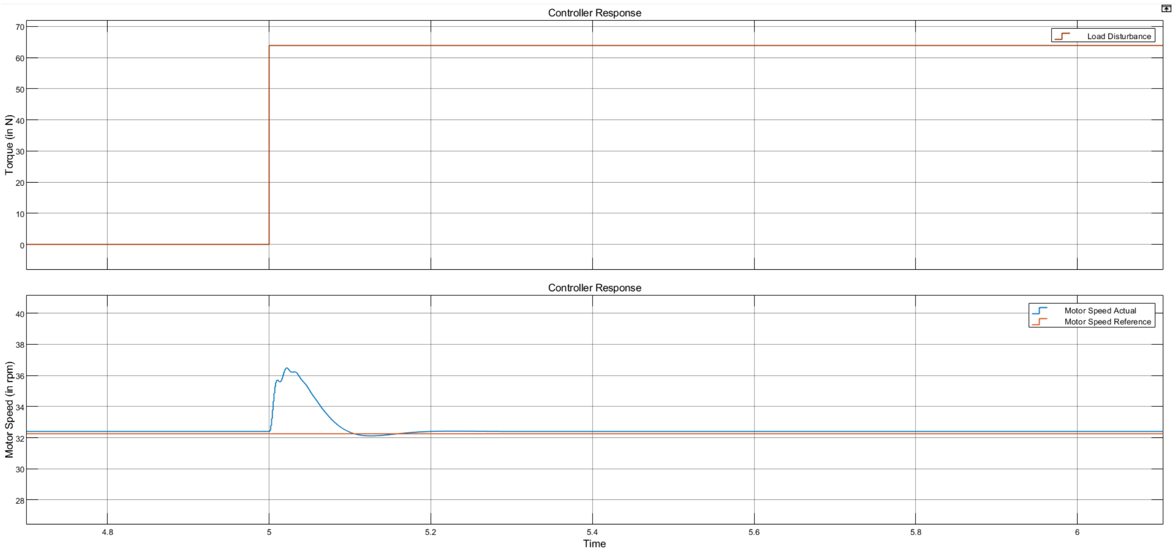

Figure 5-11: System Response for Q-Identity Matrix and R-value 1 (By Author)

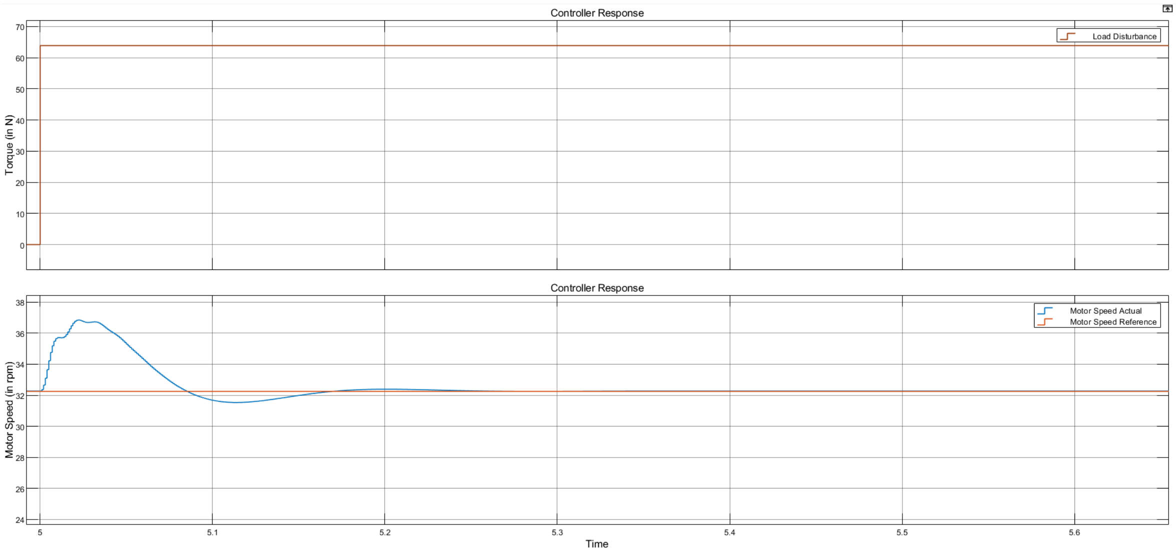

Figure 5-12: System Response for Q-Identity Matrix and R-value 10 (By Author)

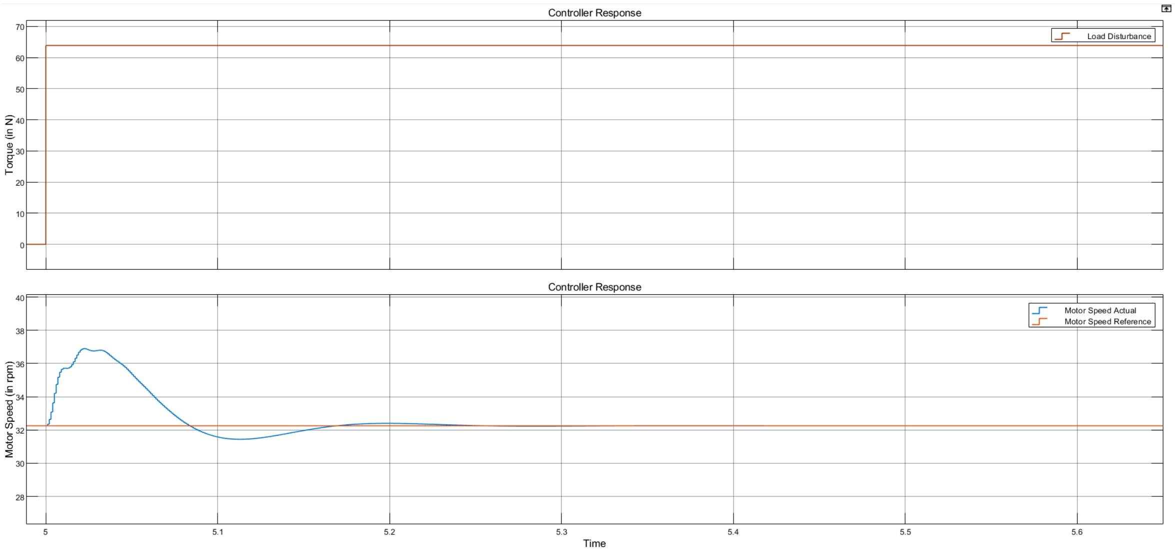

Figure 5-13: System Response for Q-Identity Matrix and R-value 100 (By Author)

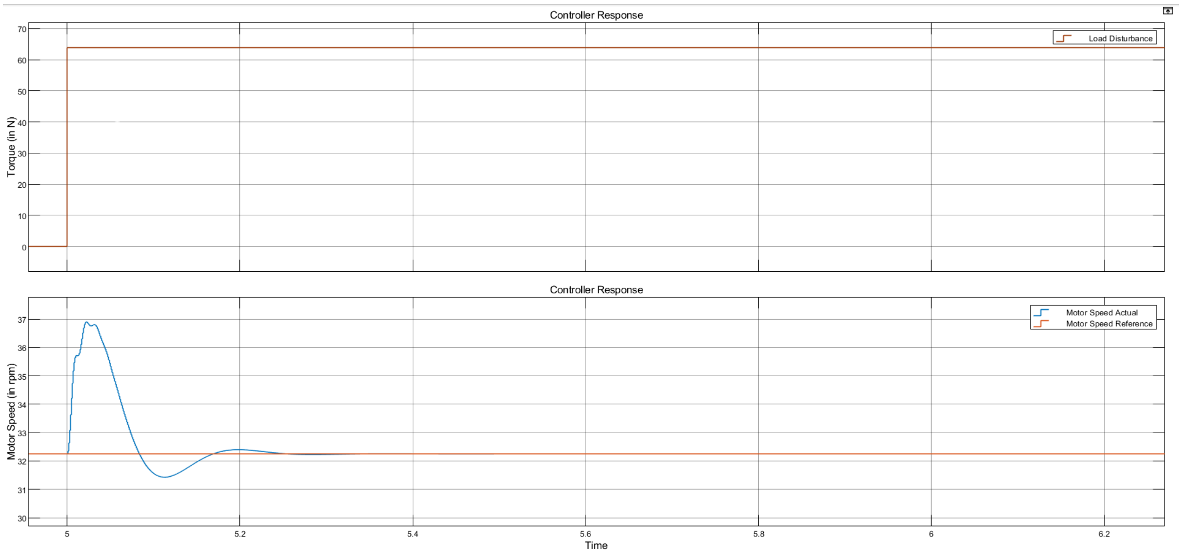

Figure 5-14: System Response for Q-Identity Matrix and R-value 1000 (By Author)

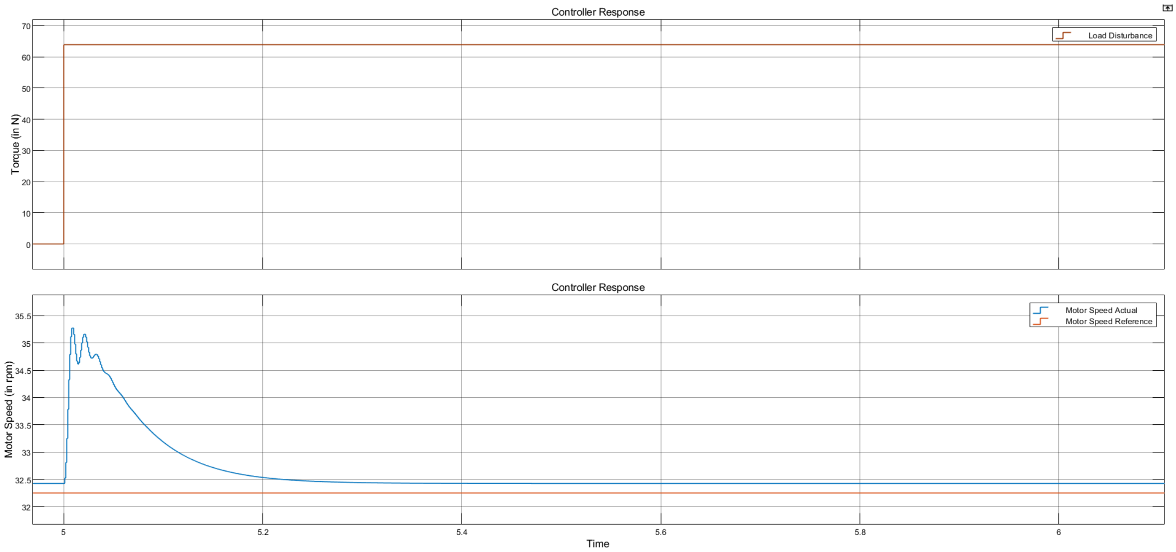

Figure 5-15: System Response for Q-10*Identity Matrix and R-value 1 (By Author)

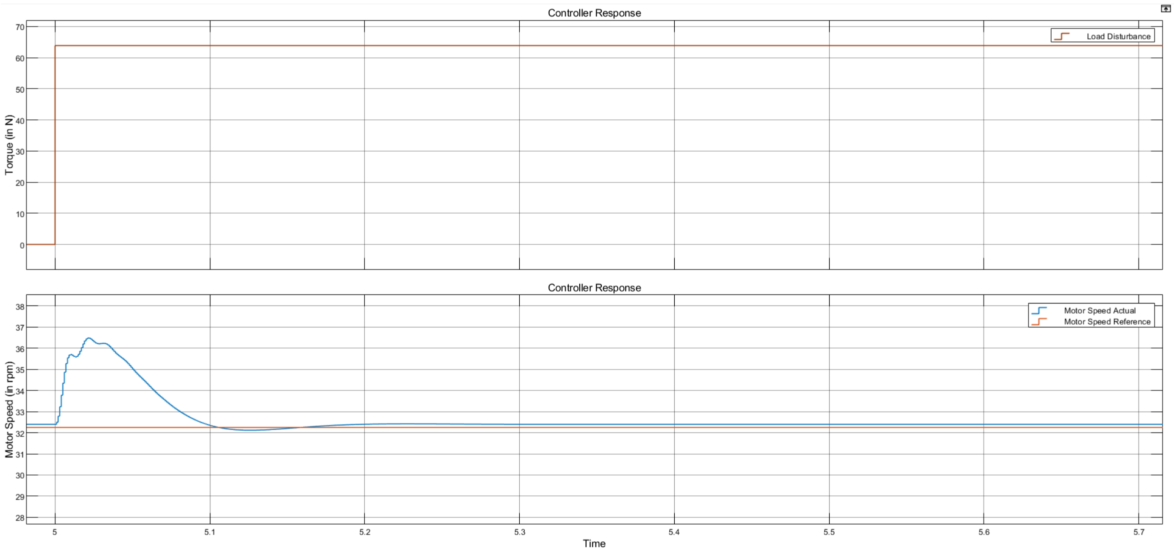

Figure 5-16: System Response for Q-10*Identity Matrix and R-value 10 (By Author)

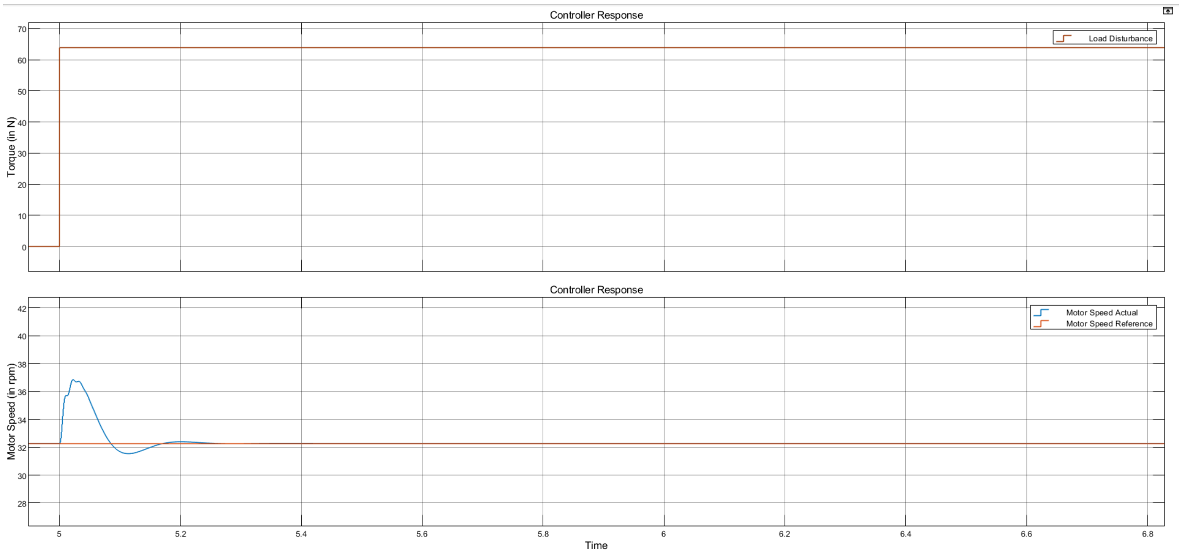

Figure 5-17: System Response for Q-10*Identity Matrix and R-value 100 (By Author)

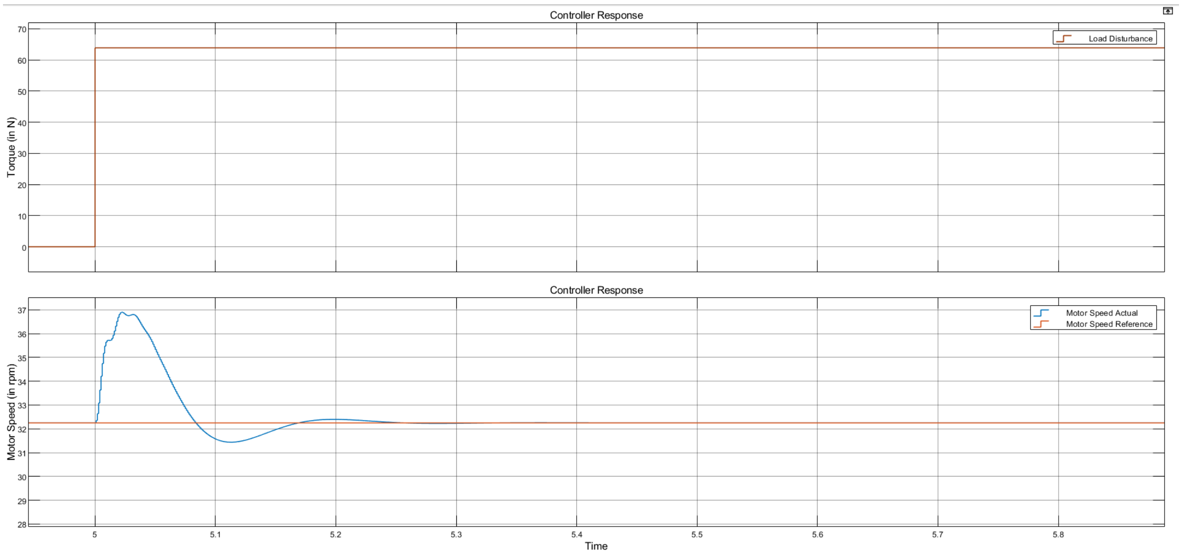

Figure 5-18: System Response for Q-10*Identity Matrix and R-value 1000 (By Author)

From Table 5-2, we choose the Q and R values as Identity Matrix and 100, respectively. This choice is based on our requirement of achieving zero steady-state error with the best possible settling time and the least overshoot. The MATLAB code for the LQR implementation is illustrated in Appendix D-2.

5-3 Model Predictive Control (MPC) Controller

MPC is a widely used feedback controller in applications where information regarding the system models is correctly available. It consists of two main parts, Model Prediction, and the Optimisation Algorithm. So essentially, the MPC considers a simplified system model, tries to predict the system's future output evolution, and finds the best possible control input for the system.

Figure 5-19 shows the working policy of the MPC. Here, k represents the current time. N represents the horizon for the optimisation problem. In a particular horizon, the controller predicts the evolution of the system's output and the control input. Therefore, in this particular optimisation window determined by the horizon value, the quadratic cost function of the system is optimised to find the best possible control input sequence for the system under consideration. This optimization procedure is repeated with the optimization window undergoing a time shift of N samples. This time shift is repeated for the entire simulation time of the problem, and a corresponding optimisation problem is solved to obtain the optimal control input sequence.

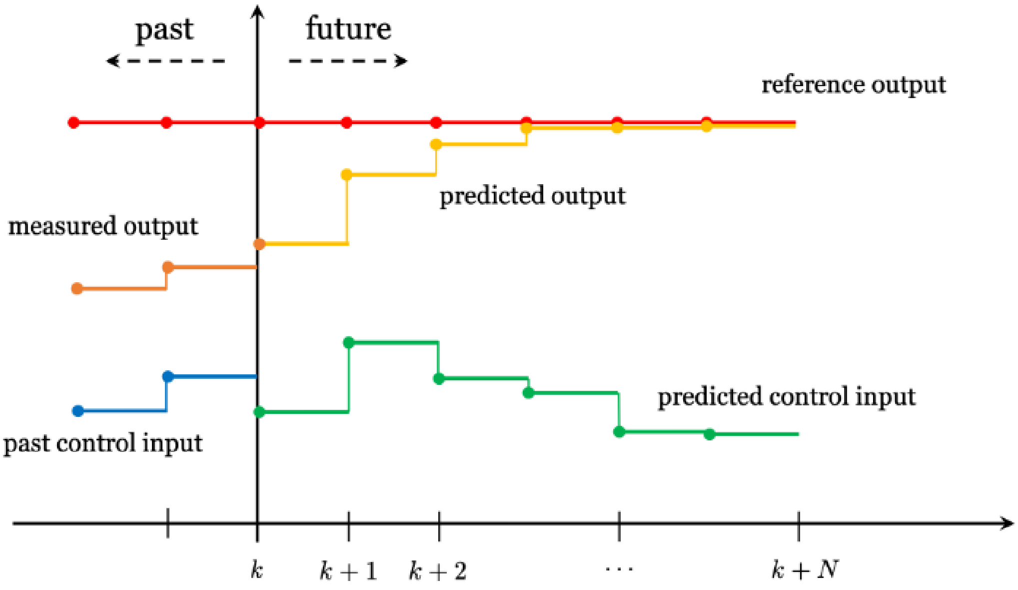

Figure 5-19: Horizon Policy for MPC [10]

Even though MPC and LQR are similar, both being feedback controllers based on solving a quadratic cost function, the working principle is different. The LQR solves the optimisation problem for an infinite horizon to ensure the system is stable. This does not guarantee system stability in a specific horizon. The MPC runs the optimisation problem in a loop where each optimisation problem is solved for a specific horizon length ensuring system stability throughout the horizon of the problem. Solving the optimisation problem in a loop is called the receding horizon policy.

5-3-1 Designing the Model Predictive Controller

The system model used for implementing the MPC is shown in (5-11). Here the disturbance, which is considered as either a step signal or a piece-wise signal, is considered an input to the system. The "MPC" block in Simulink is used to design the controller.

$$\begin{aligned} x(k+1) &= \Phi x(k) + \Gamma u(k) + \Gamma_d w(k) \\ y(k) &= Cx(k) + Du(k) \end{aligned} \tag{5-11}$$

In the Simulink block, the prediction and control horizons of the MPC can be adjusted to obtain the desired characteristics. The internal Kalman Filter of the block for state approximation. The prediction horizon, p, is the number of future control intervals the MPC controller needs to evaluate by prediction when optimizing the control sequence at interval k. The control horizon, m, is the number of control input sequences that have to be optimized at interval k. The control horizon varies between 1 and the prediction horizon p [30].

A systematic procedure is followed to obtain the desired values for both horizons. The default values in the toolbox for the prediction and control horizons are 10 and 2, respectively. First, the prediction horizon is changed, keeping the control horizon at 2. As the prediction horizon is increased from its default values, the step response of the MPC controller improves. A change in the control horizon does not have any effect on the performance of the system. Therefore the value of the control horizon is held constant at its default value. Figure 5-20 shows the step response of the MPC for its default values. Figures 5-21 and 5-22 show the step response of the MPC for a value of 20 and 30 for the prediction horizon. Figure 5-23 shows the step response of the MPC controller for a change in the control horizon. The code for the MPC controllers shown below in the figures is illustrated in Appendix D-3.

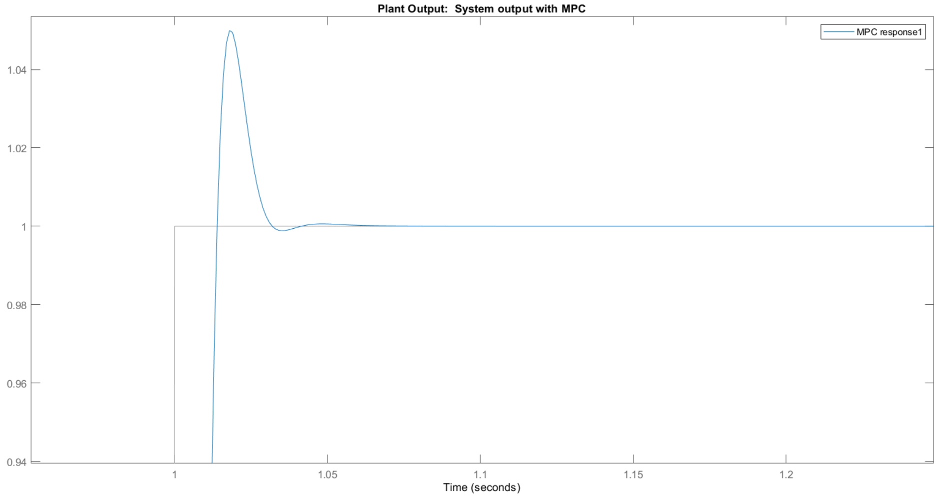

Figure 5-20: Step Response MPC with $p = 10$ and $m = 2$ (By Author)

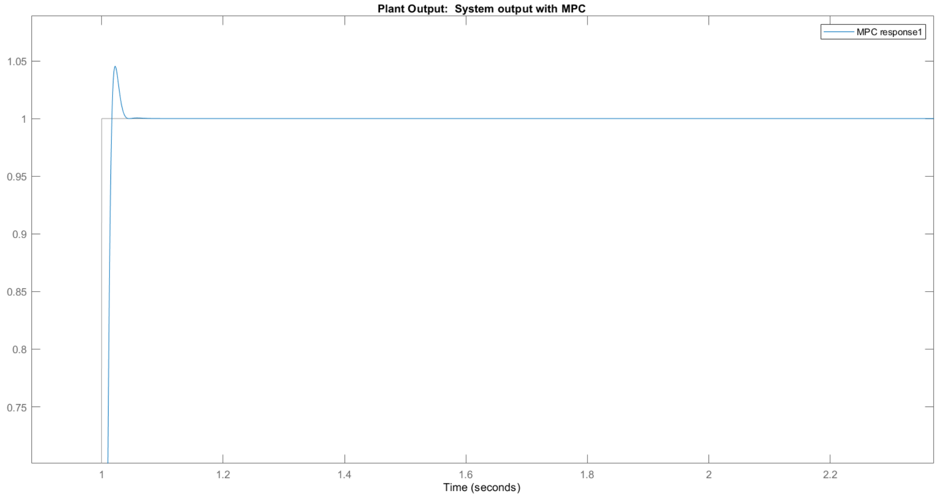

Figure 5-21: Step Response MPC with $p = 20$ and $m = 2$ (By Author)

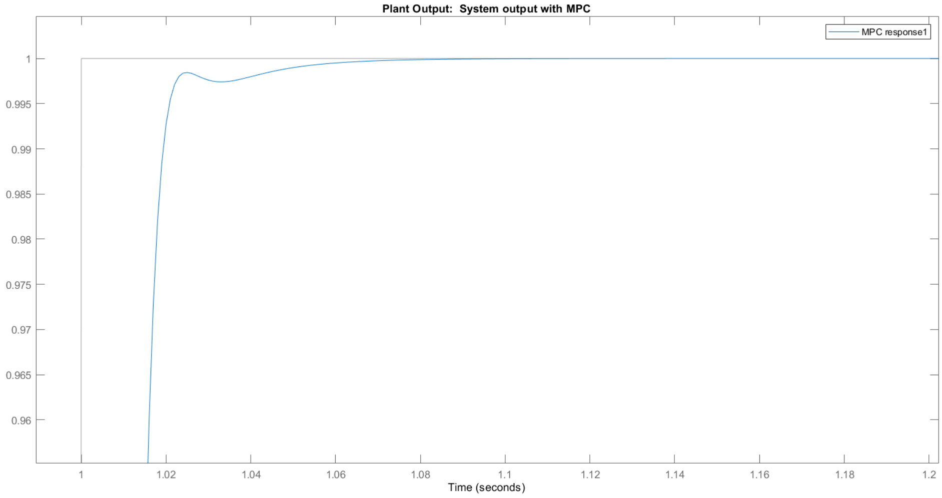

Figure 5-22: Step Response MPC with $p = 30$ and $m = 2$ (By Author)

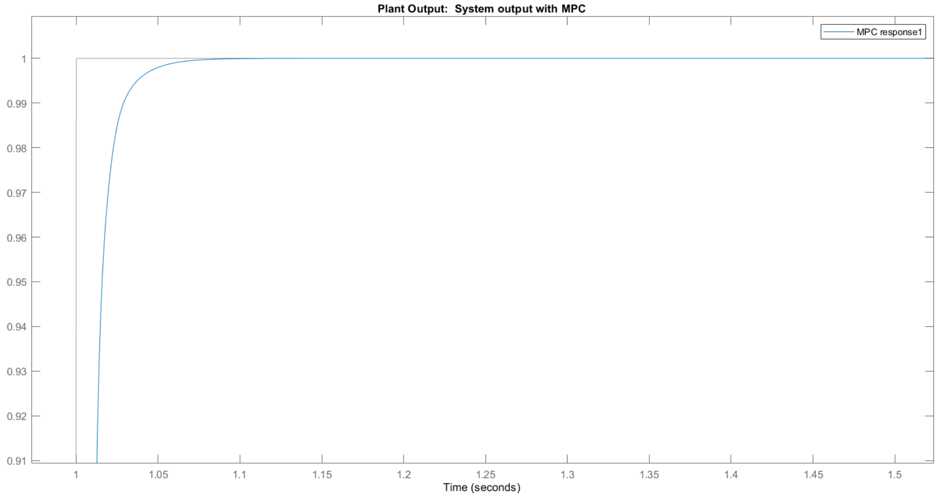

Figure 5-23: Step Response MPC with $p = 30$ and $m = 3$ (By Author)

The prediction and control horizon values selected for implementing the MPC controller are 30 and 2, respectively.

After designing the controllers in this chapter, Chapter **??** presents the simulations of the designed controllers for the speed control problem and, therefore, answers the second research question of the master thesis.

Chapter 6

Results And Discussion

The chapter will present the results obtained during the thesis. A detailed discussion explaining the results will be presented in this chapter. The first section will present the results of the regression analysis. It will also present the quantitative model obtained for the technological parameters due to speed mismatch to conclude the first research question of the master thesis.

The quantitative model will lead to the creating a load disturbance model in Simulink to reflect the speed mismatch disturbance in the current control scheme in use at the use-case facility. The second part of the chapter discusses the results obtained while implementing the speed controllers described in Chapter 5, along with the disturbance model. This would conclude the second research question of this master thesis.

6-1 Regression Analysis

A regression analysis has been carried out to obtain a quantitative model for the effect of speed mismatch on the technological parameters of rolling for stand 3. The results are obtained in Table 4-8. As shown in (6-1), a linear dependency model is used to undertake the regression analysis, where Y is the required parameter (Load L, Torque M, and Power P), a_0, a_1, and a_2 are the regression coefficients. The "fitnlm" function of MATLAB was used for the analysis. The results obtained from the regression analysis are shown in Table 6-1. Figures 6-1, 6-2, and 6-3 show the results plotted in MATLAB for the regression results.

$$\mathrm{Y} = \mathrm{a}_0 + \mathrm{a}_1 * \mathrm{X1} + \mathrm{a}_2 * \mathrm{X2} \tag{6-1}$$

Table 6-1: Regression Results

Technological Parameter (Y)	**Parameters**		
	a_0	a_1	a_2
Torque	18.479	-0.46905	-1.0244
Power	61.893	-1.6689	-3.5269
Load	418.29	1.6628	-6.1099

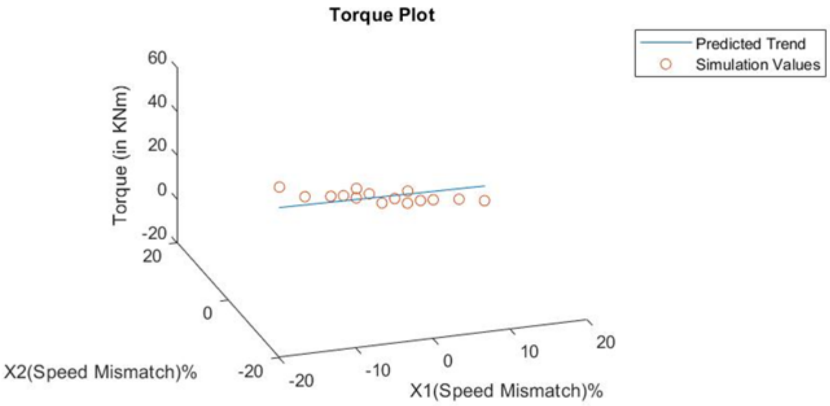

Figure 6-1: Regression Results for Torque (By Author)

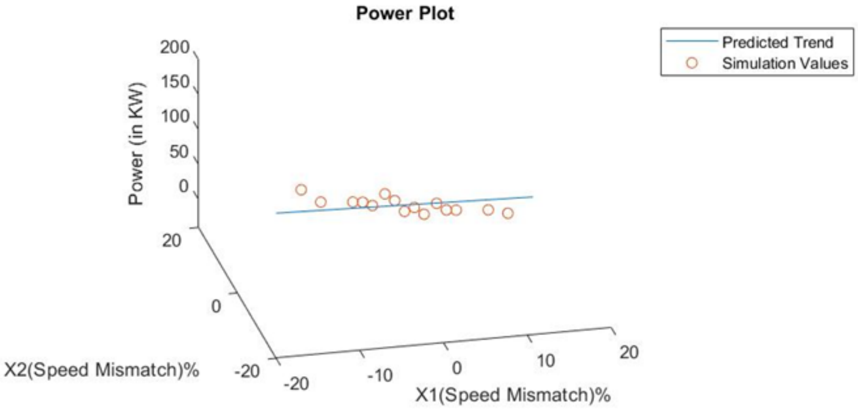

Figure 6-2: Regression Results for Power (By Author)

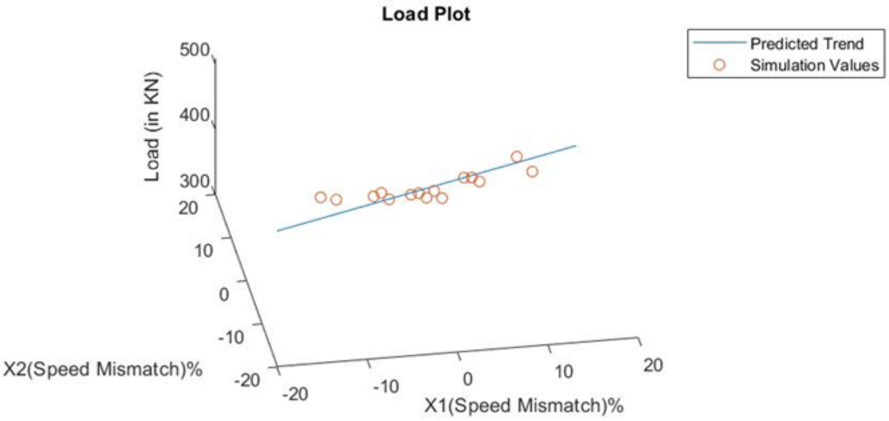

Figure 6-3: Regression Results for Load (By Author)

Some statistical values are stated in Tables 6-2, 6-3, and 6-4 to describe the statistical reliability of the regression analysis. The R-Squared Adjusted value signifies the fit percentage of the predicted trend. A high fit value signifies that the regression results obtained can accurately predict values. The p-Value is a measure of confidence for a regression parameter. A lower p-Value signifies that the parameter can be accepted into the result. This explanation follows from the F-test, a widely used statistical tool for regression analysis.

Table 6-2: Statistics Results for Torque Regression

Regression Parameters	**P-Value**	**Adjusted R-Squared Value**
a_0	$8.7306 \cdot 10^{-16}$	0.955
a_1	$4.4755 \cdot 10^{-6}$	
a_2	$8.181 \cdot 10^{-10}$	

Table 6-3: Statistics Results for Power Regression

Regression Parameters	**P-Value**	**Adjusted R-Squared Value**
a_0	$5.052 \cdot 10^{-16}$	0.961
a_1	$1.4928 \cdot 10^{-6}$	
a_2	$3.479 \cdot 10^{-10}$	

Table 6-4: Statistics Results for Load Regression

Regression Parameters	**P-Value**	**Adjusted R-Squared Value**
a_0	$3.1922 \cdot 10^{-21}$	0.945
a_1	0.0043681	
a_2	$2.2142 \cdot 10^{-8}$	

The regression analysis results help quantify the effect of speed mismatch on the technological parameters of rolling. With the help of the quantitative model obtained, a disturbance model is created, as shown below in Figure 6-4.

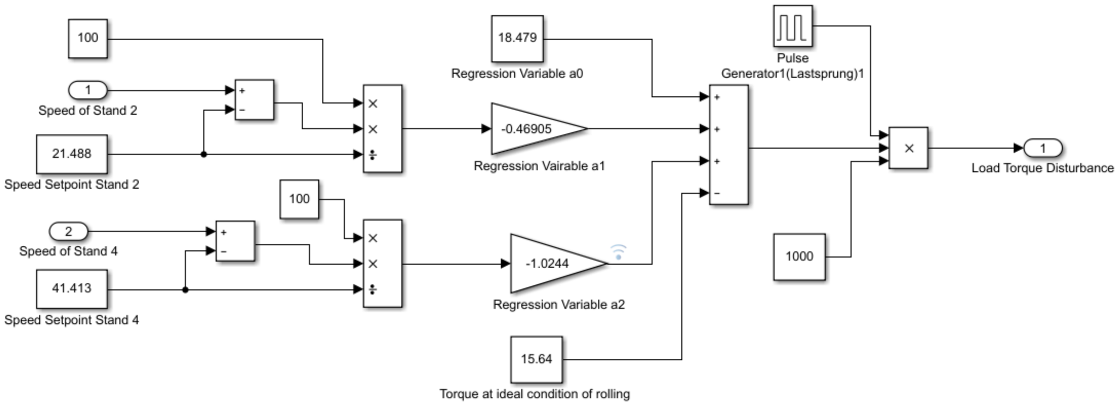

Figure 6-4: Disturbance Model (By Author)

6-2 Controller Analysis

The section will discuss the results obtained in the implementation of the controllers.

6-2-1 PID Controller

Figure 6-5 shows the implementation of the PID controller with the disturbance model shown in Figure 6-4.

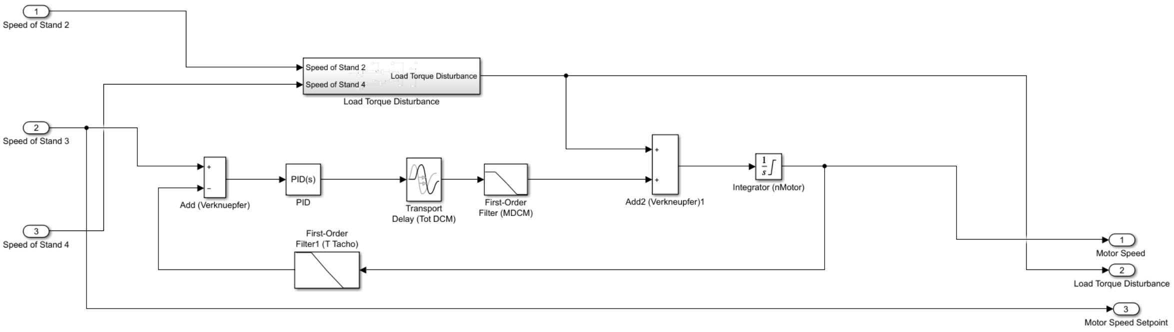

Figure 6-5: Implementation of PID controller with disturbance model (By Author)

Figures 6-6 and 6-7 show the results obtained from the PID controller for a step and piecewise disturbance following the tuning procedure mentioned in the previous chapter. We can conclude from the simulation results as follows:-

1. It is observed that there is a speed increase with the original controller at the use-case facility from 32.2 rpm to 38.7 rpm, an increase of 20.5%. With the modified controller action, the speed increase has been limited to 35.2 rpm, significantly improving the

rolling mill response by limiting the speed increase to only 9%. This is expected to positively influence the quality of the finished product and the stresses produced on the rolling mill during such severe speed mismatch scenarios.

2. There is no steady-state error in the response of the modified controller. The rolling mill stand can restore itself to its original set point post-disturbance. The settling time of the response is around 4 seconds. In contrast, with the current controller at the use-case facility, the mill needs operator intervention to restore itself to its set point. Hence, the modified controller action eliminates the steady-state error and requires no operator interference.

3. There is a higher undershoot in the modified controller's response compared to the original controller.

4. The modified controller can maintain the stability of the response in case the disturbance is injected into the system repeatedly.

The results and conclusions presented above have been formed after detailed discussions with the engineers and operators of the rolling mill at the use-case facility.

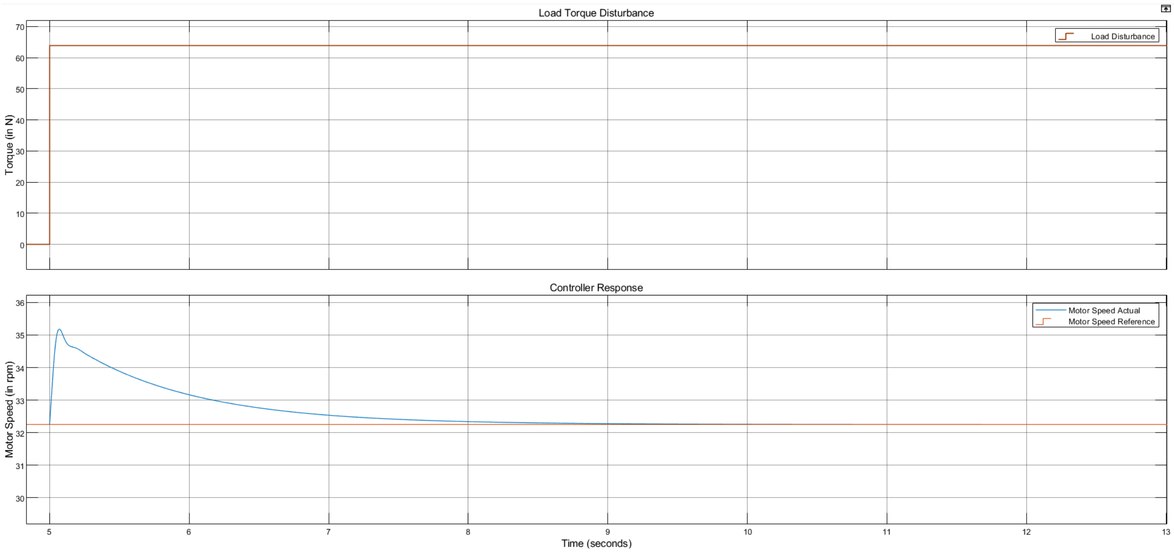

Figure 6-6: Results of PID controller with disturbance model for a step disturbance (By Author)

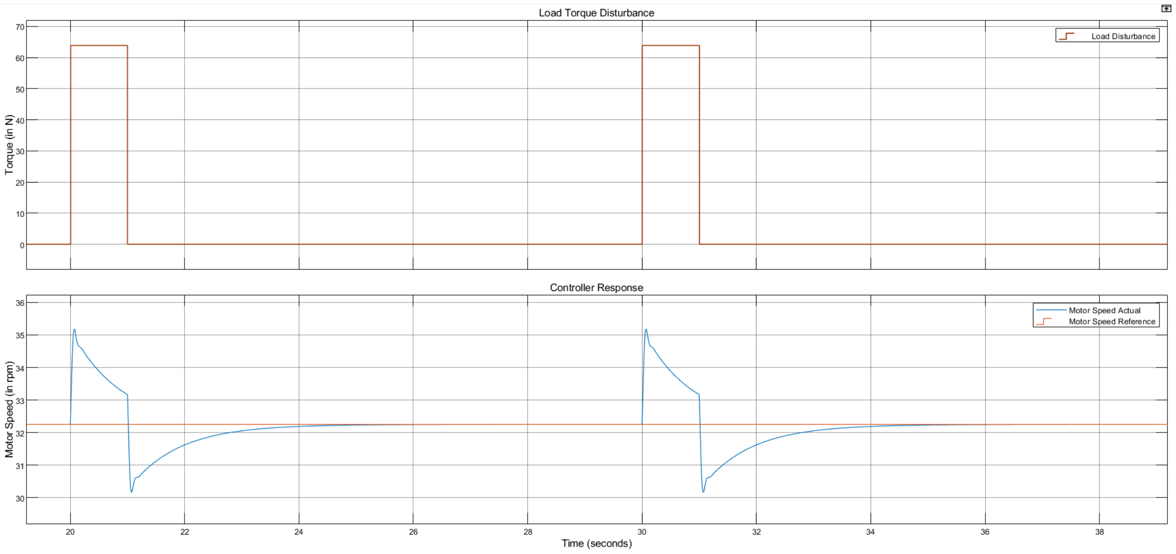

Figure 6-7: Results of PID controller with disturbance model for a piece-wise disturbance (By Author)

6-3 Linear Quadratic Regulator (LQR) Controller

Figure 6-8 shows the implementation of the Linear Quadratic Regulator (LQR) controller in Simulink.

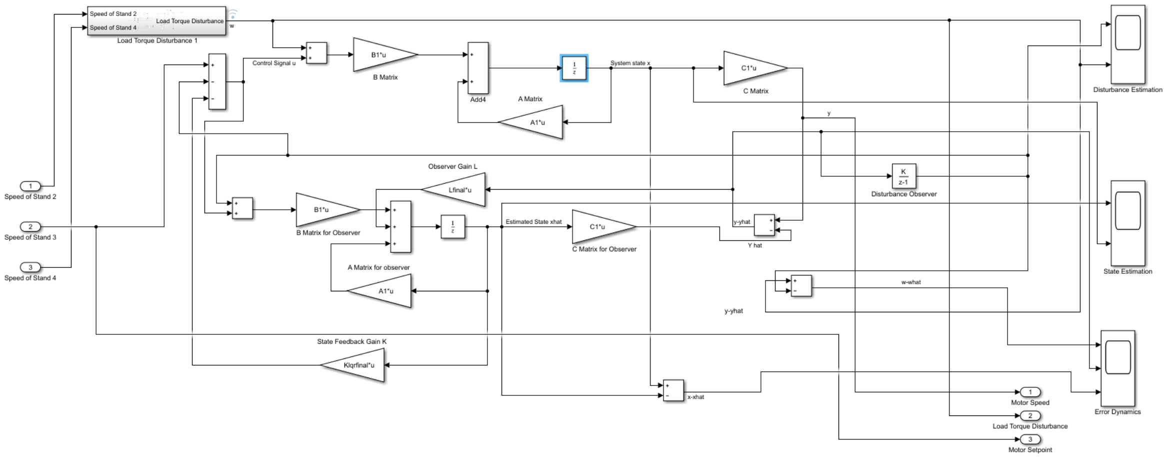

Figure 6-8: Implementation Model of the LQR Controller (By Author)

Figures 6-9 and 6-10 show the LQR controller results based on the design and tuning parameters mentioned in the previous chapter for a step and piece-wise disturbance.

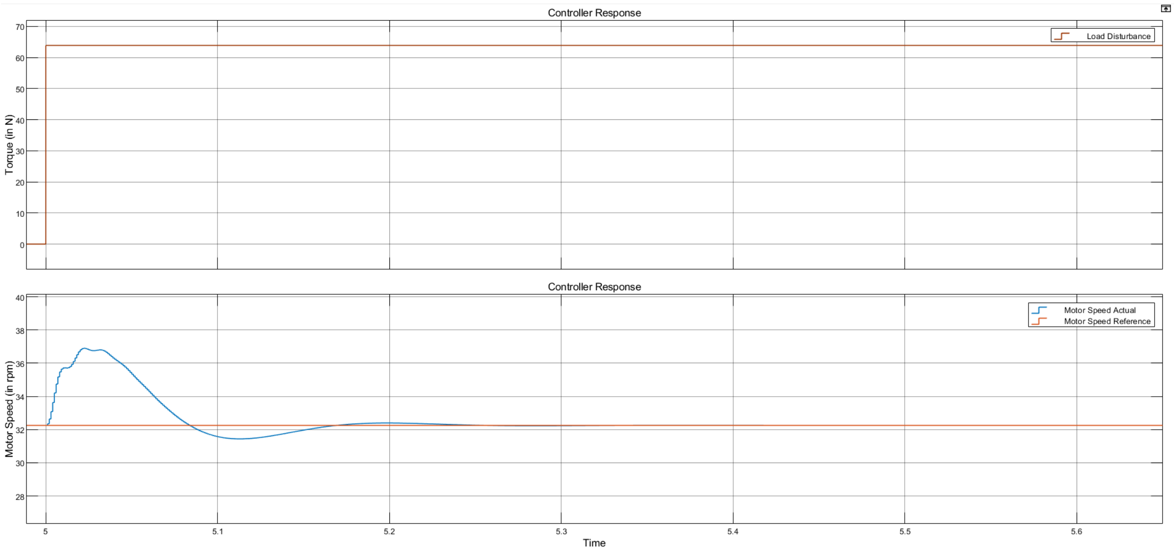

Figure 6-9: Results of LQR Controller for step disturbance (By Author)

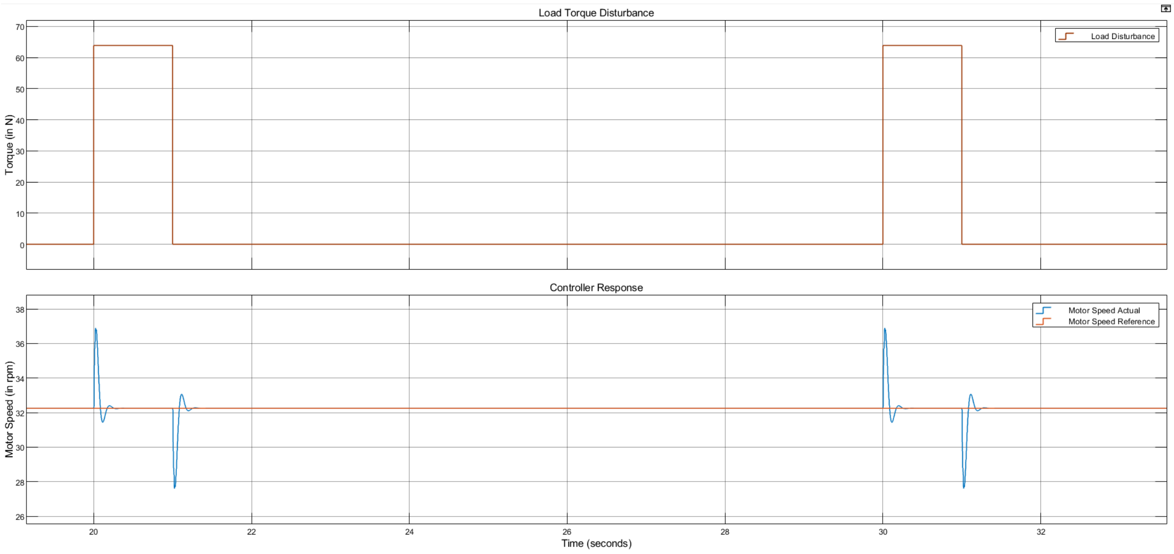

Figure 6-10: Results of LQR Controller for piece-wise disturbance (By Author)

In figures 6-9 and 6-6, a comparison is made between the performance of the PID and LQR controllers. We therefore make the following observations:-

1. The overshoot in the response of the system with LQR is higher as compared to the system with the PID controller.
2. There is a significant improvement in the system's settling time with the introduction of the LQR controller. The settling reduces from around 4 seconds to around 0.3 seconds.
3. Both systems can maintain their performance when the disturbance is introduced repeatedly into the system in the form of a piece-wise function.

6-4 Model Predictive Control (MPC) Controller

Figure 6-11 shows the Simulink model for implementing the Model Predictive Control (MPC) controller. Figures 6-12 and 6-13 show the system's response with the MPC controller for a step and piece-wise disturbance signal, respectively.

From Figures 6-12 and 6-13, we can make the following comments:-

1. The overshoot and undershoot in the response have improved significantly compared to the LQR controller.
2. The settling time of the system is around 0.3 seconds. This is quite similar to the settling time obtained from the LQR controller.
3. The controller can maintain the system's performance in the presence of a piece-wise disturbance.

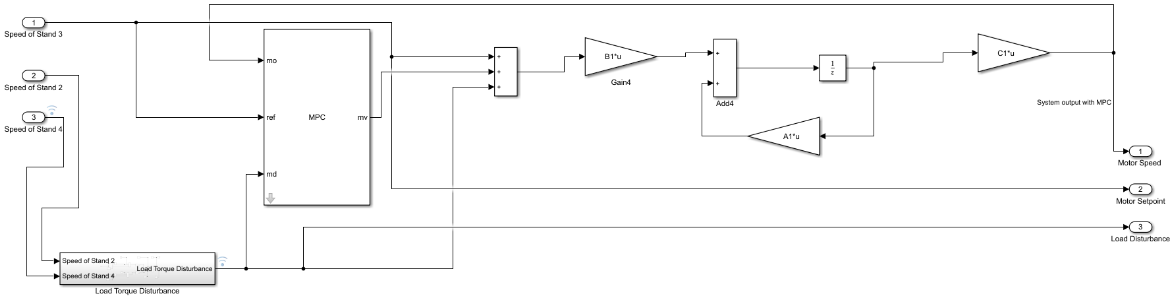

Figure 6-11: Implementation Model for MPC Controller (By Author)

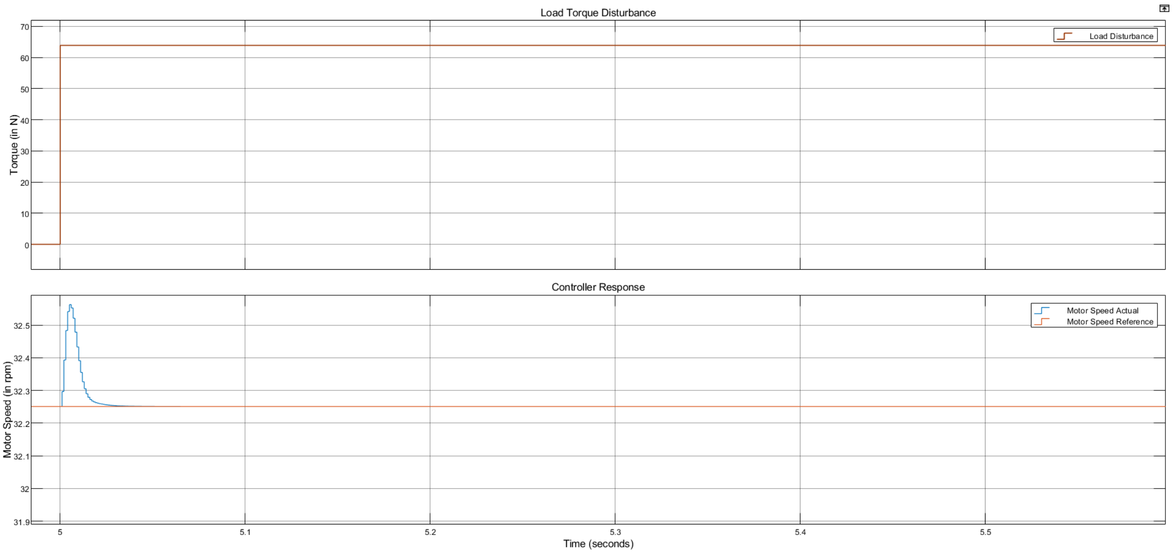

Figure 6-12: Results for MPC Controller with Step Disturbance (By Author)

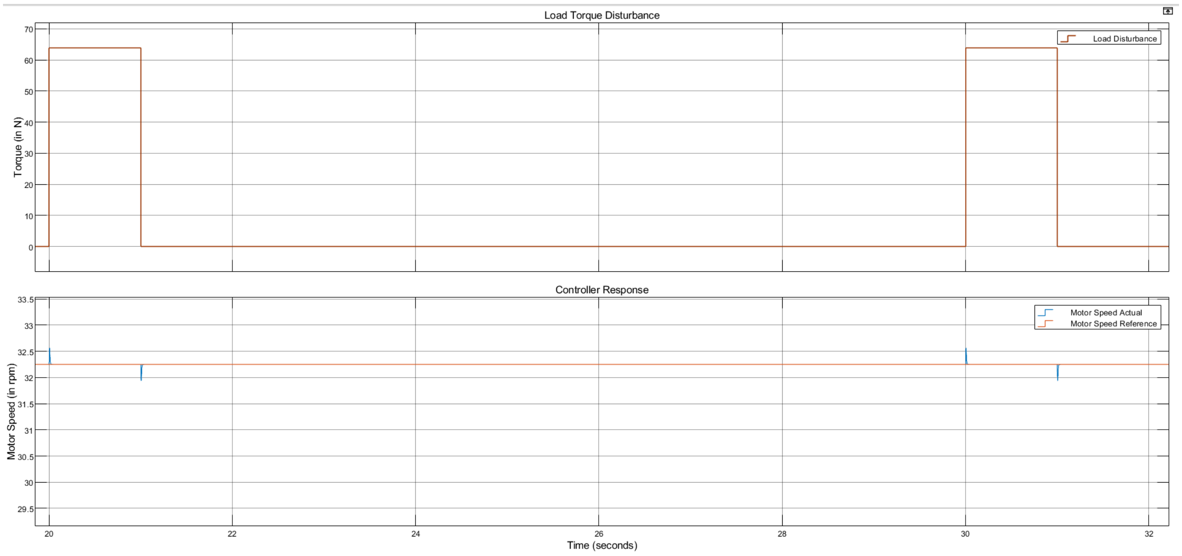

Figure 6-13: Results for MPC Controller with Piece-wise Disturbance (By Author)

Table 6-5 provides an overview of the performance of the controllers designed in the thesis for a step disturbance.

Table 6-5: Overview of the performance of controllers in thesis implementation

Characteristics	**Controller Type**			
	PID at Plant	**PID tuned**	**LQR**	**MPC**
Regulation (%)	9.05	9.05	14.41	0.017
Settling Time (sec)	371	5	0.325	0.26
Steady-State Error (rpm)	0.1	0	0	0

The table above shows the superior performance of the LQR and MPC controllers. The limitation in the usage of these controllers is that there is a need for the availability of the correct and accurate system models.

The subsequent chapter concludes the thesis and answers the third research question of the master thesis by shedding light on the future scope of the work conducted in this master thesis.

Chapter 7

Conclusion and Future Scope

The chapter will provide a brief conclusion of the thesis and future work that can be worked upon using the thesis as a starting point.

7-1 Conclusion

The master thesis aimed to quantitatively model the effect of speed mismatch on the technological parameters of steel rolling. The first step was to identify the factors that influence the stability of the steel rolling process. Some of the most prominent factors are:- speed mismatches in rolling stands, work roll wears in the rolling stands, the metallurgical composition of the workpieces, and the temperature (both along the surface and internal lattice) of the workpiece.

We selected to study the effect of speed mismatch on the technological parameters of steel for the thesis. A Finite-Element Method (FEM)-based simulator was set up using the design data of the work rolls and the workpiece in use at our use-case facility. The FEM simulations were conducted for a wide range of speed mismatches. A linear regression model was created to capture the effect of speed mismatches in consecutive stands on the middle stand's technological parameters (Load, Torque, and Power) in the philosophy of a three-stand system.

To further visualise the use of the disturbance model obtained with the help of the FEM simulations conducted in the speed control problem, simulations were created in MATLAB. These simulations take inspiration from the speed control strategy in use at the use-case facility for their Direct Current (DC) motor drives. The DC motor drives are used to power the rolling mill stands. The simulations conducted in MATLAB compare the controller in use at the use-case facility and the controllers implemented for performance improvement. A comparative study has been carried out between the implemented controllers and the controller at the use-case facility. The conclusion from the study is that the implemented controllers have a significant performance improvement in making the speed regulation of the rolling mill automated at the use-case facility. The autonomous operation of the rolling mill is a focus area for the use-case facility, and it is desired to achieve this by the end of

2030. The disturbance model obtained in the thesis work describes the effect of the speed mismatch on the technological parameters of steel rolling. The quantitative model obtained gives a new insight into the steel rolling process as until now, the disturbances in the steel rolling process have been understood only qualitatively and compensated for. The thesis provides motivates researchers in the steel rolling industry to obtain a more comprehensive disturbance model encompassing different factors that affect the stability of the steel rolling process. The performance enhancement demonstrated through the designed controllers should also motivate researchers to work on disturbance models since the designed controllers use a model-based approach to control of the rolling mills.

7-2 Future Scope

There are multiple areas where this thesis can be used as a starting point to further build on and try to achieve the goal of operator-less operation of the rolling mill.

The disturbance model may be further improved to ensure applicability with a wide range of workpieces. To achieve this, the following improvements are suggested:-

1. The wear of the work rolls is a significant factor that needs to be modelled. One of the ways this can be done is to form a regression model that explains the wear on the work rolls with respect to the tonnage of steel rolled. A wide range of equipment can be used to measure the work roll diameter. A decent interval to make a new measurement of the work roll diameter would be after every 6 tonnes of rolled steel, providing a reliable model of this factor.
2. The temperature of the workpiece also plays a role in changing the tension during the rolling process. To study this factor, the workpiece temperature has to be tracked back to the heating ovens before the workpiece enters the rolling mill. The temperature build-up in the workpiece in the oven has to be viewed in detail. The temperature build-up has to be studied for two main areas, along the surface of the workpiece and the internal lattice temperature. During this study, one must also keep in mind the effect of cold spots on the workpiece's surface when it is being moved inside the heating oven.
3. The factors mentioned above must be studied for a wide variety of metallurgical compositions of the workpiece. The use-case facility produces around 150 different qualities of wire rods. For building a comprehensive model, it is advised to consider the most widely produced qualities (in terms of tonnage) of wire rods.

Another area that can be worked upon is to expand the setup of the FEM-based simulator to capture the dynamics of the roughing and intermediate mill. The implementation of more features can be requested from the Qform group to help create a more realistic simulation of the rolling process.

After a comprehensive disturbance model is created, the area for autonomous operation of the rolling mill would be a significant step toward a new generation of rolling philosophy. Autonomous operation of the rolling mill would reduce operator influence on the quality of the end product. This would result in a significant cost saving for steel manufacturers in training operators.

Appendix A

Working of the Finite Element Method (FEM) tool QForm

A-1 Working of QForm Software

The mathematical formulation of the Finite- Element (FE) problem in QForm is based on the systems of equations which include the equilibrium equations (shown in (A-24)), compatibility equations (shown in (A-14)), constitutive equations (shown in (A-26)), incompressibility conditions (shown in (A-17)), yield criterion (shown in (A-28)), energy balance equations (shown in (A-34)). For the calculation of the flow stress (shown in (A-31)) in the material, the strain, strain rate, and temperature of the workpiece need to be provided as an input to the system [11]. The tensors values for strains and strain rates are available in the post-processor of QForm.

A-1-1 Strain Calculation

In order to characterise the finite strain, QForm employs the use of the Hencky finite strain tensor. It can be determined by taking the logarithm of a shape deformation matrix(elongation matrix) U as shown in (A-1) and can be expanded as shown in (A-2).

$$[\mathrm{E_L}] = ln\,[\mathrm{U}] \tag{A-1}$$

$$\mathrm{T_{E_L}} = \begin{bmatrix} \mathrm{E}_{11} & \mathrm{E}_{12} & \mathrm{E}_{13} \\ \mathrm{E}_{21} & \mathrm{E}_{22} & \mathrm{E}_{23} \\ \mathrm{E}_{31} & \mathrm{E}_{32} & \mathrm{E}_{33} \end{bmatrix} \tag{A-2}$$

In the post-processor of QForm, the displays of the strain tensor components follow the designations as $x - x_1$, $y - x_2$, and $z - x_3$ resulting in the tensor taking the form as shown in (A-3). For the resulting tensor, a coordinate system can be found where the tensor side components become zero. In physical terms, this means that the shear strain is absent in the coordinate system, meaning that the linear elements along this system's coordinate axes do not change their position. They can only elongate or stretch. Equation (A-4) shows the finite strain tensor for this system where strains E_1, E_2, and E_3 are the eigenvalues of the finite strain tensor and depict the strains in x, y, and z directions [11].

$$\mathrm{T}_{\mathrm{E_L}} = \begin{bmatrix} \mathrm{E}_{xx} & \mathrm{E}_{xy} & \mathrm{E}_{xz} \\ \mathrm{E}_{yx} & \mathrm{E}_{yy} & \mathrm{E}_{yz} \\ \mathrm{E}_{zx} & \mathrm{E}_{zy} & \mathrm{E}_{zz} \end{bmatrix} \tag{A-3}$$

$$\mathrm{T}_{\mathrm{E_L}} = \begin{bmatrix} \mathrm{E}_1 & 0 & 0 \\ 0 & \mathrm{E}_2 & 0 \\ 0 & 0 & \mathrm{E}_3 \end{bmatrix} \tag{A-4}$$

A multi-step summation method of incremental strains is used to determine the components of the finite strain tensor [11]. The algorithm is explained as follows:-

1. Using (A-5), the deformation gradient in the current step is determined. The derivative matrix, $\frac{\partial v_i}{\partial X_k}$ is determined in every finite element based on the velocity field approximation using the shape function.

$$\mathbf{F} = \frac{\partial \mathbf{x}}{\partial \mathbf{X}} = \mathbf{I} + \frac{\partial \mathbf{u}}{\partial \mathbf{X}}; \quad F_{ik} = \frac{\partial x_i}{\partial X_k} = \left(\delta_{ik} + \frac{\partial v_i}{\partial X_k}\Delta t\right), i,k = 1,2,3 \tag{A-5}$$

   Here:- v_i is the velocity of the mesh nodes at a time step Δt is the simulation step due to velocity δ_{ik} is called Kronecker delta (for $i = k$, it is 1 otherwise 0)

2. Right C and left B tensors for Cauchy-Green strains are determined using (A-6).

$$\begin{aligned} \mathbf{C} = \mathbf{F}^T\mathbf{F}; &\quad C_{ij} = F_{ji}F_{ij}, i,j = 1,2,3 \\ \mathbf{B} = \mathbf{F}\mathbf{F}^T; &\quad B_{ij} = F_{ij}F_{ji}, i,j = 1,2,3 \end{aligned} \tag{A-6}$$

3. Eigenvectors N and n of the primary coordinate system and tensors C and B are determined.

4. The rotation matrix $\mathbf{R}$ is determined as shown in (A-7), where $\otimes$ is the vector tensor product.

$$\mathbf{R} = \mathbf{n} \otimes \mathbf{N}; \quad R_{ij} = \begin{bmatrix} n_1N_1 & n_1N_2 & n_1N_3 \\ n_2N_1 & n_2N_2 & n_2N_3 \\ n_3N_1 & n_3N_2 & n_3N_3 \end{bmatrix} \tag{A-7}$$

5. Finite strain tensor $\mathbf{E}$ is determined using a strain accumulation at the current step with the rotation matrix as shown in (A-8). Superscripts $n+1, n$ represent the current and previous integration steps, and $\dot{\epsilon}_{ij}$ are the strain rate components [11].

$$\mathbf{E}^{n+1} = \mathbf{R}\left(\mathbf{E}^n + \dot{\epsilon}^n\Delta t\right)\mathbf{R}^T; \quad E_{ij}^{n+1} = R_{ij}\left(E_{ij}^n + \dot{\epsilon}_{ij}^n\Delta t\right)R_{ij}, i,j = 1,2,3 \tag{A-8}$$

A-1-2 Strain-Rate Calculation

The strain rate tensor takes the form shown in (A-9), where each element of the strain rate tensor is given in (A-10).

$$\mathrm{T}_{\dot{\epsilon}} = \begin{bmatrix} \dot{\epsilon}_{11} & \dot{\epsilon}_{12} & \dot{\epsilon}_{13} \\ \dot{\epsilon}_{21} & \dot{\epsilon}_{22} & \dot{\epsilon}_{23} \\ \dot{\epsilon}_{31} & \dot{\epsilon}_{32} & \dot{\epsilon}_{33} \end{bmatrix} \tag{A-9}$$

$$\dot{\epsilon}_{ij} = \frac{1}{2}\left(\frac{\partial v_i}{\partial x_j} + \frac{\partial v_j}{\partial x_i}\right), i, j = 1, 2, 3 \tag{A-10}$$

The components on the diagonals of the tensor in (A-9) represent the elongation rates of the linear elements parallel to the corresponding coordinate axes. The off-diagonal components represent the shear strain rates. After a suitable transformation, the strain rate tensor has the form as shown in (A-11), and the average strain rate is given by (A-12) [11].

$$\mathrm{T}_{\dot{\epsilon}} = \begin{bmatrix} \dot{\epsilon}_1 & 0 & 0 \\ 0 & \dot{\epsilon}_2 & 0 \\ 0 & 0 & \dot{\epsilon}_3 \end{bmatrix} \tag{A-11}$$

$$\dot{\epsilon}_m = \frac{1}{3}\left(\dot{\epsilon}_1 + \dot{\epsilon}_2 + \dot{\epsilon}_3\right) \tag{A-12}$$

The equivalent strain rate is calculated as shown in (A-13).

$$\dot{\bar{\epsilon}} = \frac{\sqrt{2}}{3}\sqrt{\left(\dot{\epsilon}_1 - \dot{\epsilon}_2\right)^2 + \left(\dot{\epsilon}_2 - \dot{\epsilon}_3\right)^2 + \left(\dot{\epsilon}_3 - \dot{\epsilon}_1\right)^2} \tag{A-13}$$

A-1-3 Matrix Representation of the Kinematic Equations

The Finite-Element Method (FEM) method implements the matrix representation of kinematic equations as shown below in (A-14).

$$\{\dot{\epsilon}\} = [\partial]\{v\} \tag{A-14}$$

where

$$\{\dot{\epsilon}\} = \begin{bmatrix} \dot{\epsilon}_{11} \\ \dot{\epsilon}_{22} \\ \dot{\epsilon}_{33} \\ \dot{\epsilon}_{12} \\ \dot{\epsilon}_{23} \\ \dot{\epsilon}_{31} \end{bmatrix} = \begin{bmatrix} \dot{\epsilon}_{xx} \\ \dot{\epsilon}_{yy} \\ \dot{\epsilon}_{zz} \\ \dot{\epsilon}_{xy} \\ \dot{\epsilon}_{yz} \\ \dot{\epsilon}_{zx} \end{bmatrix}$$

$$\{v\} = \begin{bmatrix} v_1 \\ v_2 \\ v_3 \end{bmatrix} = \begin{bmatrix} v_x \\ v_y \\ v_z \end{bmatrix}$$

$$[\partial] = \begin{bmatrix} \frac{\partial}{\partial x_1} & 0 & 0 \\ 0 & \frac{\partial}{\partial x_2} & 0 \\ 0 & 0 & \frac{\partial}{\partial x_3} \\ \frac{\partial}{2\partial x_2} & \frac{\partial}{2\partial x_1} & 0 \\ 0 & \frac{\partial}{2\partial x_3} & \frac{\partial}{2\partial x_2} \\ \frac{\partial}{2\partial x_3} & 0 & \frac{\partial}{2\partial x_1} \end{bmatrix}$$

A-1-4 Incompressibility Equation

To derive the incompressibility equation used by the QForm software, let us consider a parallelepiped with initial height, width, and length as H_0, B_0, L_0, respectively ,is compressed without friction. The dimensions of the deformed shape become H_1, B_1, L_1, as shown below in Figure A-1.

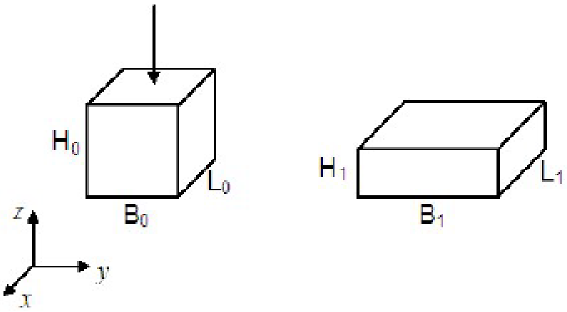

Figure A-1: Parallelepiped under deformation [11]

The initial and final volumes of the parallelepiped are given by (A-15).

$$\begin{aligned} V_0 &= H_0 B_0 L_0 \\ V_1 &= H_1 B_1 L_1 \end{aligned} \tag{A-15}$$

It is known using the law of constant volume, that the initial and final volume of the parallelepiped is equal. As a result, the following derivations are obtained.

$$\begin{aligned}&V_0 = V_1\\ &\frac{H_1 B_1 L_1}{H_0 B_0 L_0} = 1\\ &ln\frac{H_1}{H_0} + ln\frac{B_1}{B_0} + ln\frac{L_1}{L_0} = 0\end{aligned}$$

The sum in the derived expression represents the logarithmic strains in three mutually perpendicular directions. Thus, the sum of the strains in three mutually perpendicular directions at plastic deformation is always equal to zero, as shown in (A-16) [11].

$$\epsilon_{L_{xx}} + \epsilon_{L_{yy}} + \epsilon_{L_{zz}} = 0 \tag{A-16}$$

The plastic deformation rates follow the same property as that of the strains in (A-16), and as a result, we get (A-17). Equation (A-17) is known as the incompressibility equation.

$$\dot{\epsilon_{xx}} + \dot{\epsilon_{yy}} + \dot{\epsilon_{zz}} = 0 \tag{A-17}$$

A-1-5 Stress Calculation

The stress at a point in the workpiece is calculated using a set of normal and shear stresses in the three mutually perpendicular surface elements that pass through the point under consideration. The set of stresses in the three mutually perpendicular planes passing through the point under consideration forms the symmetric tensor of second-order. This tensor is termed the stress tensor and is shown in (A-18), where σ is the normal stress perpendicular to the surface and τ represents the shear stresses located in the surface plane. QForm software uses the momentless theory, implying that the stress tensor is symmetric. The average stress is given by (A-19) [11].

$$\mathrm{T}_\sigma = \begin{bmatrix}\sigma_x & \tau_{xy} & \tau_{xz}\\ \tau_{yx} & \sigma_y & \tau_{yz}\\ \tau_{zx} & \tau_{zy} & \sigma_z\end{bmatrix} \tag{A-18}$$

$$\sigma_m = \frac{1}{3}\left(\sigma_x + \sigma_y + \sigma_z\right) \tag{A-19}$$

The stress deviator tensor is derived by subtracting the average stress from the diagonal components of the stress tensor. Equations (A-20) and (A-21) show the stress deviator tensor and its shorthand denotation, respectively.

$$\mathrm{D}_\sigma = \begin{bmatrix}\sigma_x - \sigma_m & \tau xy & \tau xz\\ \tau yz & \sigma_y - \sigma_m & \tau_{yz}\\ \tau_{zx} & \tau_{zy} & \sigma_z - \sigma_m\end{bmatrix} = \begin{bmatrix}\sigma'_{11} & \sigma'_{12} & \sigma'_{13}\\ \sigma'_{21} & \sigma'_{22} & \sigma'_{23}\\ \sigma'_{31} & \sigma'_{32} & \sigma'_{33}\end{bmatrix} \tag{A-20}$$

$$\sigma'_{ij} = \sigma_{ij} - \delta_{ij}\sigma_m \quad (\delta_{ij} = 1, \text{for} \quad i = j, \text{else} \quad 0), i, j = 1, 2, 3 \tag{A-21}$$

A-1-6 Equilibrium Equations

For the workpiece under deformation, the stresses in any two points in the workpiece are different. Due to this, stress gradients are created, which cause metal flow. For a better understanding, consider stresses in two points, M and M*, located at an infinitely small distance from each other, as shown below in Figure A-2.

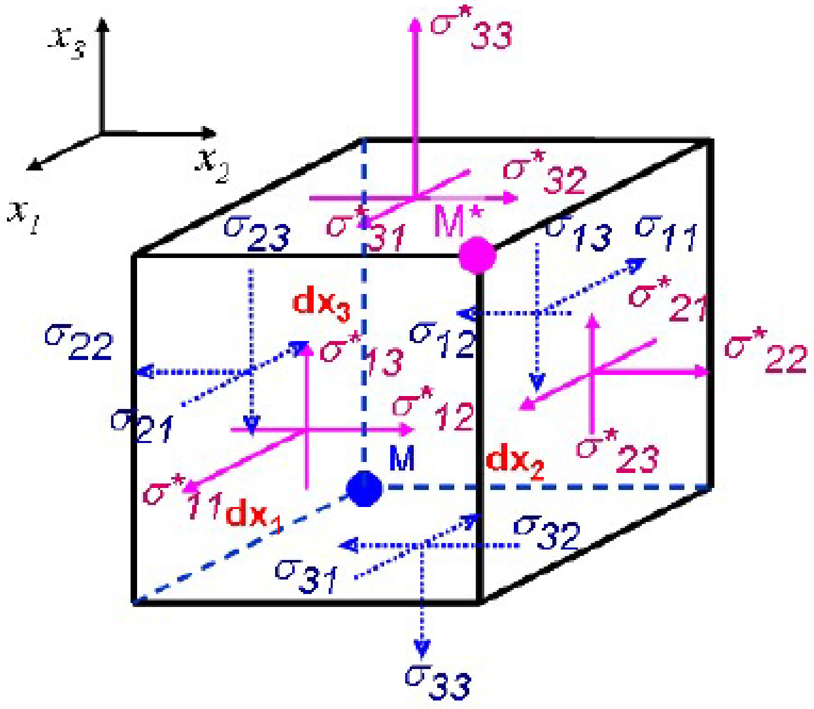

Figure A-2: Stresses in parallelepiped [11]

The parallel planes' stresses change proportion as shown in (A-22). Considering that the body is under the state of equilibrium, the sum of the projections of forces acting on the parallelepiped on every coordinate axis should be zero. Therefore, the equilibrium equations obtained for the parallelepiped are shown in (A-23) and can be written in shorthand (A-24).

$$\begin{aligned}\sigma{*}_{11} &= \sigma_{11} + \frac{\partial\sigma_{11}}{\partial x_1}dx_1\\ \sigma{*}_{12} &= \sigma_{12} + \frac{\partial\sigma_{12}}{\partial x_1}dx_1\\ \sigma{*}_{13} &= \sigma_{13} + \frac{\partial\sigma_{13}}{\partial x_1}dx_1\end{aligned} \tag{A-22}$$

$$\begin{aligned}
\frac{\partial\sigma_{11}}{\partial x_1}+\frac{\partial\sigma_{21}}{\partial x_2}+\frac{\partial\sigma_{31}}{\partial x_3}=0\\
\frac{\partial\sigma_{12}}{\partial x_1}+\frac{\partial\sigma_{22}}{\partial x_2}+\frac{\partial\sigma_{32}}{\partial x_3}=0\\
\frac{\partial\sigma_{13}}{\partial x_1}+\frac{\partial\sigma_{23}}{\partial x_2}+\frac{\partial\sigma_{33}}{\partial x_3}=0
\end{aligned} \tag{A-23}$$

$$\frac{\partial\sigma_{ij}}{\partial x_i}=0,\quad i,j=1,2,3 \tag{A-24}$$

A-1-7 Levy-Mises Constitutive Equations

In QForm, the elastic recovery of the workpiece is neglected for large plastic deformations in the workpiece. Therefore, the total strain in the workpiece amounts to the plastic strain. The mathematical description of constitutive equations for the medium gives us the Levy-Mises equations as shown in (A-25) [11].

$$\dot{\epsilon}_{ij}=\frac{3}{2}\frac{\bar{\epsilon}}{\bar{\sigma}}\dot{\sigma}'_{ij} \tag{A-25}$$

Here:-

$\bar{\sigma}$ is the effective stress, $\dot{\bar{\epsilon}}$ is the effective deformation rate, $\dot{\epsilon}_{ij}$ is the strain tensor, σ'_{ij} is the stress deviator.

The FEM uses the Levy-Mises constitutive equations as shown in (A-26).

$$\begin{gathered}
\{\sigma'\}=\frac{\bar{\sigma}}{\dot{\bar{\epsilon}}}[D]\{\dot{\epsilon}\}\\
\{\sigma\prime\}=\begin{bmatrix}\sigma_{xx}-\sigma_m\\ \sigma_{yy}-\sigma_m\\ \sigma_{zz}-\sigma_m\\ \sigma_{xy}\\ \sigma_{yz}\\ \sigma_{zx}\end{bmatrix}\quad
\{\dot{\epsilon}\}=\begin{bmatrix}\dot{\epsilon}_{xx}\\ \dot{\epsilon}_{yy}\\ \dot{\epsilon}_{zz}\\ \dot{\epsilon}_{xy}\\ \dot{\epsilon}_{yz}\\ \dot{\epsilon}_{zx}\end{bmatrix}\quad
[D]=\frac{2}{3}\begin{bmatrix}1&0&0&0&0&0\\0&1&0&0&0&0\\0&0&1&0&0&0\\0&0&0&2&0&0\\0&0&0&0&2&0\\0&0&0&0&0&2\end{bmatrix}
\end{gathered} \tag{A-26}$$

Here:- $\{\sigma'\}$ is the stress deviator column matrix, $\{\dot{\epsilon}\}$ is the strain rate column matrix, D is the coupling matrix.

A-1-8 Von Mises Yield Criterion

The yield criterion is an expression constraining stress components in a point and determining the transition to a plastic state [11]. For uniaxial tension, a plastic state arises when the tensile stress σ_1 achieves the yield stress threshold σ_Y. Beyond this threshold, the relationship between stress and strain is no longer linear. This can be seen in Figure A-3.

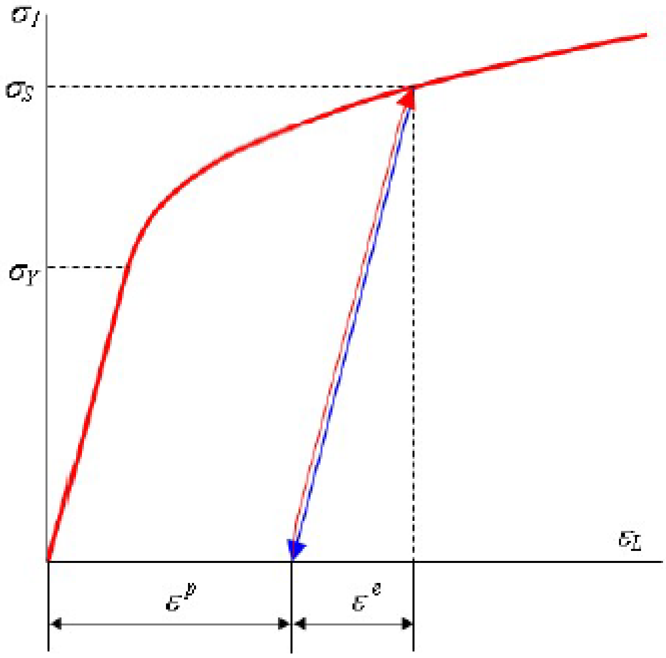

Figure A-3: Stress vs Strain Graph [11]

Equation (A-27) presents the general form of the yield criterion where σ_{ij} and σ_S represent the stress tensor components and the material's resistance to plastic deformation, respectively.

$$f\left(\sigma_{ij}, \sigma_S\right) = 0 \tag{A-27}$$

QForm uses the Von-Mises criterion (shown in (A-28)) for the plastic deformation of the workpiece, which states that in the plastic state, the effective stress is equal to the flow stress of the material. The Von-Mises criterion states that the transition to a plastic state occurs when the deformation-specific energy of the material is attained. It also signifies that it is not dependent on the stressed state mechanism and is purely based on the characteristics of the material of the workpiece.

$$\bar{\sigma} = \sigma_S \tag{A-28}$$

From the Von-Mises criterion, the maximum shear stress depends on the metal flow. It cannot exceed the values shown in (A-29) at plastic deformation, where k is the maximum shear stress.

$$\tau_{\max} \leq k = \frac{\sigma_S}{\sqrt{3}} \tag{A-29}$$

A-1-9 Friction Laws

Several laws can be used to model the friction between the workpiece and the work rolls. These are Coulumb's law, Siebel's law, Levanov's law, and a combination of Coulumb's and

Siebel's law. For the simulations conducted in the thesis, the law selected was Siebel's friction law. According to the law, the specific friction force is proportional to the maximum shear stress at shear k, as shown in (A-30). m is the friction factor and takes a value between 0 and 1. The selection of Siebel's friction law is based on the fact that during longitudinal rolling, the ratio of normal stress to flow stress is large [11].

$$\tau = mk \tag{A-30}$$

A-1-10 Flow Stress

Flow stress is the effective stress acting at uniaxial tension along the sample axis in uniform deformation. During plastic deformation, the flow stress usually increases. In QForm, a strain hardening hypothesis is implemented based on which the hardening quantity is determined with the effective plastic strain. Equation (A-31) shows the function of the flow stress as a function of effective strain, strain rate, and temperature. It describes the behaviour of the workpiece material at plastic deformation independent of the stress state mechanism [11].

$$\begin{aligned}\sigma_S &= f\left(\epsilon^p_{ef}, \dot{\bar{\epsilon}}, T\right)\\ \epsilon^p_{ef} &= \int_t \dot{\bar{\epsilon}}^p dt\end{aligned} \tag{A-31}$$

A-1-11 Energy Balance Equations

The conservation of mechanical energy of the deformed body in the absence of the inertial loads states that the power of specific external forces p applied to the outer surface F of the deformed body is equal to power developed by stresses σ over the strain rate in the volume of the deformed body V and is shown in (A-32) [11].

$$\int\int_F p_i v_i dF = \int\int\int_V \sigma_{ij}\dot{\epsilon}_{ij} dV \tag{A-32}$$

Here:- $i.j = x, y, z$, which are the coordinate axes, v_i is the projections of the velocities of the surface material points on the coordinate axes.

For plastic deformation simulation in QForm, Markov's variational principle, as shown in (A-33), is used. The first integral of the function reflects the power of plastic strain, and the second integral reflects the power of external forces. QForm uses the Markov's functionality in the matrix form as shown in (A-34), where $\{v\}$ and $\{p\}$ are the matrix vectors of material points' velocities and known specific forces on the external surface [11].

$$\Phi = \int\int\int_V \bar{\sigma}\dot{\bar{\epsilon}} dV - \int\int_{F_p} p_i v_i dF \tag{A-33}$$

$$\Phi = \int\int\int_V \bar{\sigma}\dot{\bar{\epsilon}} dV - \int\int_{F_p} \{v^T\}\{p\} dF \tag{A-34}$$

A-1-12 Systems of Equations for Plastic Deformation

The preceding sections describe the various individual equations that form the system of equations that QForm solves to simulate the plastic deformation problem. The equations are summarised below as follows:-

- Equilibrium Equations

$$\frac{\partial \sigma_{ij}}{\partial x_i} = 0 \quad i,j = 1,2,3$$

- Compatibility conditions between velocity field and strain rate components

$$\dot{\epsilon_{ij}} = \frac{1}{2}\left(\frac{\partial v_i}{\partial x_j} + \frac{\partial v_j}{\partial x_i}\right) \quad i,j = 1,2,3$$

- Levy-Mises constitutive equations that present the mathematical relationship between stressed and strained states

$$\dot{\epsilon}_{ij} = \frac{3}{2}\frac{\dot{\bar{\epsilon}}}{\bar{\sigma}}\sigma'_{ij} \quad i,j = 1,2,3$$

- Incompressibility condition from the law of constant volume

$$3\dot{\epsilon}_m = \dot{\epsilon}_{ii} = 0 \quad i = 1,2,3$$

- Essential boundary conditions on the surface F_v

$$v_i = v_{0i}$$

- Natural boundary conditions on the surface F_p

$$p_i = p_{0i}$$

- Von Mises yield criterion

$$\bar{\sigma} = \sigma_S$$

- Rheological model of the material of the workpiece, which is also the expression for flow stress

$$\sigma_S = f\left(\epsilon^p_{ef}, \dot{\bar{\epsilon}}, T\right)$$

- Satisfaction of the balance differential equations according to the Markov's variational principle

$$\delta\Phi = \int\int\int_V \bar{\sigma}\delta\dot{\bar{\epsilon}}dV - \int\int_{F_p} p_i\delta v_i dF = 0 \qquad \text{(A-35)}$$

A-1-13 Solution of plastic deformation problem in Qform

For the solution of the plastic deformation problem, QForm uses a set of discrete equations that can be derived from Markov's variational principle (A-35). The necessary condition is shown in (A-36) to minimize Markov's variational principle function.

$$\frac{\partial\Phi}{\partial\{v\}} = 0 \tag{A-36}$$

The velocity field in (A-36) for every FE is dependent on the shape function and the FE nodal velocities, as shown in (A-37). For the 3D plastic deformation problem, the shape function is chosen to be a tetrahedron. The tetrahedron shape function consists of 5 nodes, each of which possesses 3 degrees of freedom. The nodal velocity matrix, therefore, becomes a column matrix with dimension 15. The shape function matrix becomes a matrix with a dimension of 315.

$$\{v\} = [N]\left\{v^{(e)}\right\} \tag{A-37}$$

Using the Von-Misses yield criterion shown in (A-28) and the help of shape functions, the strain rates can be found for the nodal velocities as shown below in (A-38). Here, $[B]$ is the matrix of gradients, signifies the shape function's derivatives with respect to the spatial coordinates and has a dimension of 615.

$$\{\dot{\epsilon}\} = [B]\left\{v^{(e)}\right\} \tag{A-38}$$

Equation (A-39) shows the effective strain rate for the incompressible body in matrix form.

$$\dot{\bar{\epsilon}} = \sqrt{\{\dot{\epsilon}^T\}\,[D]\,\{\dot{\epsilon}\}} \tag{A-39}$$

Where [D] is the same as in (A-26).

We now obtain the function we need to minimise, as shown in (A-40).

$$\Phi = \sum_e \int_{V^{(e)}} \sigma_S \sqrt{\{v^{(e)}\}^T\,[B]^T\,[D]\,[B]\,\{v^{(e)}\}}dV - \sum_e \int_{F_p^{(e)}} \left\{v^{(e)}\right\}^T [N]^T\,\{p\}dF \tag{A-40}$$

This function does not include the constraint for constant volume, which can be written as shown in (A-41).

$$\begin{aligned} \dot{\epsilon}_v &= \dot{\epsilon}_{xx} + \dot{\epsilon}_{yy} + \dot{\epsilon}_{zz} = 0 \\ &= \begin{bmatrix}1 & 1 & 1 & 0 & 0 & 0\end{bmatrix}\{\dot{\epsilon}\} = 0 \\ &= [I][B]\left\{v^{(e)}\right\} = 0 \\ &= [E]\left\{v^{(e)}\right\} = 0 \end{aligned} \tag{A-41}$$

In order to take into account the incompressibility, Markov's functionality is modified by introducing the constraints shown in (A-41) based on the Lagrange multiplier concept. Equation (A-42) represents this updated function where the Lagrange multipliers are considered the mean stress σ_m.

$$\begin{aligned}
\Phi^* &= \Phi + \int\int\int_V \lambda\dot{\epsilon}_v dV \\
\Phi^* &= \int\int\int_V \bar{\sigma}\dot{\bar{\epsilon}} + \int\int\int_V \lambda\dot{\epsilon}_v dV - \int\int_{F_p} \{v\}^T \{p\}\, dF \\
\Phi^* &= \sum_e \int_{V^{(e)}} \sigma_S \sqrt{\{v^{(e)}\}^T [B]^T [D] [B] \{v^{(e)}\}} dV + \sum_e \int_{V^{(e)}} [N^*] \left\{\sigma_m^{(e)}\right\} [E] \left\{v^{(e)}\right\} dV \\
&\quad - \sum_e \int_{F_p^{(e)}} \left\{v^{(e}\right\}^T [N]^T \{p\}\, dF \\
\Phi^* &= \sum_e \int_{V^{(e)}} \sigma_S \sqrt{\left\{\dot{U}\right\}^T [B]^T [D] [B] \left\{\dot{U}\right\}} dV + \sum_e \int_{V^{(e)}} \left\{\dot{U}\right\}^T [E]^T [N^*] \{S\}\, dV \\
&\quad - \sum_e \int_{F_p^{(e)}} \left\{\dot{U}\right\}^T [N]^T \{p\} dF
\end{aligned} \tag{A-42}$$

Here, $\left\{\dot{U}\right\}$ and $\{S\}$ are the nodal velocity vector in the global coordinate system and the mean stress nodal value vector, respectively. These are defined as shown in (A-43), where $iv = 1, \ldots Nv$ is the number of nodes used for approximating the velocity field, $j = 1, 2, 3$ is the degrees of freedom in every node and $is = 1, \ldots, Ns$ is the number of nodes for approximating the average stress field.

$$\left\{\dot{U}\right\} = \left\{\begin{matrix} v_{1,1} \\ v_{1,2} \\ v_{1,3} \\ \cdots \\ v_{iv,j} \\ \cdots \\ v_{Nv,1} \\ v_{Nv,2} \\ v_{Nv,3} \end{matrix}\right\} \quad \{S\} = \left\{\begin{matrix} (\sigma_m)_1 \\ \cdots \\ (\sigma_m)_{is} \\ \cdots \\ (\sigma_m)_{Ns} \end{matrix}\right\} \tag{A-43}$$

Equation (A-44) depicts the conditions for the minimum of the functional.

$$\begin{cases} \dfrac{\partial \Phi^*}{\partial \{\dot{U}\}} = 0 \\ \left(\sum_e \int_{V^{(e)}} \dfrac{\sigma_S}{\dot{\bar{\epsilon}}} \left[B\right]^T \left[D\right] \left[B\right] dv\right) \left\{\dot{U}\right\} + \left(\sum_e \int_{V^{(e)}} \left[E\right]^T \left[N^*\right] dV\right) \{S\} - \sum_e \int_{F_p^{(e)}} \left[N'\right]^T \{p\} dF = 0 \\ \dfrac{\partial \Phi^*}{\partial \{S\}} = 0 \\ \left(\sum_e \int_{V^{(e)}} \left[N^*\right]^T \left[E\right] dV\right) \left\{\dot{U}\right\} = 0 \end{cases} \tag{A-44}$$

Using the matrix transformations shown in (A-45), the global equation of systems is obtained as shown in (A-46), where $[K]$ is the global stiffness matrix, $[Z]$ and $[R]$ are the vector of nodal unknowns, and vector for external loads, respectively.

$$\begin{aligned} \left[a\right]^T &= \left(\left[b\right]\left[c\right]\right)^T = \left[c\right]^T \left[b\right]^T \\ \frac{\partial}{\partial \left[a\right]} &\left(\left[s\right]^{T\left[b\right]\left[a\right]}\right) = 2\left[b\right]\left[a\right] \\ \frac{\partial}{\partial \left[a\right]} &\left(\left[a\right]^T \left[b\right]\right) = \left[b\right] \end{aligned} \tag{A-45}$$

$$\begin{aligned} &\left[K\right]\{Z\} = \{R\} \\ &\left[K\right] = \begin{bmatrix} \left[K_{11}\right] & \left[K_{12}\right] \\ \left[K_{21}\right] & 0 \end{bmatrix} \\ &\left[K_{11}\right] = \sum_e \left[K_{11}^{(e)}\right] = \sum_e \int_{V^{(e)}} \frac{\sigma_S}{\dot{\bar{\epsilon}}} \left[B\right]^T \left[D\right] \left[B\right] dV \\ &\left[K_{21}\right] = \sum_e \left[K_{21}^{(e)}\right] = \sum_e \int_{V^{(e)}} \left[N^*\right]^T \left[E\right] dV \\ &\left[K_{12}\right] = \sum_e \left[K_{12}^{(e)}\right] = \sum_e \int_{V^{(e)}} \left[E\right]^T \left[N^*\right] dV \\ &\{Z\} = \left\{ \begin{array}{c} \left\{\dot{U}\right\} \\ \{S\} \end{array} \right\} \\ &\{R\} = \left\{ \begin{array}{c} \{R_1\} \\ 0 \end{array} \right\} = \left\{ \begin{array}{c} \sum_e \int_{F_p^{(e)}} \left[N\right]^T \{p\} dF \\ 0 \end{array} \right\} \end{aligned} \tag{A-46}$$

The equation described in (A-46) is non-linear and is solved using a multi-step iteration method. The solutions obtained after solving the equation are the velocity and the average stress. These solutions can then be further used to calculate various other values during the plastic deformation simulation in QForm.

Appendix B

Theoretical Analysis

B-1 Analysis for rolling mode (-10,10)

The speed mismatch is calculated using (3-25) as:-

$$\mathrm{X1} = \frac{19.339 - 21.488}{21.488} \times 100 = -10\%$$
$$\mathrm{X2} = \frac{45.554 - 41.413}{41.413} \times 100 = 10\%$$

The external coefficient of friction is calculated using (3-21) as:-

$$\mathrm{f} = (1.05 - 0.0005 \times 1050) = 0.525$$

The bite angle for the rolling mill stand is calculated using (3-22) as:-

$$\alpha = 2 \arcsin \sqrt{\frac{0.12029 - 0.0673049}{2 \times 2 \times 0.196421}} = 0.\text{ radians}$$

The deformation ratio for the three stands are calculated using (3-23) as:-

$$\lambda_2 = 1.382;$$
$$\lambda_3 = 1.356;$$
$$\lambda_4 = 1.333$$

For calculating the lead of metal for the three stands, (3-24) is used and we as follows:-

$$\mathrm{S}_2 = \frac{0.500793 - 0.455101}{0.455101} = 0.1003$$
$$\mathrm{S}_3 = \frac{0.709948 - 0.66337}{0.66337} = 0.0701$$
$$\mathrm{S}_4 = \frac{1.02605 - 0.99055}{0.99055} = 0.0358$$

The front and the rear tension for the middle stand can be calculated using (3-26) as:-

$$\sigma_0 = \frac{1}{0.045}\left[\left(\frac{32.2507}{19.339}\right) - \left(\frac{32.2507}{21.488}\right)\right]\left[\frac{0.196421}{0.224836}\cdot\frac{1}{1.356}\cdot\frac{1+0.0701}{1+0.1003}\right] = 2.1026\,\mathrm{MPa}$$
$$\sigma_1 = \frac{1}{0.045}\left[\left(\frac{45.554}{32.25707}\right) - \left(\frac{41.413}{32.2507}\right)\right]\left[\frac{0.207552}{0.196421}\cdot\frac{1}{1.333}\cdot\frac{1+0.0358}{1+0.0701}\right] = 1.9884\,\mathrm{MPa}$$

Equation (3-27) is used for finding out the resultant tension on the stand under consideration:-

$$\sigma_\Sigma = \sigma_0 - \sigma_1 = 0.33018\,\mathrm{MPa}$$

The length of the deformation zone of the stand follows from (3-31) as:-

$$\mathrm{l_c} = \sqrt{(0.12029 - 0.0673049)\times 0.196421} = 0.10201\,\mathrm{m}$$

The projection of the area of contact between the work roll and the workpiece follows from (3-30) as:-

$$\mathrm{F_k} = \frac{0.0639513 + 0.0752961}{2}\times 0.10201 = 0.00710231\mathrm{m}^2$$

The term η is calculated using (3-33) as:-

$$\frac{1}{\eta} = \frac{0.12029}{0.0673049} = 1.7872$$

The change in the rolling moment of the stand under the influence of inter-stand tension follows from (3-29) as:-

$$\Delta\mathrm{M} = \frac{0.00626\times 0.091}{1.586 - 1}\times 0.33018 = 0.101343\,\mathrm{KNm}$$

The entire back and front tension in the workpiece is calculated by using (3-28) as:-

$$\mathrm{T_0} = 2.1026\times 0.645634 = 1.3575\,\mathrm{MN}$$
$$\mathrm{T_1} = 1.9884\times 0.428705 = 0.8524\,\mathrm{MN}$$

The deformation in the workpiece follows from (3-20) as:-

$$\delta = \frac{2\times 0525}{0.525} = 2$$

With the use of (3-32), the change in roll pressure on the workpiece in the presence of inter-stand tension is given as:-

$$\Delta\mathrm{p} = -\left\{\left[\left(1.787 - 1.787^{0.25}\right)\cdot\frac{2.1026}{0.787}\right] - \left[\left(1.787^{0.25} - 1\right)\cdot\frac{1.9884}{0.787}\right]\right\} = -1.69558\,\mathrm{MPa}$$

With the use of (3-34), the torque on the stand can be calculated as follows:-

$$\mathrm{M_H} = 0.196421\cdot\left(\frac{1.3575}{1.356} - 0.8524\right)\cdot(1+0.0701) = 28.38\,\mathrm{KNm}$$

B-2 Analysis for rolling mode (5,-5)

The speed mismatch is calculated using (3-25) as:-

$$\begin{aligned}\mathrm{X1} &= \frac{22.562 - 21.488}{21.488} \times 100 = 5\% \\ \mathrm{X2} &= \frac{39.342 - 41.413}{41.413} \times 100 = -5\%\end{aligned}$$

The external coefficient of friction is calculated using (3-21) as:-

$$\mathrm{f} = (1.05 - 0.0005 \times 1050) = 0.525$$

The bite angle for the rolling mill stand is calculated using (3-22) as:-

$$\alpha = 2\arcsin\sqrt{\frac{0.10684 - 0.0736316}{2 \times 2 \times 0.196421}} = 0.4141\,\text{radians}$$

The deformation ratio for the three stands are calculated using (3-23) as:-

$$\begin{aligned}\lambda_2 &= 1.382; \\ \lambda_3 &= 1.356; \\ \lambda_4 &= 1.333\end{aligned}$$

For calculating the lead of metal for the three stands, (3-24) is used and we as follows:-

$$\begin{aligned}\mathrm{S}_2 &= \frac{0.568061 - 0.530947}{0.530947} = 0.06 \\ \mathrm{S}_3 &= \frac{0.721714 - 0.66337}{0.66337} = 0.08 \\ \mathrm{S}_4 &= \frac{0.924286 - 0.8554803}{0.8554803} = 0.08\end{aligned}$$

The front and the rear tension for the middle stand can be calculated using (3-26) as:-

$$\begin{aligned}\sigma_0 &= \frac{1}{0.045}\left[\left(\frac{32.2507}{22.562}\right) - \left(\frac{32.2507}{21.488}\right)\right]\left[\frac{0.196421}{0.224836} \cdot \frac{1}{1.356} \cdot \frac{1+0.08}{1+0.06}\right] = -1.0421\,\text{MPa} \\ \sigma_1 &= \frac{1}{0.045}\left[\left(\frac{39.342}{32.25707}\right) - \left(\frac{41.413}{32.2507}\right)\right]\left[\frac{0.207552}{0.196421} \cdot \frac{1}{1.333} \cdot \frac{1+0.08}{1+0.08}\right] = -1.13119\,\text{MPa}\end{aligned}$$

Equation (3-27) is used for finding out the resultant tension on the stand under consideration:-

$$\sigma_\Sigma = \sigma_0 - \sigma_1 = 0.08909\,\text{MPa}$$

The length of the deformation zone of the stand follows from (3-31) as:-

$$\mathrm{l_c} = \sqrt{(0.10684 - 0.0736316) \times 0.196421} = 0.0807\,\mathrm{m}$$

The projection of the area of contact between the work roll and the workpiece follows from (3-30) as:-

$$\mathrm{F_k} = \frac{0.0636498 + 0.0752538}{2} \times 0.0807 = 0.005604\mathrm{m}^2$$

The term η is calculated using (3-33) as:-

$$\frac{1}{\eta} = \frac{0.0736316}{0.10684} = 0.68917$$

The change in the rolling moment of the stand under the influence of inter-stand tension follows from (3-29) as:-

$$\Delta\mathrm{M} = \frac{0.005604 \times 0.0807}{0.68917 - 1} \times 0.08909 = -0.129621\,\mathrm{KNm}$$

The entire back and front tension in the workpiece is calculated by using (3-28) as:-

$$\begin{aligned}\mathrm{T}_0 &= -1.0421 \times 0.593471 = -0.618456\,\mathrm{MN}\\ \mathrm{T}_1 &= -1.13119 \times 0.457583 = -0.517613\,\mathrm{MN}\end{aligned}$$

The deformation in the workpiece follows from (3-20) as:-

$$\delta = \frac{2 \times 0525}{0.4141} = 2.535$$

With the use of (3-32), the change in roll pressure on the workpiece in the presence of inter-stand tension is given as:-

$$\Delta\mathrm{p} = -\left\{\left[\left(0.68917 - 0.68917^{0.302}\right) \cdot \frac{-1.0421}{-0.31083}\right] - \left[\left(0.68917^{0.302} - 1\right) \cdot \frac{-1.13119}{-0.31083}\right]\right\} = 0.29859\mathrm{MPa}$$

With the use of (3-34), the torque on the stand can be calculated as follows:-

$$\mathrm{M_H} = 0.196421 \cdot \left(\frac{-0.618456}{1.356} + 0.517613\right) \cdot (1 + 0.08) = 13.05\,\mathrm{KNm}$$

B-3 Analysis for rolling mode (10,-10)

The speed mismatch is calculated using (3-25) as:-

$$\begin{aligned}\mathrm{X1} &= \frac{23.636 - 21.488}{21.488} \times 100 = 10\%\\ \mathrm{X2} &= \frac{37.271 - 41.413}{41.413} \times 100 = -10\%\end{aligned}$$

The external coefficient of friction is calculated using (3-21) as:-

$$\mathrm{f} = (1.05 - 0.0005 \times 1050) = 0.525$$

The bite angle for the rolling mill stand is calculated using (3-22) as:-

$$\alpha = 2\arcsin\sqrt{\frac{0.104089 - 0.0765497}{2 \times 2 \times 0.196421}} = 0.376\,\mathrm{radians}$$

The deformation ratio for the three stands are calculated using (3-23) as:-

$$\begin{aligned}\lambda_2 &= 1.382;\\ \lambda_3 &= 1.356;\\ \lambda_4 &= 1.333\end{aligned}$$

For calculating the lead of metal for the three stands, (3-24) is used and we as follows:-

$$\mathrm{S}_2 = \frac{0.587834 - 0.55622}{0.55622} = 0.056$$
$$\mathrm{S}_3 = \frac{0.724517 - 0.66337}{0.66337} = 0.092$$
$$\mathrm{S}_4 = \frac{0.889616 - 0.810447}{0.810447} = 0.097$$

The front and the rear tension for the middle stand can be calculated using (3-26) as:-

$$\sigma_0 = \frac{1}{0.045}\left[\left(\frac{32.2507}{23.636}\right) - \left(\frac{32.2507}{21.488}\right)\right]\left[\frac{0.196421}{0.224836}\cdot\frac{1}{1.356}\cdot\frac{1+0.092}{1+0.056}\right] = -2.01935\,\mathrm{MPa}$$
$$\sigma_1 = \frac{1}{0.045}\left[\left(\frac{37.271}{32.25707}\right) - \left(\frac{41.413}{32.2507}\right)\right]\left[\frac{0.207552}{0.196421}\cdot\frac{1}{1.333}\cdot\frac{1+0.097}{1+0.092}\right] = -2.2749\,\mathrm{MPa}$$

Equation (3-27) is used for finding out the resultant tension on the stand under consideration:-

$$\sigma_\Sigma = \sigma_0 - \sigma_1 = 0.255\,\mathrm{MPa}$$

The length of the deformation zone of the stand follows from (3-31) as:-

$$\mathrm{l_c} = \sqrt{(0.104089 - 0.0765497) \times 0.196421} = 0.0735\,\mathrm{m}$$

The projection of the area of contact between the work roll and the workpiece follows from (3-30) as:-

$$\mathrm{F_k} = \frac{0.0641636 + 0.075525}{2} \times 0.0735 = 0.0051703\mathrm{m}^2$$

The term η is calculated using (3-33) as:-

$$\frac{1}{\eta} = \frac{0.0765497}{0.104089} = 0.735$$

The change in the rolling moment of the stand under the influence of inter-stand tension follows from (3-29) as:-

$$\Delta\mathrm{M} = \frac{0.0051703 \times 0.0735}{0.735 - 1} \times 0.255 = -0.36567\,\mathrm{KNm}$$

The entire back and front tension in the workpiece is calculated by using (3-28) as:-

$$\mathrm{T}_0 = -2.01935 \times 0.579458 = -1.170128\,\mathrm{MN}$$
$$\mathrm{T}_1 = -2.2749 \times 0.463772 = -1.055034\,\mathrm{MN}$$

The deformation in the workpiece follows from (3-20) as:-

$$\delta = \frac{2 \times 0525}{0.376} = 1.34$$

With the use of (3-32), the change in roll pressure on the workpiece in the presence of inter-stand tension is given as:-

$$\Delta\mathrm{p} = -\left\{\left[\left(0.735 - 0.735^{0.126}\right)\cdot\frac{-2.01935}{-0.265}\right] - \left[\left(0.735^{0.126} - 1\right)\cdot\frac{-2.2749}{-0.265}\right]\right\} = 1.40195\,\mathrm{MPa}$$

With the use of (3-34), the torque on the stand can be calculated as follows:-

$$\mathrm{M_H} = 0.196421 \cdot \left(\frac{-1.170128}{1.356} + 1.055034\right)\cdot(1 + 0.092) = 41.2055\,\mathrm{KNm}$$

Appendix C

Drawings for Work Rolls

C-1 Technical Drawings

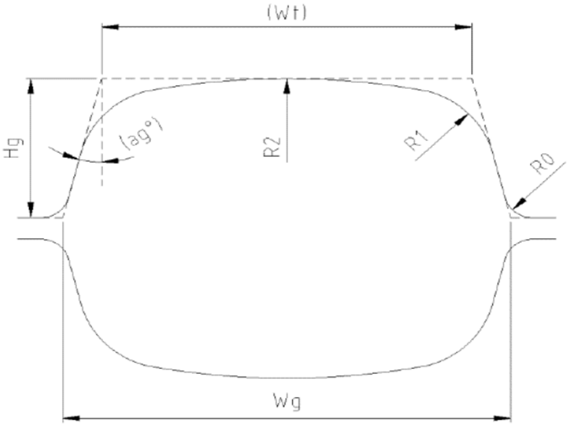

Figure C-1: Technical Drawing for Stand 1 [7]

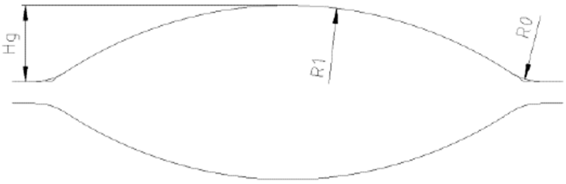

Figure C-2: Technical Drawing for Stand 2 and 4 [7]

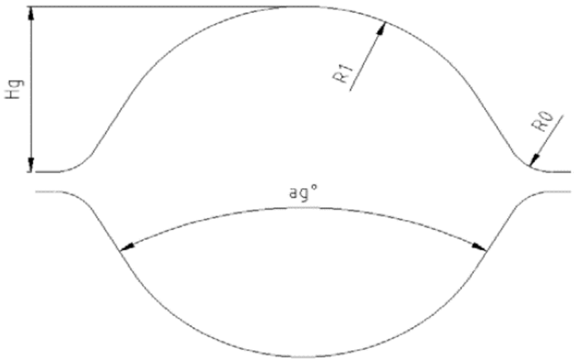

Figure C-3: Technical Drawing for Stand 3 [7]

C-2 2-D Sketches

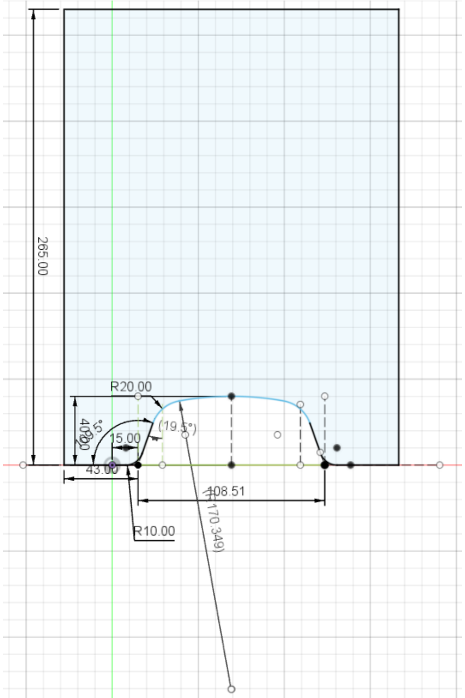

Figure C-4: 2-D Sketch for Stand 1 (By Author)

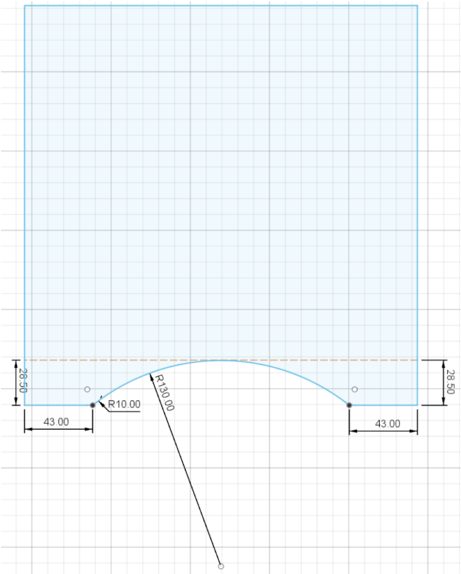

Figure C-5: 2-D Sketch for Stand 2 (By Author)

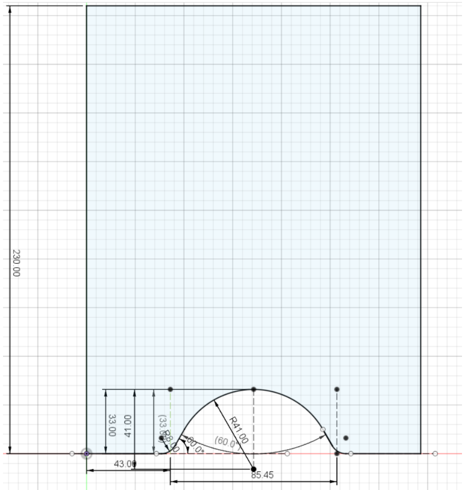

Figure C-6: 2-D Sketch for Stand 3 (By Author)

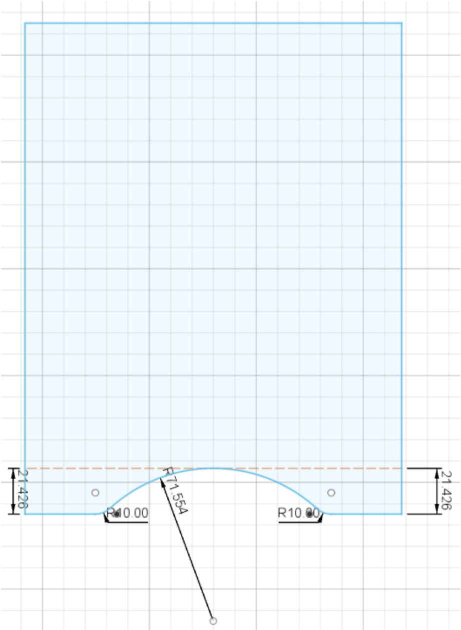

Figure C-7: 2-D Sketch for Stand 4 (By Author)

C-3 3-D Profiles

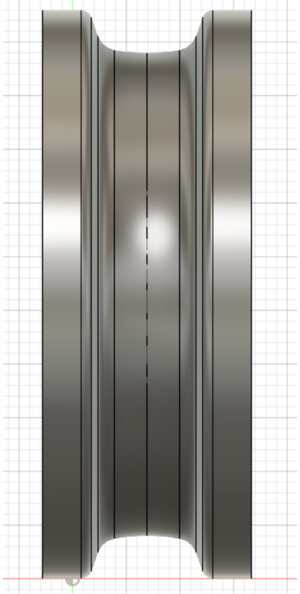

Figure C-8: 3-D Profile for Stand 1 (By Author)

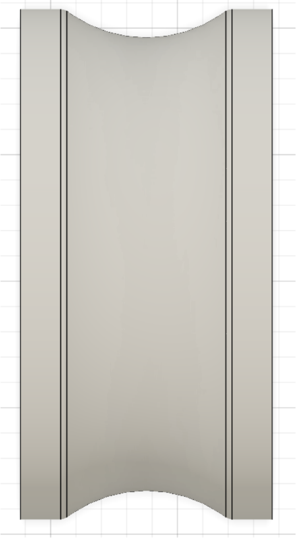

Figure C-9: 3-D Profile for Stand 2 (By Author)

Figure C-10: 3-D Profile for Stand 3 (By Author)

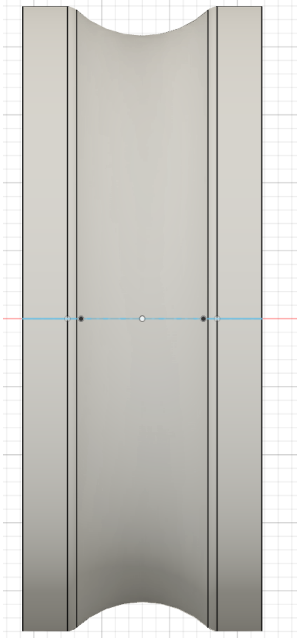

Figure C-11: 3-D Profile for Stand 4 (By Author)

Appendix D

MATLAB Codes

D-1 State Space Representations

```
clear all;
clc;
sampleT=0.001;
sys1=tf(32.2507,[0.01 1 0],'inputdelay',0.02);
sys2=tf(1,[0.014 1]);
main_sys= feedback(sys1,sys2);
ss_temp=ss(main_sys);
[A,B,C,D]= ssdata(ss_temp); % Continuous time
ss_temp_d=c2d(main_sys,sampleT);
[A1,B1,C1,D1]= ssdata(ss_temp_d); % Discrete time
figure(1)
step(ss_temp)
hold on
step(ss_temp_d)
hold off
```

D-2 Linear Quadratic Regulator (LQR) design

```
%% SYS CREATE

sys1=tf(32.2507,[0.01 1 0],'inputdelay',0.02);
sys2=tf(1,[0.014 1]);
main_sys= feedback(sys1,sys2);
ss_temp=ss(main_sys);
[A,B,C,D]= ssdata(ss_temp); % Continuous time
ss_temp_d=c2d(main_sys,0.001);
[A1,B1,C1,D1]= ssdata(ss_temp_d); % Discrete time
Co=ctrb(ss_temp_d);
Co_rank=rank(Co);

```

```
%% STATE OBSERVER

Ltest=place(A1',C1',[0.32,0.9,0.34])';
Ltest1=place(A1',C1',[0.4,0.9,0.5])';
Ltest2=place(A1',C1',[0.12,0.9,0.22])';
Ltest3=place(A1',C1',[0.01,0.9,0.12])';
Lfinal= Ltest;
%% DISTURBANCE OBSERVER
Kw1=20;
Kw2=50;
Kw3=70;
Kwfinal= Kw3;

%% STATE FEEDBACK GAIN
Q1 = eye(3);
Q2= 10 * eye(3);
R1 = 1;
R2 = 10;
R3= 100;
R4= 1000;
N=0;
[K1,S1,e1] = dlqr(A1,B1,Q1,R1,N);
[K2,S2,e2] = dlqr(A1,B1,Q1,R2,N);
[K3,S3,e3] = dlqr(A1,B1,Q1,R3,N);
[K4,S4,e4] = dlqr(A1,B1,Q1,R4,N);
[K5,S5,e5] = dlqr(A1,B1,Q2,R1,N);
[K6,S6,e6] = dlqr(A1,B1,Q2,R2,N);
[K7,S7,e7] = dlqr(A1,B1,Q2,R3,N);
[K8,S8,e8] = dlqr(A1,B1,Q2,R4,N);
Klqrfinal=K3;
```

D-3 Model Predictive Control (MPC) design

```
%% SYSTEM DEFINE
clc;
clear all;
sys1=tf(32.2507,[0.01 1 0],'inputdelay',0.02);
sys2=tf(1,[0.014 1]);
main_sys= feedback(sys1,sys2);
ss_temp=ss(main_sys);
[A,B,C,D]= ssdata(ss_temp); % Continuous time
ss_temp_d=c2d(main_sys,0.001);
[A1,B1,C1,D1]= ssdata(ss_temp_d);% Discrete time
L=place(A1',C1',[0.29,0.27,0.28])';


%% SYSTEM LOAD
%%%%%%%%Please make sure .mat files are in the same folder as the matlab
    code
PlantMPCmain = load('C:\Users\Anant Sareen\Desktop\Thesis Implement\
    PlantforMPC.mat');
```

```
Referencesignal = load('C:\Users\Anant Sareen\Desktop\Thesis Implement\referencesignalMPCdesign.mat');
MDsignal = load('C:\Users\Anant Sareen\Desktop\Thesis Implement\MDSignalMPCdesign.mat');
mpc3_ModelOD=load('C:\Users\Anant Sareen\Desktop\Thesis Implement\mpc3_ModelOD.mat');

%% MPC CONTROLLER 1
% create MPC controller object with sample time
mpc1 = mpc(PlantMPCmain.PlantMPC, 0.001);
% specify prediction horizon
mpc1.PredictionHorizon = 10;
% specify control horizon
mpc1.ControlHorizon = 2;
% specify nominal values for inputs and outputs
mpc1.Model.Nominal.U = [0;0];
mpc1.Model.Nominal.Y = 0;
% specify overall adjustment factor applied to weights
beta = 1.0833;
% specify weights
mpc1.Weights.MV = 0*beta;
mpc1.Weights.MVRate = 0.104081016663371/beta;
mpc1.Weights.OV = 0.96079*beta;
mpc1.Weights.ECR = 100000;
% specify overall adjustment factor applied to estimation model gains
alpha = 10;
% adjust default output disturbance model gains
setoutdist(mpc1, 'model', getoutdist(mpc1)*alpha);
% adjust default measurement noise model gains
mpc1.Model.Noise = mpc1.Model.Noise/alpha;
% specify simulation options
options = mpcsimopt();
options.RefLookAhead = 'off';
options.MDLookAhead = 'off';
options.Constraints = 'on';
options.OpenLoop = 'off';
% run simulation
figure(1)
sim(mpc1, 10001, Referencesignal.mpc3_RefSignal, MDsignal.mpc3_MDSignal, options);



%% MPC2 CONTROLLER 2
% create MPC controller object with sample time
mpc2 = mpc(PlantMPCmain.PlantMPC, 0.001);
% specify prediction horizon
mpc2.PredictionHorizon = 20;
% specify control horizon
mpc2.ControlHorizon = 2;
% specify nominal values for inputs and outputs
mpc2.Model.Nominal.U = [0;0];
mpc2.Model.Nominal.Y = 0;
```

```
% specify overall adjustment factor applied to weights
beta = 1.0833;
% specify weights
mpc2.Weights.MV = 0*beta;
mpc2.Weights.MVRate = 0.104081016663371/beta;
mpc2.Weights.OV = 0.96079*beta;
mpc2.Weights.ECR = 100000;
% specify overall adjustment factor applied to estimation model gains
alpha = 10;
% adjust default output disturbance model gains
setoutdist(mpc2, 'model', getoutdist(mpc2)*alpha);
% adjust default measurement noise model gains
mpc2.Model.Noise = mpc2.Model.Noise/alpha;
% specify simulation options
options = mpcsimopt();
options.RefLookAhead = 'off';
options.MDLookAhead = 'off';
options.Constraints = 'on';
options.OpenLoop = 'off';
% run simulation
figure(2)
sim(mpc2, 10001, Referencesignal.mpc3_RefSignal, MDsignal.mpc3_MDSignal,
    options);



%% MPC CONROLLER 3
% create MPC controller object with sample time
mpc3 = mpc(PlantMPCmain.PlantMPC, 0.001);
% specify prediction horizon
mpc3.PredictionHorizon = 30;
% specify control horizon
mpc3.ControlHorizon = 2;
% specify nominal values for inputs and outputs
mpc3.Model.Nominal.U = [0;0];
mpc3.Model.Nominal.Y = 0;
% specify overall adjustment factor applied to weights
beta = 1.0833;
% specify weights
mpc3.Weights.MV = 0*beta;
mpc3.Weights.MVRate = 0.104081016663371/beta;
mpc3.Weights.OV = 0.96079*beta;
mpc3.Weights.ECR = 100000;
% specify overall adjustment factor applied to estimation model gains
alpha = 10;
% adjust default output disturbance model gains
setoutdist(mpc3, 'model', getoutdist(mpc3)*alpha);
% adjust default measurement noise model gains
mpc3.Model.Noise = mpc3.Model.Noise/alpha;
% specify simulation options
options = mpcsimopt();
options.RefLookAhead = 'off';
options.MDLookAhead = 'off';
```

```
options.Constraints = 'on';
options.OpenLoop = 'off';
% run simulation
figure(3)
sim(mpc3, 10001,Referencesignal.mpc3_RefSignal, MDsignal.mpc3_MDSignal,
    options);


%% MPC CONTROLLER 4

% create MPC controller object with sample time
mpc4 = mpc(PlantMPCmain.PlantMPC, 0.001);
% specify prediction horizon
mpc4.PredictionHorizon = 30;
% specify control horizon
mpc4.ControlHorizon = 3;
% specify nominal values for inputs and outputs
mpc4.Model.Nominal.U = [0;0];
mpc4.Model.Nominal.Y = 0;
% specify overall adjustment factor applied to weights
beta = 1.0833;
% specify weights
mpc4.Weights.MV = 0*beta;
mpc4.Weights.MVRate = 0.104081016663371/beta;
mpc4.Weights.OV = 0.96079*beta;
mpc4.Weights.ECR = 100000;
% specify overall adjustment factor applied to estimation model gains
alpha  = 10;
% adjust custom output disturbance model gains
setoutdist(mpc4, 'model', mpc3_ModelOD.mpc3_ModelOD*alpha);
% adjust default measurement noise model gains
mpc4.Model.Noise = mpc4.Model.Noise/alpha;
% specify simulation options
options = mpcsimopt();
options.RefLookAhead = 'off';
options.MDLookAhead = 'off';
options.Constraints = 'on';
options.OpenLoop = 'off';
% run simulation
figure(4)
sim(mpc4, 10001, Referencesignal.mpc3_RefSignal, MDsignal.mpc3_MDSignal,
    options);
```

Bibliography

[1] ArcelorMittal Hamburg Internal Presentation , Internal Document.

[2] R. Sah and S. Dutta, "Direct reduced iron: Production," *Encyclopedia of Iron, Steel, and Their Alloys*, p. 27, 2016.

[3] A. Karabegovic, *Model development and minimum tension control for looperless rolling mills.* Technische Universität Hamburg-Harburg, Master Thesis, 2011.

[4] C. W. D. Silva, *Modelling and Control of Engineering Systems.* CRC Press, 2009.

[5] N. Mohan, *Electrical Machines and Drives: A First Course.* WILEY India, 2013.

[6] J. Pitter and M. Simaan, *Tandem Cold Metal Rolling Mill Control Using Practical Advance Methods.* Springer-Verlag London, 1 ed., 2011.

[7] ArcelorMittal Hamburg Drawing Archives, Internal Document.

[8] T. Keviczky and A. Dabiri, *Lecture Notes, Control Engineering.* Delft University of Technology.

[9] K. Ogata, *Modern Control Engineering.* Pearson, 5 ed.

[10] S. Grammatico, *Lecture Notes, Model Predictive Control.* Delft University of Technology.

[11] Qform Group Help Manual QForm 10.1.

[12] J.A.Schey, "Progress report on recent advances in bulk metal deformation processes," *International Metal Reviews*, vol. 22, pp. 302–303, 1977.

[13] S. Choi, A. Rossiter, and P. Fleming, "A survey of the looper-tension control technology in hot rolling mills," *IFAC Proceedings Volumes*, vol. 38, pp. 37–44, 2005.

[14] H. Katori, R. Hirayama, T. Ueyama, and K. Furuta, "On the possibility of looperless rolling on hot rolling process," *IFAC Automation in Mining, Mineral and Metal Processing, Tokyo, Japan*, pp. 119–124, 2001.

[15] "Intranet arcelormittal hamburg." https://hamburg.arcelormittal.com/Ueber-uns/.

[16] W. Leonhard, *Control of Electric Drives.* Springer-Verlag Berlin Heidelberg, 3 ed., 2001.

[17] K. Schröder, *A Basic Understadning of Mechanics of Rolling Mills.* ESW, 2003.

[18] W. Roberts, *Hot Rolling of Steel.* 270 Madison Avenue,New York: Marcel Dekker Inc, 1983.

[19] A. Chandra and S. Mukherjee, "A finite element analysis of metal forming processes with thermomechanical coupling," *International Journal of Mechanical Sciences*, vol. 26, pp. 661–676, 1984.

[20] A. Chandra, "A generalized finite element analysis of sheet metal forming with an elastic-viscoplastic material model," 1986.

[21] S. Oh, J. Park, S. Kobayashi, and T. Altan, "Application of fem modeling to simulate metal flow in forging a titanium alloy engine disk," 1983.

[22] L. Dewasurendra, "A finite element method for ring rolling processes," *PHD Thesis, College of Engineering and Technology, Ohio University*, 1998.

[23] A. Chandra, "Simulation of rolling processes by the boundary element method," *Computational Mechanics*, vol. 4, pp. 443–451, 1989.

[24] A. Chandra and S. Mukherjee, "Boundary element formulations for large strain-large deformation problems of viscoplasticity," *International Journal of Solids and Structures*, vol. 20, pp. 41–53, 1984.

[25] A. Chandra and S. Mukherjee, "A boundary element analysis of metal extrusion processes," 1987.

[26] J. Alexander, "On the theory of rolling," *Proceedings of The Royal Society*, 1971.

[27] G. Nikitin, *The theory of continuous longitudinal rolling (In Russian).* MSTU im. N.E. Bauman Moscow, 2009.

[28] A. O'Dwyer, *Handbook of PI and PID controller tuning rules.* Imperial College Press, 3 ed.

[29] K. J. Astrom and B. Wittenmark, *Computer Controlled Systems, Theory and Design.* Tsinghua University Press, 3 ed.

[30] Matlab Documentation, *Choose Sample Time and Horizons.* Mathworks.

Glossary

List of Acronyms

DCSC	Delft Center for Systems and Control
FEM	Finite-Element Method
FE	Finite- Element
DC	Direct Current
AC	Alternating Current
EMF	Electromotive Force
MOI	Moment of Inertia
FEA	Finite Element Analysis
BEM	Boundary Element Method
CAD	Computer-Aided Design
CAM	Computer-Aided Manufacturing
PCB	Printed Circuit Board
LQR	Linear Quadratic Regulator
MPC	Model Predictive Control

List of Symbols

Constants	
π	3.14
E	Young's Modulus for Steel, 103.5 $\frac{\mathrm{KN}}{\mathrm{mm}^2}$
g	Gravitational constant
DC Motor	
b	Flux ratio
B_m	Motor damping ratio

E_g	Static Electromotive Force (EMF)
I_a	Static armature current
I_f	Static field current
J_m	Motor Moment of Inertia (MOI)
K_t	Motor torque constant
K_v	Motor voltage constant
L_a	Armature circuit inductance
L_f	Field circuit inductance
R_a	Armature circuit resistance
R_f	Field circuit resistance
T_d	Resultant motor torque
T_m	Motor torque
T_L	Load torque
T_R	Rated torque
V_a	Static armature voltage
V_f	Static field voltage
ω_m	Motor speed
ω_ref	Speed reference
$\omega_{m\mathrm{R}}$	Rated motor speed
ϕ_m	Motor flux
ϕ_R	Rated motor flux
e_g	Dynamic EMF
i_a	Dynamic armature current
i_f	Dynamic field current
$i_{a\mathrm{R}}$	Rated dynamic armature current
u_{Y_n}	Voltage set by current controller normed
$U_{\max}$	Maximum output voltage of rectifier circuit
v_a	Dynamic armature voltage
v_f	Dynamic field voltage
$v_{a\mathrm{R}}$	Rated dynamic armature voltage

Other symbols

$\dot{m}$	Mass flow rate
° C	Degree Celsius
MVA	Mega Volt Amperes
MW	Mega Watt

Workpiece

α	Roll bite angle
$\dot{\epsilon}$	Strain Rate
ϵ	Strain
η	Viscosity of material

λ_{b}	Backward Slip Coefficient
λ_{f}	Forward Slip Coefficient
$\mathrm{h}_{(j,j+1)}$	Height of exiting workpiece
$\mathrm{h}_{(j-1,j)}$	Height of incoming workpiece
$\mathrm{K}_{\mathrm{W}m}$	Average forming resistance
$\mathrm{L}_{(j,j+1)}$	Inter-stand distance
R	Radius of the work roll
R'	Working radius of the work roll
v_j	Speed of workpiece at neutral point
$\mathrm{v}_j^{(1)}$	Speed of incoming workpiece
$\mathrm{v}_j^{(2)}$	Speed of exiting workpiece
σ_{d}	Dynamic Stress
σ_{s}	Static Stress
$\sigma_{j,j+1}$	Interstand tension in exiting workpiece
$\sigma_{j-1,j}$	Interstand tension in incoming workpiece
τ_η	Retardation Time

Work Rolls

D	Roll diameter
g	Gear ratio
j	Stand Number
v	Roll tangential velocity

Theoretical Analysis Equations

α	Bite Angle
Δp	Change in roll pressure
δ	Deformation in Material
$\Delta\mathrm{M}$	Change in rolling moment
λ	Deformation Ratio
A_{0j}	Area of workpiece before stand entry
A_{1j}	Area of workpiece after stand exit
B_0	Width of workpiece before stand entry
B_1	Width of workpiece after stand exit
C	Calibration constant for continuous rolling
$\mathrm{D}_{\mathrm{k}j}$	Work roll diameter of stand j
f	Coefficient of external friction
F_j	Exit cross-section area of material from stand j
F_{k}	Projection area of contact surface between workpiece and work rolls
H_0	Height of workpiece before stand entry
H_1	Height of workpiece after stand exit
k_1	Constant for steel, 1
l_{c}	Length of deformation zone

$\mathrm{M_H}$	Torque on a particular stand
n_j	Work roll speed of stand j
$\mathrm{n_{coordinated}}$	Speed of work roll in coordinated mode
n_ϕ	Current speed of work roll
S_j	Lead of metal stand j
T	Entire strip tension
T	Temperature of workpiece
v	Exit speed of workpiece from stand
V_j	Exit speed of material from stand j
$\mathrm{v_r}$	Work roll speed of stand
μ_j	Friction Coefficient stand j
σ_0	Rear tension
σ_1	Front tension